TÉCNICO LISBOA

PANS and DES of a Simplified Heavy-Duty Vehicle:

Comparison and an Active Flow Control Application

Miguel Calixto de Sousa

Thesis to obtain the Master of Science Degree in

Mechanical Engineering

Supervisors: Prof. João Carlos de Campos Henriques
Dr. Guglielmo Minelli

Examination Committee

Chairperson: Prof. Carlos Frederico Neves Bettencourt da Silva
Supervisor: Prof. João Carlos de Campos Henriques
Member of the Committee: Prof. José Manuel da Silva Chaves Ribeiro Pereira

November 2018

Abstract

This work presents two main purposes: one is to see how the partially-averaged Navier-stokes (PANS) method performs against the detached eddy simulation (DES) method for different grid refinement levels, when applied to the study of the external aerodynamics of a generic heavy-duty vehicle, and the other is to study the application of Active Flow Control (AFC) on the trailer front pillars of a generic heavy-duty vehicle, on a dynamic oscillating configuration, using PANS.

For the first part, a cross analysis of the flow physics around the generic heavy-duty vehicle and a comparison of the time-averaged and the instantaneous flow structures, force coefficients and aerodynamic forces of the results obtained using DES and PANS with three grids of different level of refinement, is performed. The results show that both PANS and DES simulations capture the same main flow features and produce similar trends, which are in accordance with published works. The DES shows more robustness, as its results using the three different meshes are more similar than in PANS, and it handles the coarser mesh better, since the PANS results with the coarse mesh show a significant deviation from the ones using the more refined meshes.

For the second part, the heavy-duty model is simulated to have a dynamic oscillation of the yaw angle between $-10^\circ < \beta < 10^\circ$ with a non-dimensional frequency of $\mathrm{St} = fW/U_{inf} = 0.1$, with and without the actuation of AFC in the trailer front pillars. Overall, the actuation is not effective and even shows to be disadvantageous.

Keywords

Partially-averaged Navier-stokes, Detached eddy simulation, Active Flow Control, Generic Heavy-Duty vehicle, CFD

Resumo

Este trabalho tem dois focos: Um é ver como o desempenho do método partially-averaged Navier-stokes (PANS) se compara com o do método detached eddy simulation (DES) quando aplicado ao estudo aerodinâmico de um veículo genérico heavy-duty, usando diferentes malhas com diferentes níveis de refinamento. O outro é o uso do método PANS para estudar a aplicação de Active Flow Control (AFC) nos pilares frontais do reboque do veículo genérico, em condições de oscilação dinâmica.

Na primeira parte é feita uma análise do escoamento em torno de um veículo heavy-duty genérico, e uma comparação das estruturas presentes no escoamento instantâneo e médio, e dos coeficientes de forças aerodinâmicas, entre os diferentes resultados obtidos com PANS e DES em malhas de diferente nível de refinamento. É concluído que ambos os modelos capturam as mesmas características principais do escoamento que as de trabalhos previamente publicados. O modelo DES demonstrou ser mais robusto que o PANS, uma vez que os resultados dos três níveis de refinamento são mais semelhantes entre si, e porque os resultados da aplicação de PANS com a malha mais grosseira apresentam um desvio considerável em comparação com os resultados de PANS com malhas mais refinadas.

Na segunda parte o veículo heavy-duty é simulado em condições dinâmicas, com uma oscilação em yaw entre $-10 < \beta < 10$, com uma frequência reduzida de $\mathrm{St} = fW/U_{inf} = 0.1$, com e sem atuação de AFC nos pilares frontais do reboque. Os resultados obtidos demonstram que a atuação AFC escolhida piora o performance aerodinâmico do veículo.

Palavras Chave

Partially-averaged Navier-stokes, Detached eddy simulation, Active Flow Control, Veículo Heavy-Duty genérico, CFD

Contents

List of Figures

List of Tables

1

Introduction

1.1 Motivation and background of the study

Transportation is fundamental in today's world and it is a key element in the frame of sustainable development due to its economical, social and environmental impact. The fast paced consumption of energy resources, the increasing oil prices and the aggravation of global warming by greenhouse gas (GHG) emission make the reduction of fuel consumption a priority at global level. Under the Paris Agreement, the European Union has committed to avoiding climate change by limiting global warming to well below 2º C, which makes decreasing GHG emissions a key prerequisite. Under this light, the EU set the strategy for low emission mobility of lowering the transport GHG emissions by at least 60% when compared to 1990. The National emissions reported to the UNFCCC and to the EU Greenhouse Gas Monitoring Mechanism provided by European Environment Agency (EEA) currently (September, 2018) shows that in Europe road transportation is responsible for 72% of the total GHG emissions, from which around one quarter is caused by Heavy-duty vehicles (trucks, buses and coaches). Heavy-duty vehicles are this way responsible for almost 5% of the total EU-28 GHG emissions, which makes the development of more efficient heavy duty vehicles imperative.

The aerodynamic drag accounts for more than 60% of the total power consumption of a traveling truck at cruise speed, [1], so the improvement of its aerodynamic efficiency have a major impact on the total power consumption, making it necessary to fulfill such commitments. For such efficiency improvement, the understanding of the heavy-duty vehicles complex external flows, which is defined by turbulent boundary layers, massive separation, shear layer evolution and reattachment, is of great importance in its design. Aerodynamic design solutions and add-ons for heavy-duty vehicles, such as rounded corners, cab extenders, skirts and underbody wedges for the wheels, are already broadly used, due to their already proved success in significantly increasing aerodynamics efficiency. All these improvements are passive of nature, having the limitation of only being optimized for one specific setting of conditions. In this work, an alternative method is considered, the application of active flow control (AFC) devices which is of increasing interest due to the possibility of its adaptation to different conditions through close-loop control. This way, the application of AFC can increase the vehicle's aerodynamic efficiency, while enhancing its stability, in all real road conditions.

There are several AFC techniques, and the one used in this work is the zero net mass flux (ZNMF) synthetic jet, which is a control technique that has been extensively used in different aerodynamic fields to mitigate flow separation. Inclusive, it was implemented to manipulate the wake of generic vehicles, [2], control the flow separation at the A-pillar of oscillating simplified truck cabins, [3], and truck-trailer models, [4]. As the goal of applying AFC on a heavy-duty vehicle is to prevent a large scale flow separation, it is important to first know the main sources of drag due to this phenomena. These are the front of the tractor, the gap between the tractor and the trailer, wheel-housing and wheels, the underbody and majorly the trailer wake region, [4, 5]. The application of AFC to decrease the drag in some of these regions have already been studied through experiments and numerical simulation. For example, in [6], the application of AFC on the A-pillars of a simplified truck in constant zero yaw angle is proven to mitigate, and in some cases even to suppress, the recirculation bubble created in the truck cabin A-pillars, which ultimately leads to a C_d reduction of up to 30%, when an actuation frequency equal to the characteristic frequency of the shear layer instability is used. In closer to real conditions, where side winds and periodic gusts are considered, a decrease of drag, stabilization of the flow and reduction of the size of the side recirculation bubble is also obtained, [3]. In [4], the application of AFC actuating on the trailer wake of a truck-trailer model led to a decrease of up to 1.8% in constant zero yaw angle conditions. Although there are already passive solutions to reduce the recirculation in the gap, such as cab extenders, the study of AFC applied in gap is not so common. The use of AFC on the front pillars of the trailer is not only very advantageous for heavy-duty vehicles without the possibility to have cab extenders, but it could also be for the ones that do. Specially, under realistic conditions, where the vehicle is subjected to side wind, gusts and atmospheric turbulence, causing the incoming flow to not be oriented along the direction of the vehicle, making the cab extenders work poorly, [7]. Also, with the

use of AFC, the radius of the trailer front pillars can be decreased, increasing this way the space inside the trailer while having a good aerodynamic performance. Based on the major success of the AFC application in the truck cabin presented in previous works, one of the current work aims is to present a solution to the drag in the gap region by application of AFC, in close to real conditions, where the presence of front and side wind gusts lead to a large separation of the flow in the trailer front pillars, extending along the side surfaces of it. This was done in this work through the study of an oscillating simplified truck model with and without the application of AFC in the front trailer pillars. The studies are made using geometry and meshes similar to the ones in the already validated cases in [3] and [6], and also trough the application of PANS in AVL-Fire, since their results in this conditions are already validated through experiments. The use of an oscillating model to recreate real conditions was first introduced in [8] for a tractor-trailer model, and recently have been studied numerically and experimentally in [3] on a truck cabin with AFC application. All these studies highlight how different the flow nature is from quasi-static to dynamic configurations, and conclude that it is of major importance to implement more realistic tests in the design of vehicles aerodynamics.

In order to study the complex turbulent flow around the truck model CFD is used, where different approaches to solve the flow field are available. The choice between methods is a compromise between flow resolution and computational resources available. The Reynolds Averaged Navier-Stokes (RANS) is one of the most used turbulence models in the industry nowadays, as it gives an accurate prediction of attached flows and of some cases with minor separations, which are cases present in some common engineering applications. However, numerical methods based on standard RANS fail to describe massively separated flows, as it cannot predict wake and vortex flow, due to the inherent unsteady character of the flow and the inadequate modeling of the turbulence. Direct numerical simulation (DNS) resolves the whole spectrum of spatial and temporal scales of turbulence without needing any modeling of the turbulence. However, this requires very fine spatial and temporal resolution, which makes it prohibitive for industrial turbulent flows.

The large-eddy simulation (LES) method is one of the most popular solutions to tackle the before mentioned methods' main drawbacks. It decreases the computational cost, comparing with DNS, by modelling the small length scales, which are the most computationally expensive to resolve, only resolving the larger scales. The LES method has been proven to predict turbulent flows with high accuracy, as it can be seen in the study of trucks, [10], trains, [11], and buses, [12]. However, the LES method is still too resource expensive, leaving the former problem open. The inaccuracy of the steady RANS and the expensiveness of the DNS and LES techniques have led to pursue the hybridization and bridging the RANS modeling approaches and the flow resolving approaches, LES and DNS. The detached-eddy simulation (DES), was first proposed in 1997 by Spalart et al., [13], and it is the most popular hybrid method in the research community and industry, as it has been successful in predicting the flow around

bluff bodies, like trains [14, 15], Ahmed bodies [16]. The base of DES is that it behaves as unsteady RANS (URANS) models in the near-wall regions and as LES in the regions away from the near-wall. The partially-averaged Navier–Stokes (PANS) is a bridging method proposed by Girimaji et al. in 2003, [17], and it is a method that is quickly getting recognition in the research community and industry. It is based in the bridging between RANS and DNS depending on the dynamic control parameters f_k and f_ϵ, which are dependent on the flow local characteristics and local grid dimensions. This way, the PANS model will behave as RANS on regions of low turbulence and coarser grid and as DNS in regions of high turbulence and refined enough mesh. The PANS method has been successful in solving the flow around different bluff body, like landing gears, [18], Ahmed bodies, [19], and a generic truck cabin with AFC application, [6], and in some of this cases it is shown that PANS predictions are better than LES, when using coarser meshes, i.e. with unresolved LES, since the near wall flow structures cannot be resolved with such coarse grid.

In the first part of the present work, PANS and DES simulations of the flow around a truck model, at a constant zero yaw angle model, at Reynolds number $\mathrm{Re} = 250000$, have been performed. For each method, three equivalent simulations are ran using a common coarse (3 million cells) , medium (5 milion cells) and fine mesh (8 million cells). The use of this resolutions in PANS cases of similar geometries, domain, conditions and with the same characteristic length, W, have previously been validated in the study of bluff body flows, [20], application of AFC on a generic truck cabin, [6], and the application of AFC on a oscillating truck cabin, [3]. The objective of this simulations is not only to understand the model flow nature, but also to compare the capability of PANS and DES in predicting the unsteady turbulent flow around the model, how they behave with refinement of the mesh and how they compare with PIV experimental results in the wake of the trailer.

1.2 Structure of the dissertation and objectives

The present dissertation is divided into two parts:

In the first, numerical studies are carried out to understand the physics of the flow around a simplified truck model, as well as to conduct a detailed comparison of the PANS and DES prediction results of the unsteady turbulent flow, and the behaviour of each method to different levels of grid refinement. Here, a simulation of the truck model under the flow at a constant zero yaw angle was performed, using a coarse (3 million cells), medium (5 million) and fine (8 million) meshes for each method, PANS and DES. The results are also compared with unpublished PIV experimental results in the wake of the trailer. The model and the grids used have a similar geometry and resolution, of the ones used in [6], of a PANS study of the flow over a generic truck cabin, which were already validated through experiments.

In the second, the focus is on starting to access how viable is the application of the active flow

control (AFC) technique zero net mass flux (ZNMF) pulsating synthetic jet in the trailer front pillars, in order to mitigate the flow separation and consequently enhancing its aerodynamic performance on the gap region during close to real conditions. Here, two simulations of an oscillating simplified truck model are carried out, one with the application of AFC in the front trailer pillars and one without. In this simulations the PANS method is used, and the model studied is the same as in the first part of this thesis, but with a wider trailer.

2

Theory

In this chapter, an overview of some numerical models used in Computational Fluid Dynamics, including the methods of focus in this thesis, DES and PANS, is presented. This is followed by a revision on truck aerodynamics and the application of active flow control.

2.1 Turbulence and its modelling

Most kind of flows encountered in daily life and engineering are turbulent: the flowing water in rivers, atmosphere and ocean currents, the flow around vehicles, the flow in a gas turbine, the mixing of air and fuel in engines, and pipe flows are some examples. It is evident that the presence of turbulence in most natural and man-made systems, and its influence in them is almost always impossible to avoid. Therefore we must be able to understand it and predict it. Although the concept of turbulence is almost intuitive, its precise definition is very difficult to formulate, leaving the description of its characteristic features as the best option, [21]:

- A turbulent flow is irregular, this is it is random and unpredictable

- A turbulent flow is diffusive, which causes rapid mixing and increased rates of momentum, heat and mass transfer.
- Turbulent flows occur at high Reynolds numbers.
- A turbulent flow is rotational and three-dimensional
- A turbulent flow is dissipative, the energy in the small eddies (kinetic energy) is transformed into internal energy (heat), through the cascade process.
- Turbulence is a continuum phenomenon, the smallest scales occurring in a turbulent flow are much larger than the molecular length scale.

Although turbulent flows have been identified and distinguished from laminar flows centuries ago, it was only in 1883 that Osborne Reynolds discovered the dimensionless number that predicts the transitions between the two flow states, based on the flow property velocity, U, the fluid property, kinematic viscosity, ν, and the geometry length scale, L , later called the Reynolds number, Re [22].

$$\mathrm{Re} = \frac{UL}{\nu}. \tag{2.1}$$

The Reynolds number represents therefore the ratio between inertial and viscous forces. If the inertial forces are dominant, the flow is turbulent, otherwise, if the viscous forces, defined as the resistance to flow, are dominant, the flow is laminar. As turbulence defines most of the engineering flows (such as the flow around a vehicle), setting the Reynolds number is crucial in order to correctly define the flow field. In vehicle aerodynamics, the characteristic dimension of the vehicle is defined as the length scale, L, and the free stream velocity as U in the Reynolds equation.

It is generally accepted that the fluid motion is governed by the Navier-Stokes equations (NSE), a description of the conservation of mass and momentum for a fluid particle subjected to the continuum approximation. For an incompressible, single-phase flow with constant density, ρ, and dynamic viscosity, μ, the NSE reads:

$$\frac{\partial u_i}{\partial x_i} = 0 \tag{2.2}$$

$$\frac{\partial u_i}{\partial t} + u_j \frac{\partial u_i}{\partial x_j} = -\frac{1}{\rho}\frac{\partial p}{\partial x_i} + \nu \frac{\partial^2 u_i}{\partial x_j \partial x_j} + f_i. \tag{2.3}$$

Equation 2.2 is the continuity equation, which expresses the conservation of mass, and equation 2.3 is the momentum equation, which expresses the conservation of momentum. $u_{i=x,y,z}$ are the three components of the velocity vector in a Cartesian coordinate system, p is the static pressure and f_i is other possible body forces. The NSE mathematically describe the whole spectrum of flow scales present in a turbulent flow, in time and space. In turbulent flows, the scales present range from vortices of size of the

vehicle's characteristic length, L, to the smallest scales in the flow, called the kolmogorov scales, which are smaller than the millimeter for vehicle flows. The energy cascade process is represented in figure 2.1, along with the scales' energy level, $E(k)$. This cascade process is divided in three regions, depending on the wave number, k, describing the flow scale. The first region (I), the energy containing region, is constituted by the largest scale eddies, which carry most of the energy in the cascade, extracted from its interaction with the mean flow. The energy is consequentially transferred from the larger to the slightly smaller eddy (tipically in an anisotropic way) through the inertial subrange (region II). The dissipation of the kinetic energy into internal energy (heat) occurs at the smallest scales (usually isotropic), in the so called kolmogorov scales, at the dissipation range (region III).

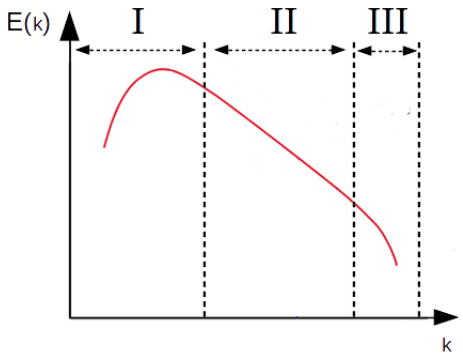

Figure 2.1: Energy cascade of a turbulent flow. I - Energy containing region, II - inertial subrange, III - dissipative region.

When numerically solving 2.2 and 2.3, without any modelling or hypothesis, with all scales of motion being resolved, the direct numerical simulation (DNS) approach is used [23]. This means that the whole range of spatial and temporal scales of the turbulence are being resolved, in the computational mesh, from the smallest Kolmogorov micro-scales up to the largest scales. DNS is the method that gives the most accurate representation of the real flow, however the computational effort in DNS rises with Reynolds number in the power of $9/4$, [24], due to the very small character of the dissipative scales, which makes such calculations prohibitive for most engineering applications of practical interest, at the present and in the foreseeable future. Therefore, DNS is only used to study fundamental flows, such as isotropic turbulence [25, 26], turbulent boundary layers [27] and turbulent pipe flows [28]. To achieve affordable computational costs for turbulence resolving simulations, the resolved turbulence scales must be larger than those resolved using DNS, therefore turbulent models must be introduced in order to get an approximation of the DNS solution of the flow. One of the most used turbulence models in the industry nowadays are based on the Reynolds Averaged Navier-Stokes (RANS), where all the turbulence is modeled. Here the Reynolds decomposition is introduced by dividing the flow into a superposition of

a mean and fluctuating part:

$$u_i = \overline{u}_i + u_i', \tag{2.4}$$

which applied to the NSE, 2.2 and 2.3, gives the RANS equations:

$$\frac{\partial \overline{u}_i}{\partial x_i} = 0 \tag{2.5}$$

$$\frac{\partial \overline{u}_i}{\partial t} + \overline{u}_j \frac{\partial \overline{u}_i}{\partial x_j} = -\frac{1}{\rho}\frac{\partial \overline{p}}{\partial x_i} + \frac{\partial}{\partial x_j}\left(\frac{\nu \partial \overline{u}_i}{\partial x_j} + \frac{1}{\rho}\tau_{ij}\right), \tag{2.6}$$

where the additional term τ_{ij} is the Reynolds stress tensor,

$$\tau_{ij} = -\rho(\overline{u_i' u_j'}), \tag{2.7}$$

which is present due to the non-linearity of the NSE. This term introduces six new unknowns, which make the system impossible to solve and leading to the well known closure problem. To close this problem the Reynolds stresses have to be modeled. Joseph Valentin Boussinesq was the first to tackle this problem, with the so called Boussinesq's assumption, where the concept of eddy viscosity is introduced to model the turbulent diffusion:

$$-\overline{u_i' u_j'} = \nu_t\left(\frac{\partial \overline{u}_i}{\partial x_j} + \frac{\partial \overline{u}_j}{\partial x_i}\right) - \frac{2}{3}\left(\frac{\partial \overline{u}_k}{\partial x_k} + k\right)\delta_{ij}, \tag{2.8}$$

where k is the turbulent kinetic energy. As this assumption closes the system by relating the turbulence stresses to the mean flow, only the mean value of the flow is resolved, the large scales (region I in fig. 2.1), modelling the whole spectra present in the energy cascade and the dissipation. This way, the grid and time step used can be more relaxed than when using DNS, meaning a much lower computational cost, however with the cost of losing accuracy. This approach is one of the most famous in the industry and it is basis for the steady state engineering turbulence models such as two-equation models, like $k-\epsilon$ and $k-\omega$, and various Reynolds Stress Models. However, this approach presupposes a large separation of the turbulent fluctuating scales and the energy carrying scale (the mean flow), which is not acceptable in most type of bluff body flows, where the scales are continuously distributed from the smallest to the largest scales, thus rendering not so correct to vehicle aerodynamics.

DNS is the most accurate method to solve the NSE, resolving the whole spectrum of of scale motion, however it requires a prohibitive amount of computing resources, which renders it unusable for industry applications. RANS based models are very efficient solving the NSE, resolving only the mean value of the flow, the largest scales and modelling the entire cascade of energy, however at the cost of decreasing its accuracy. Large Eddy Simulation (LES) is a well known solution for the drawbacks of both methods, as it resolves the large scale motions, which contains most of the energy and the anisotropy of the flow, and it models only the small scales, which represent the isotropic part of the turbulence and are

responsible for dissipation. This way, the simulation time is reduced when compared to DNS and the accuracy is significantly improved when compared to RANS. To separate the resolved turbulence from its modeled counterpart, spatial filtering is used, which decomposes the instantaneous flow field in a resolved part $\overline{u}_i$ and an unresolved/ modeled part u'', which is called the sub grid scale (SGS),

$$u_i = \overline{u}_i + u''. \tag{2.9}$$

In LES, the filter width is defined by the mesh cell size, i.e. a box filter (implicit filtering), so it is imperative to design a fine grid accordingly to the problem settings, in order to obtain the anisotropic features of the flow and obtain an accurate prediction of the flow. For an accurate LES prediction, the filter width should be designed in such a manner that the cut-off frequency, k_c, is located in the inertial sub-range (see Fig. 2.1). According to Choi and Moin [29], the grid-point requirement for a well resolved LES rises with the Reynolds number with the power of $13/7$, which allows a more relaxed grid, leading to lower computational efforts when compared to DNS. However, LES only brings a slight resources cost decrease compared to DNS, and the computational costs of applying it to complete configurations such as an airplane, submarine, or road vehicle are still prohibitive, which leads to a more common use of RANS or URANS instead.

So, a model that is more efficient than LES while not compromising too much on its accuracy is still in need. In recent years a more recent concept is presented as the suitable solution, hybrid and bridging models that smartly blend LES/DNS and RANS approaches. The two main methods that follow this approach are the detached eddy simulation (DES) and the partially-averaged Navier Stokes (PANS) methods, which are the methods used in this thesis. The PANS method is more recent and it is still going through a fast process of validation, while the DES approach is one of the most, if not the most, famous hybrid method, already used in several industrial applications. The two methods present a very different concept, PANS is a bridging method which presents a smoothly alternating behaviour between DNS, where the mesh is fine enough and there is high turbulence, and RANS, where the mesh is coarser and the flow is undisturbed, using a filter in space and time. The DES has a very different approach, as it carefully transits between RANS and LES, behaving as its RANS base model near all regions in contact with no slip condition surfaces and where the grid is coarser, which should be the regions with less turbulence, and behaving as LES everywhere else, which are the regions of high turbulence and fine enough mesh. A more profound overview of both methods is presented in the next sections.

2.1.1 Partially Averaged Navier-Stokes

The PANS model was developed by Girimaji [30] with the goal to overcome the major defects of the URANS (Unsteady Reynolds Averaged Navier-Stokes) method. In the URANS method, the RANS equa-

tions are solved in a time-accurate fashion on relative fine grids with low initial turbulent kinetic energy and, therefore, low initial eddy viscosity. The URANS is intended to resolve smaller unsteady scales of motion than the ones typically averaged away in a steady-RANS simulation. However, it has been verified that the eddy viscosity of the unresolved scales get nonphysically large values, suppressing most temporal and spatial fluctuations in the resolved velocity field that would have been supported by the grid and temporal resolution. This is due to the URANS ratio of produced kinetic energy to dissipation (P/ϵ ratio) getting too high, making it incapable of resolving much of the fluctuations [31]. On the other hand, PANS solves the problem of getting physically inconsistent high values of eddy viscosity of the unresolved scales by modifying the coefficients of the parent RANS model in a physical correct manner according to the local resolution of the flow field in time and space, and the amount of resolved and unresolved fluctuations. This way, the method aims to maximize the resolved fluctuating scales, that are supported by a given grid and flow situation. This way, the PANS P/ϵ ratio allows the model to vary smoothly from RANS to DNS, depending on the values of its resolution control parameters. The parameters determining the RANS-to-DNS ratio are the unresolved-to-total ratio of kinetic energy, f_k, and the unresolved-to-total ratio of dissipation, f_ϵ. These parameters are computed at each point at the end of every time step and are then used as fixed values in the next iteration, which will be discussed afterwards.

The PANS model used in this study is the PANS $\zeta - f$, developed by Basara et al. [32], and further motivated by Basara et al. [33] and [18]. It uses the RANS $k - \epsilon - \zeta - f$ model as base. The RANS $k - \epsilon - \zeta - f$ was formulated by Hanjalić et al., [34], with the purpose to enhance the performance of the $k - \epsilon$ RANS model in the near wall region. This method falls into the so called elliptic-relaxation based eddy-viscosity models, where besides the k and ϵ equations, two additional ones are added. One for the velocity scale ratio, $\zeta_u = \frac{\overline{v^2}}{k_u}$, where $\overline{v^2}$ refers to the normal (to any no-slip boundary) fluctuating component of the velocity field, and the second for the relaxation fluctuation f. The introduction of the wall normal velocity $\overline{v^2}$ allows RANS to take into account the inviscid wall blocking effect while incorporating low Reynolds number effects in the viscous and buffer sub-layer of the turbulent boundary layer.

An overview of the PANS $\zeta - f$ follows here. The Incompressible Navier-Stokes equation for the instantaneous velocity (V) and pressure (p) fields is:

$$\frac{\partial V_i}{\partial t} + V_j \frac{\partial V_i}{\partial x_j} = -\frac{\partial p}{\partial x_i} + \nu \frac{\partial^2 V_i}{\partial x_j \partial x_j} \tag{2.10}$$

The PANS model takes the following decomposition:

$$V_i = U_i + u_i; \quad p = p_U + p_u. \tag{2.11}$$

The unresolved velocity, u_i, and unresolved pressure, p_u, are of background turbulence and are modeled, while $U_i =< V_i >$; $p_U =< p >$ are the partially-averaged (filtered) flow variables, and are resolved, where $< \cdot >$ denotes an arbitrary filter which is commutative with the spatial and temporal differentiation. This way, the PANS equation is written as:

$$\frac{\partial U_i}{\partial t} + U_j \frac{\partial U_i}{\partial x_j} = -\frac{\partial p_U}{\partial x_i} + \frac{\partial}{\partial x_j}\left(\nu \frac{\partial U_i}{\partial x_j} + \tau(V_i, V_j)\right) \tag{2.12}$$

where $\tau(V_i, V_j) =< V_i V_j > - < V_i >< V_j >$ is the subfilter scale (SFS) stress, which represents the effect of the unresolved scales on the resolved field, and it is closed by its anisotropic part using the eddy-viscosity (Boussinesq) assumption:

$$\tau(V_i, V_j) = -2\nu_u S_{ij} + \frac{2}{3} k_u \delta_{ij}. \tag{2.13}$$

In eq. 2.13, k_u is the unresolved (subfilter) turbulent kinetic energy, S_{ij} is the resolved stress tensor:

$$S_{ij} = \frac{1}{2}\left(\frac{\partial U_i}{\partial x_j} + \frac{\partial U_i}{\partial x_i}\right), \tag{2.14}$$

and ν_u is the viscosity of the unresolved scales, defined by:

$$\nu_u = C_\mu \zeta_u \frac{k_u^2}{\epsilon_u}. \tag{2.15}$$

In order to close the model, three transport equations for $k - \epsilon - \zeta$ and a Poisson equation, for the elliptic relaxation function of the unresolved velocity scales, are necessary. So, the PANS $\zeta - f$ model is constituted by the set of equations:

$$\begin{aligned}
\frac{\partial k_u}{\partial t} + U_j \frac{\partial k_u}{\partial x_j} &= P_u - \epsilon_u + \frac{\partial}{\partial x_j}\left(\frac{\nu_u}{\sigma_{k_u}} \frac{\partial k_u}{\partial x_j}\right) \\
\frac{\partial \epsilon_u}{\partial t} + U_j \frac{\partial \epsilon_u}{\partial x_j} &= C_{\epsilon 1} P_u \frac{\epsilon_u}{k_u} - C^*_{\epsilon 2} \frac{\epsilon_u^2}{k_u} + \frac{\partial}{\partial x_j}\left(\frac{\nu_u}{\sigma_{\epsilon_u}} \frac{\partial \epsilon_u}{j}\right) \\
C^*_{\epsilon 2} = C_{\epsilon 1} + f_k(C_{\epsilon 2} - C_{\epsilon 1}); &\qquad C_{\epsilon 1} = 1.4\left(1 + \frac{0.045}{\sqrt{\zeta_u}}\right) \\
\frac{\partial \zeta_u}{\partial t} + U_j \frac{\partial \zeta_u}{\partial x_j} &= f_u - P_u \frac{\zeta_u}{k_u} + \frac{\zeta_u}{k_u} \epsilon_u (1 - f_k) + \frac{\partial}{\partial x_j}\left(\frac{\nu_u}{\sigma_{\zeta_u}} \frac{\partial \zeta_u}{\partial x_j}\right) \\
L_u^2 \nabla^2 f_u - f_u &= \frac{1}{T_u}\left(c_1 + c_2 \frac{P_u}{\epsilon_u}\right)\left(\zeta_u - \frac{2}{3}\right),
\end{aligned} \tag{2.16}$$

where the last equation is the PANS Poisson equation for the elliptic relaxation function f_u, and $P_u = -\tau(V_i, V_j)\frac{\partial U_i}{\partial x_j}$ is the production of unresolved turbulent kinetic energy , which is closed by the previously introduced Bousinnesq assumption, Eq. 2.13. The constants in Eqs. 2.16 are:

$$C_\mu = 0.22; \quad C_{\epsilon 2} = 1.9; c_1 = 0.4; \quad c_2 = 0.65; \sigma_k = 1; \quad \sigma_\epsilon = 1.3; \quad \sigma_u = 1.2.$$

L_u and T_u are the length and time scales:

$$T_u = \max\left[\frac{k_u}{\epsilon}, C_\tau\left(\frac{\nu}{\epsilon}\right)^{1/2}\right]; \quad L_u = C_L \max\left[\frac{k^{3/2}}{\epsilon}, C_\eta\left(\frac{\nu^3}{\epsilon}\right)^{1/4}\right], \tag{2.17}$$

where

$$C_\tau = 6; \quad C_L = 0.36; \quad C_\eta = 85.$$

As previously stated, the parameters $f_{k,\epsilon}$ dynamically determine how much of the flow is resolved, as they vary between 0 and 1. In the PANS $\zeta - f$ set of equations, it was assumed that $f_\epsilon = \frac{\epsilon_u}{\epsilon} = 1$, which means that all the unresolved dissipation is assumed to be RANS dissipation and therefore modeled. This assumption is based on the fact that in most cases the small dissipative scales are unlikely to be resolved, since a computational grid beyond the inertial subrange, i.e. a near wall DNS resolution, would be required. This leaves only the crucial variable f_k to be chosen. When f_k assumes the value of one it makes the set of PANS $\zeta - f$ equations turn into the base RANS equations, assuming the value of zero makes it turn into the DNS approach, and assuming values in between makes it behave as mixture of RANS and DNS . As the influence of f_k on the resolved flow physics became clearer over time, its value evolved from being a fixed value to a dynamic parameter, where at every time-step the smallest value of f_k that a grid can support is calculated for every computational cell. In order to fulfill this, the following dynamic parameter was proposed:

$$f_k(x,t) = \frac{1}{C_\mu}(\frac{\Delta}{\Lambda})^{2/3}. \tag{2.18}$$

Where Δ is the geometric-average grid cell dimension, $\Delta = (\Delta x \cdot \Delta y \cdot \Delta z)^{1/3}$, and Λ is the Tayler scale of turbulence, which is computed as $\Lambda = \frac{(k_u + k_{res})^{1.5}}{\epsilon}$, where k_{res} is the resolved kinetic energy.

2.1.2 Detached-Eddy Simulation

The DES approach is one of the most, if not the most, famous hybrid method, already used in several industrial applications. It has shown to be successfully applicable to both research oriented, such as the supersonic flow on the base of a cylinder, and very complicated industrial and military applications, such as the flow around an airplane, [35]. Its application in predicting the flow around simplified vehicles, more specifically around the Ahmed's body, has been successfully proven by S. Kapadia *et al.*, [36], where the DES predicted drag is within 5 % of its measured value. The DES approach combines the LES approach with the RANS one, offering a reduced computational effort in comparison to LES, while maintaining much of the physical accuracy of the method. The basic concept of DES was first proposed

in 1997 by Spalart *et al.* [13], and it was based on a formulation employing the Spalart–Allmaras (SA) one-equation turbulence model. Since then, several other variants have been developed, based on other models such as the Standard Spalart-Allmaras RANS model, two equation models, such as $k-\epsilon$, and others. The way DES turbulence models are set up is: boundary layer and irrotational flow regions are solved using a base RANS closure model, while in regions of detached flow, it will behave as a basic LES subgrid scale model. This way, one gets the benefits of a RANS simulation in the boundary layers and of LES in the unsteady separated regions.

A famous problematic behavior of the standard DES has been reported by Menter and Kuntz [37], who showed a production of artificial separation for an airfoil simulation when refining the maximum cell edge length (h_{max}) inside the wall boundary layer below the critical value $h_{max}/\delta < 0.5 \sim 1$, where δ is the local boundary layer thickness. This effect was named Grid-Induced Separation (GIS), and it is caused by a sudden grid refinement, which makes the DES model to change from RANS to LES, without balancing the reduction in eddy-viscosity by resolved turbulence content, [38]. This is, in near-wall regions where the grid is so refined that the grid spacing, which is the filter width, becomes smaller than the RANS length scale, which is the wall-distance when using the SA model, that the model switches from RANS to LES mode, even though the grid is not refined enough according to LES requirements. This will decrease the turbulent viscosity and therefore the modeled stresses, as well as the resolved stresses, since the mesh is not fine enough for LES, leading the so called Modeled Stress Depletion (MSD), which can lead to premature separation, GIS. Solutions for this problem have been proposed, Menter et al. recommended using the $F1$ blending function of the SST-DES model to shield the boundary layers from the DES limiter. Following his steps, other blending functions for the same purpose have been suggested by Spalart et al. [39], with the name of Delayed DES (DDES). The DDES model, as originally proposed for the Spalart-Allmaras model, provided limited protection against GIS for two-equation models such as BSL, SST, and $k-\epsilon$. A further refinement is provided by the Improved DDES (IDDES) formulation of Shur et al. [40], a global wall-modeled LES approach, which allows RANS to be used in a much thinner near-wall region, where the wall distance is much smaller than the boundary-layer thickness, shielding against GIS, and providing some WMLES (Wall-modeled LES) capabilities to the DES formulation. This is done in order to use LES inside the boundary layer and RANS in the viscous region, bridging the gap between wall-resolved LES, where LES is applied all the way to the wall and current DDES like approaches, where RANS covers the whole boundary layer. Note that IDDES only switches to WMLES mode (branch) when the inflow conditions used in the simulation are unsteady, imposing some turbulent content, and the grid is fine enough to resolve boundary-layer dominant eddies, otherwise the DDES formulation (branch) is the one active, treating the boundary layer with RANS.

The variant of DES used in this project is the SST (Menter) $k-\omega$ Detached Eddy simulation, with an Improved Delayed DES (IDDES) formulation, through the STAR-CCM+ commercial code. The SST

(Menter) $k-\omega$ Detached Eddy model combines features of the SST $k-\omega$ RANS model in the boundary layers with an LES in unsteady separated regions. The standard SST model is a combination of the $k-\omega$ model with the $k-\epsilon$, in which the former is used in the inner part of the boundary layer and the latter is used in the outer part of the boundary layer and outside of it. In [41], Menter recognized that the ϵ transport equation from the Standard $k-\epsilon$ model could be transformed into the ω transport equation by variable substitution, and that this transformed equation is similar to the one in the Standard $k-\omega$ model, but with the additional non-conservative cross-diffusion term $\nabla k \cdot \nabla \omega$. So, the inclusion of this term in the ω transport equation potentially makes the $k-\omega$ model give identical results to the $k-\epsilon$ model. By using a blending function (which includes functions of wall distance) that includes the cross-diffusion term away from the walls, but not near them, it is possible to effectively blend a $k-\epsilon$ model in the far-field with a $k-\omega$ model near the wall, with just one pair of transport equations. The advantage of using these two different models in these specific regions is that the $k-\omega$ model has its strengths inside the boundary layer and its weakness outside of it, while the $k-\epsilon$ is the other way around. The main advantage the $k-\omega$ model has over the $k-\epsilon$ model is that it can be applied throughout the boundary layer, including the viscous-dominated region, without further modification, and its improved performance for boundary layers under adverse pressure gradients. However, in its original form, it has the big disadvantage of boundary layer computations being sensitive to the values of ω in the free-stream, which translates into extreme sensitivity to inlet boundary conditions for internal flows. This problem does not exist for the $k-\epsilon$ models, being then more favorable to use outside the boundary layer over the $k-\omega$ model. In addiction, the $k-\omega$ SST model has other benefits over its two base models, such as having a shear stress limiter (for ν_t reduction), which keeps the Reynolds shear stress terms from becoming too large in adverse pressure gradient regions, typically found on the top of an airfoil, [37].

Next, an overview of the formulation of the model IDDES SST $k-\omega$, used in commercial code of STAR-CCM+, will be presented as it is in its guide.

The base model in which it is set is the SST $k-\omega$ model, in which the transport equations for the kinetic energy, k, and the specific dissipation rate, ω, are:

$$\frac{\partial}{\partial t}(\rho k) + \nabla \cdot (\rho k \overline{u}) = \nabla \cdot [(\mu + \sigma_k \mu_t)\nabla k] + P_k - \rho \beta^* f_{\beta^*}(\omega k - \omega_0 k_0) + S_k \tag{2.19}$$

$$\frac{\partial}{\partial t}(\rho \omega) + \nabla \cdot (\rho \omega \overline{u}) = \nabla \cdot [(\mu + \sigma_\omega \mu_t)\nabla \omega] + P_\omega - \rho \beta(\omega^2 - \omega_0^2 k_0) + 2\rho(1-F_1)\sigma_{w_2}\frac{1}{\omega}\nabla k \cdot \nabla \omega + S_\sigma. \tag{2.20}$$

The $\overline{u}$ is the mean velocity, μ is the dynamic viscosity, k_0 and ω_0 are the ambient turbulence values that counteract turbulence decay, and S_k and S_ω are the user-specified source terms. f_{β^*} is the free-shear modification factor, which is a dissipation limiter that counteracts the $k-\omega$ model tendency to underpredict the production of ω in flows that are dominated by free-shear layers (such as jets or mixing

layers) or when free-stream turbulence is high. It is calculated as

$$f_{\beta^*} = \begin{cases} 1, & \text{for } \chi_k \leq 0 \\ \frac{1+680\chi_k^2}{1+400\chi_k^2}, & \text{for } \chi_k > 0 \end{cases}$$

where

$$\chi_k = \frac{\nabla k \cdot \nabla \omega}{\omega^3}$$

The P_k and P_ω are production terms, where $P_k = G_k + G_{nl}$ - G_k being the turbulent production, and G_{nl} the "non-linear" production:

$$P_\omega = \rho\gamma\left[\left(S^2 - \frac{2}{3}(\nabla \cdot \overline{u})^2\right) - \frac{2}{3}\omega\nabla \cdot \overline{u}\right]$$

$$G_k = \mu_t f_c S^2 - \frac{2}{3}\rho k \nabla \cdot \overline{u} - \frac{2}{3}\mu_t(\nabla \cdot \overline{u})^2$$

$$G_{nl} = \nabla \cdot \overline{u} : (T_{t,NL})$$

where the : represents a inner product of two tensors, γ is a model coefficient defined later in this section, f_c is the curvature correction factor, which incorporates the stabilizing and destabilizing effects usually associated with strong (streamline) curvature and frame rotation (to which the transport equation for the turbulent kinetic energy is insensitive, by construction), [43], $S = \sqrt{2S_{ij}S_{ij}}$ is the modulus of the mean strain rate tensor (with $S_{ij} = \frac{1}{2}\left(\frac{\partial \overline{u}_i}{\partial x_j} + \frac{\partial \overline{u}_j}{\partial x_i}\right)$ being the mean strain rate tensor), and $T_{t,NL}$ is a quadratic non-linear constitutive relation, which accounts for anisotropy of turbulence by adding non-linear functions of the strain and vorticity tensors. The third term of the right end side of the equation (2.20) is the before mentioned cross diffusion term, which makes the $k-\omega$ model behave like the $k-\epsilon$ model, and its influence on the model is controlled by F_1, the blending function responsible for changing the behaviour of the SST model between the $k-\omega$ and $k-\epsilon$ formulation by changing between the value 1 close to the wall, to 0 in the outer part of the boundary layer and outside of it, and is defined as:

$$F_1 = \tanh\left(\left[\min\left(\max\left(\frac{\sqrt{k}}{0.09\omega d}, \frac{500\nu}{d^2\omega}\right), \frac{2k}{d^2 CD_{k\omega}}\right)\right]^4\right), \tag{2.21}$$

where $CD_{k\omega}$ is the cross-diffusion coefficient, which is calculated by:

$$CD_{k\omega} = \max(\frac{1}{\omega}\nabla k \cdot \nabla \omega, 10^{-20}).$$

In the transport equations, (2.19) and (2.20), there are also present some model coefficients, σ_k, β^*,σ_ω, β and γ, which are calculated as:

$$
\begin{array}{lll}
\sigma_k = F_1\sigma_{k_1} + (1-F_1)\sigma_{k_2} & \sigma_{k_1} = 0.85; & \sigma_{k_2} = 1 \\
\beta^* = F_1\beta_1^* + (1-F_1)\beta_2^* & \beta_1^* = 0.09; & \beta_2^* = 0.09 \\
\sigma_\omega = F_1\sigma_{\omega_1} + (1-F_1)\sigma_{\omega_2} & \sigma_{\omega_1} = 0.5; & \sigma_{\omega_2} = 0.856 \\
\beta = F_1\beta_1 + (1-F_1)\beta_2 & \beta_1 = 0.075; & \beta_2 = 0.0828 \\
\gamma = F_1\gamma_1 + (1-F_1)\gamma_2 & \gamma_1 = \frac{\beta_1}{\beta^*} - \sigma_{\omega_1}\frac{k^2}{\sqrt{\beta^*}} & \gamma_2 = \frac{\beta_2}{\beta^*} - \sigma_{\omega_2}\frac{k^2}{\sqrt{\beta^*}}
\end{array}
$$

The SST $k-\omega$ model is equipped with a turbulent shear stress limiter which switches from a eddy viscosity model to the Johnson-King (JK) model for most of the adverse pressure gradient regions (wake region of the boundary layer), i.e. where the shear stress becomes excessively large, [44] and [45]. It is defined as:

$$\mu_t = \rho k T, \tag{2.22}$$

where T is the turbulent time scale, which is calculated using Durbin's realizability constraint, [46]:

$$T = \min\left(\frac{1}{\omega}, \frac{a_1}{SF_2}\right), \tag{2.23}$$

where $a_1 = 0.31$ is a model coefficient and F_2 is a blending function that ensures that the JK model can only be used in the boundary layer, and is calculated as:

$$F_2 = \tanh\left(\left(\max\left(\frac{2\sqrt{k}}{\beta^*\omega d}, \frac{500\nu}{d^2\omega}\right)\right)^2\right),$$

where d is is the distance to the wall.

The used DES formulation of the (Menter) SST $k-\omega$ model, using the IDDES approach, is based on the work of Shur et al., [40], and is obtained by replacing the specific dissipation rate, ω, in the transport equation for the turbulent kinetic energy, Eq. 2.19, of the RANS SST $k-\omega$ model, by $\tilde{\omega}$ defined as:

$$\tilde{\omega} = \frac{\sqrt{k}}{l_{\text{HYBRID}}\beta^* f_{\beta^*}}. \tag{2.24}$$

where l_{HYBRID} is the variable containing the filter that makes the model switch between the RANS and LES mode:

$$l_{\text{HYBRID}} = \tilde{f_d}(1+f_e)l_t + (1-\tilde{f_d})C_{\text{DES}}\Delta_{\text{IDDES}}. \tag{2.25}$$

l_t is the RANS length scale, which for the (Menter) SST $k-\omega$ is calculated as $l_t = k^{1/2}/(\beta^*\omega)$, which makes the RANS-LES switch dependent on the flow and not only on the grid, since it depends on k and ω. $C_{\text{DES}}\Delta_{\text{IDDES}}$ is the LES length scale, where $\Delta_{\text{IDDES}} = \min(\max(0.15d, 0.15\Delta, \Delta_{min}), \Delta))$ is the altered SGS filter of LES used, where d is the distance to the wall, Δ is the largest distance between the cell center under consideration and the cell centers of the neighboring cells and Δ_{min} is the smallest distance between the cell center under consideration and the cell centers of the neighboring cells. Unlike

the usual LES and DES approaches, this new definition of the subgrid length-scale includes explicit wall-distance dependence, and not only the grid-spacings. As previously stated, the IDDES approach is constituted by two branches, one that is the WMLES mode, which is only activated when the inflow conditions used in the simulation are unsteady and impose some turbulent content and the grid is fine enough to resolve boundary-layer dominant eddies, and other which is the DDES mode. The WMLES branch is introduced to the length scale calculation, Eq. 2.25, by the blending function f_B and the so-called "elevating" function, f_e. The function f_B is only dependent on the grid construction, as its definition is:

$$f_B = \min\left[2\exp(-9\alpha^2), 1\right] \tag{2.26}$$

$$\alpha = 0.25 - \frac{d}{\Delta}$$

and it varies from 0 to 1, while providing rapid switching of the model from RANS mode (f_B = 1) to LES mode (f_B = 0) within the range of wall-distance $0.5\Delta < d < \Delta$. f_e has the aim of preventing the excessive reduction of the RANS Reynolds stresses, observed in the interaction of the RANS and LES regions, in the vicinity of their interface, combating this way the log-layer mismatch. f_e is defined in a way that it is close to zero (passive) in two occasions:

- when the grid used is sufficient for a wall-resolved LES (the interface between RANS and LES occurs very close to the wall, $y^+ < 15 \sim 20$, making the Reynolds stresses near the interface negligible);
- when the model performs as the background RANS model.

Such requirements are met by using the following definition:

$$f_e = \max[(f_{e_1} - 1), 0]\psi f_{e_2}, \tag{2.27}$$

where the introduction of the function ψ is purely empirical and f_e is only active in the RANS simulation region, i.e. where $f_B = 1$. f_{e_1} is the shape function of f_e , while the amplitude of f_e depends on the solution field, and is given by f_{e_2}. This component is built of sensor functions for the viscous sublayer and for the modeled log-law region, r_{dl} and r_dt respectively.

$$f_{e_1} = \begin{cases} 2\exp(-11.09\alpha^2), & \text{if } \alpha \geq 0 \\ 2\exp(-9\alpha^2), & \text{if } \alpha \leq 0 \end{cases}$$

$f_{e_2} = 1 - \max(f_t, f_l)$ controls the intensity of "elevating" of the RANS component of the model through the functions:

$$f_t = \tanh[(C_t^2 r_{dt})^3]; \quad C_t = 1.87; \quad r_{dt} = \frac{\nu_t}{\sqrt{\nabla u : \nabla u^T k^2 d^2}}$$

$$f_l = \tanh[(C_l^2 r_{dl})^1 0]; \quad C_l = 5; \quad r_{dl} = \frac{\nu}{\sqrt{\nabla u : \nabla u^T} k^2 d^2}$$

where $k = 0.41$ is the Von Karman constant. C_l and C_t are specific constants from the model, which are tuned so that f_{e_2} is virtually zero when either f_t or f_l are close to unity. The function $\tilde{f_d}$ is the blending function that combines the WMLES and DDES branches of the model and is defined as:

$$\tilde{f_d} = \max((1 - f_{dt}), f_B), \tag{2.28}$$

with $f_{dt} = 1 - \tanh\left[(C_{dt} r_{dt})^3\right]$, where $C_{dt} = 20$ is a mode coefficient.

As shown in [40], in simulations with inflow turbulent content: $r_{dt} \ll 1$; f_{dt} is close to 1.0; $\tilde{f_d}$ is equal to f_B; autommaticaly reducing to the WMLES branch. Otherwise, f_e becomes zero, and (2.25) reduces to the DDES formulation, $l_{\text{HYBRID}} = l_{\text{DDES}} = \tilde{f_d} l_{\text{RANS}} + (1 - \tilde{f_d}) l_{\text{LES}}$, which is equivalent to the original DDES, [47].

2.2 Truck aerodynamics

The aerodynamics of a vehicle plays a major role in vehicle development, as it affects the cooling, handling, performance, noise, comfort, safety and fuel economy of it. This thesis focus on the fuel economy, as the aerodynamic drag represents a major part of the tractive resistance, accounting for at least 60% of the total power consumed by a heavy-duty vehicle at highway cruise speeds, making it the most responsible for energy loss, [1]. Choi et al. [1] provides a good description of a tractor-trailer aerodynamics and some of the simplified truck models developed for its studies, which are represented in Fig. 2.2. Two of the most popular simplified models are the ground transportation system (GTS), [48], and the generic conventional model (GCM), [49], where the GTS is the most simplified version, as there is no gap between the tractor and the trailer and is striped out of real geometrical features, while the GCM presents the gap between the tractor and the trailer and has a Cab-Over-Engine (COE) arrangement of the tractor unit. Each of the models was later modified into a more realistic version, the modified GTS (M-GTS), [50], and the generic modified GCM (M-GCM).

For the static zero yaw angle, the models show a similar flow topology, where the incoming flow stagnates near the front grill of the tractor and separates at the trailing edge of the tractor body, forming counter-rotating vortices trapped inside the gap, between the tractor and the trailer (except in the GTS). The flow on the gap is of great importance, as the drag varies greatly with different gap clearances. Gap flow and C_d trends on the gap depending on the gap clearance can be seen in [51]. In the Hammache et al. work, [51], DPIV experiments of a simplified tractor-trailer model similar to the M-GTS model, but without wheels, present intermittent symmetry breakdown in the gap between the tractor and trailer, for certain gap widths, in a constant zero yaw angle configuration. After the gap, the flow travelling above

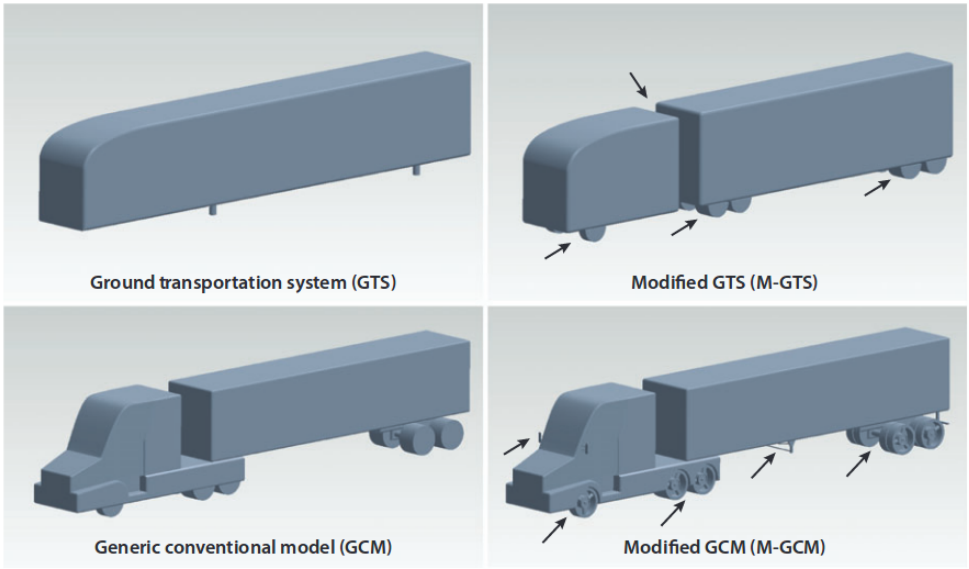

Figure 2.2: Simplified tractor-trailer models: ground transportation system (GTS), generic conventional model (GCM), and their modifications (M-GTS and M-GCM). Figure from [1].

the trailer top surface remains attached and then separates at its trailing edge, resulting in a large wake with a significant pressure drop. There, separating shear layers develop at the trailing edges of the trailer which roll up into vortex rings. The vortex topology at the rear wake depend on the ground clearance of the model, and it is described in 65.

2.3 The concept of Drag

The total aerodynamic drag is given by the sum of skin friction and pressure drag. Both components are a direct effect of viscosity. As a viscous flow interacts with a wall, it develops a velocity gradient $\frac{\partial u}{\partial y}$ due to the no-slip condition. This induces shear stress that acts on the surface of the body. The skin friction drag is given by the integration of this shear stress at the surface in the flows' free-stream direction:

$$D_f = \int \tau_w \, dS. \tag{2.29}$$

Pressure drag is caused by the pressure difference between the front and rear surfaces of an object, associated with the formation of a wake in the rear end of a body, due to flow separation induced by a strong adverse pressure gradient. It is calculated as:

$$D_p = \int (p - p_\infty) \, sin\alpha \, dS, \tag{2.30}$$

in which α is the angle angle of the pressure with the tangent of the and p_∞ is the atmospheric pressure. So, the total drag is given by:

$$D_{tot} = D_f + D_p. \tag{2.31}$$

More often, the drag force is defined as:

$$D = \frac{1}{2}\,\rho\, U_\infty^2\, C_d\, A. \tag{2.32}$$

It depends on the shape of the body, related by the drag coefficient C_d and the cross sectional area A, density of the flow ρ and the free-stream velocity U_∞. Since we have no control over the air density and the cross sectional area of a truck shouldn't be reduced, since it affects its capacity to transport goods, the only way to reduce losses due to drag resistance is by lowering the C_d. All road vehicles fall into the category of bluff bodies, which is a body that produces a wake comparable to its characteristic dimension. In bluff bodies the contribution of the skin friction is much lower than that of pressure, so emphasis needs to be on minimizing pressure drag. This means guaranteeing that the flow stays attached over as much of the body surface as possible and raising the pressure in the large separated region at the rear of a vehicle. For this, it is essential to know what are the main sources of drag in a truck. As depicted in Fig. 2.3, it is the front of the tractor, the gap between the tractor and the trailer, wheel-housing and wheels, the under-body and majorly the trailer wake region [[4], 5].

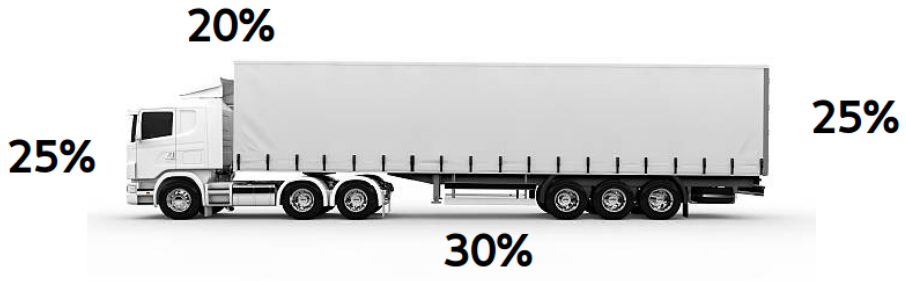

Figure 2.3: Distribution of aerodynamic drag for a heavy vehicle tractor-trailer truck.

2.4 Flow Control

Being able to control the flow around a vehicle enables us to reduce its C_d, achieving that way the aerodynamic efficiency required to meet the today's need of sustainable transportation. A semi-trailer truck usually have a C_d value of 0.5 - 0.7, which is double the one of a passenger car, 0.25 - 0.35. Trucks are designed to carry a maximum volume of goods or of payload. The restrictions presented by design regulations for trucks constrict its dimensions limiting the flexibility needed to solve aerodynamic issues, without affecting negatively its load capacity. Before the oil crisis of the early 1970's most designers of

heavy duty trucks didn't take aerodynamics into consideration. The top concern was ease of fabrication and avoidance of round corners, due to diminish inside volume, which led to very aerodynamically inefficient trucks. Only when the crisis started, bigger consideration for aerodynamics was taken. Since then, a broad research on heavy duty trucks have been achieved and it is still an active area. The implementation of add-ons and design alterations such as smoother front corners of the cabin, rounded edges trailers, cab extenders and trailer splitter plate for the cabin-trailer gap, skirts and underbody wedges for the wheels and underbody, boat-tail plates and flaps for the trailer base, and other devices studied on [1], have shown to improve significantly trucks' aerodynamic efficiency. All the solutions mentioned before are considered as passive flow control, i.e. geometrical modifications or add-ons applied to control the flow or to generate a specific behaviour, without any energy supply. Active flow control (AFC) presents critical advantages when compared to passive techniques. It independently (energy wise) controls the natural stability of the flow using a small, localized energy input and it can adapt to different flow conditions, which is highly advantageous since it gives the possibility to match the real conditions of the flow. The latter is referred to as reactive flow control where the state of a variable is measured and used in the control process. If the measured variable is also the one being controlled, it is classified as closed loop control, otherwise it is classified as open feed-forward loop control. Alternatively to reactive flow control, there is Predetermined active flow control, also called open-loop active flow control, where as input we have a predetermined energy input, without adapting to the exterior flow[4].

As a flow travels through a solid surface against an adverse pressure gradient, the speed of its boundary layer relative to the surface starts to decay to zero and tends to detach from the surface, creating a re-circulation bubble. The AFC injects unsteady localized energy into the turbulent boundary layer, before the separation point, delaying or even suppressing its separation. The AFC technique applied in this thesis is a synthetic zero net mass flux jets, where the fluid necessary to actuate on the boundary layer is intermittently injected through orifices and is driven by the motion of a diaphragm sealed underneath the surface.

3

Methodology

The work done in this thesis was divided into three steps: the development of the model and meshes, solving of the computational domain and post-processing of the simulation results. For these three steps, commercial softwares were used: Ansys ICEM-CFD for the geometry and mesh generation, AVL Fire and STAR-CCM+ to run the PANS and DES simulations, respectively, and Ansys EnSight and Matlab for the post-processing.

3.1 Geometry and Domain

The geometry and domain of the body were both drawn using the software ICEM-CFD. The geometry of the model is represented in Fig. 3.1. It is a simplified two-bodied truck model constituted by two simple rectangular prisms: a cabin with round corners at the top and A-pillars, and a trailer with rounded front pillars, which is based on the model used in [8] and [9]. The use of a simplified model facilitates the grid generation and avoids flow complexities. The coordinates system origin is located at the middle of the trailer front surface. All static simulations have the same model, with the same geometry and dimensions. All dimensions are normalized by the characteristic length, which is chosen to be the width

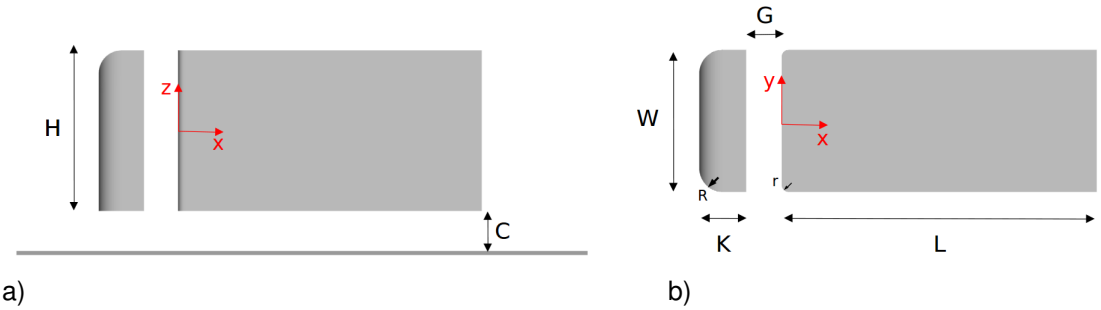

Figure 3.1: The model geometry.

of the truck, W, which has the value of 0.4 m for the static simulations. Both cabin and trailer have the same width, the height, $H/W = 1.1675$, and ground clearance, $c/W = 0.167$. The cabin has a length of $K/W = 0.33$ and a gap to the trailer of $G/W = 0.25$, while the trailer has a length of $L/W = 2.22$. Both Static and dynamic simulations use the same domain dimensions and positioning of the model. The domain dimensions are based on the closed circuit wind tunnel at Chalmers University of Technology. The domain is represented on Fig. 3.2, and it presents a width of $T/W = 9$, an height of $P/W = 6.25$ and a length of $B/W = 29.65$, which considering the model's width it gives a blockage factor of about 2.1%, which is well below 5%. The front face of the cabin is located at $X_1/W = 9.367$ from the channel inlet and the base surface of the trailer is located at $X_2/W = 17.507$ from the outlet.

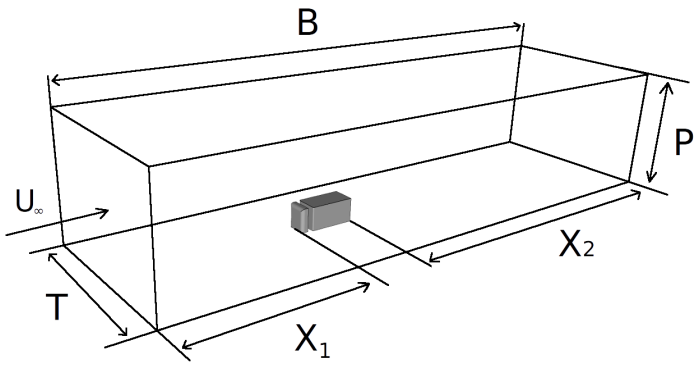

Figure 3.2: The computational domain.

3.2 Computational grids and near-wall resolution

A total of four different meshes were created, three for the static simulations and one for the dynamic simulations. The structured grids were built using the commercial grid generator software Ansys ICEM-

CFD and are constituted of only hexahedral elements. This software has available two important mesh generating tools, the blocking and the O-grid tools, which allow to concentrate the cells in the most important sections of the domain, such as near the truck's surface and on the wake. This allows to have coarser cell sizes in less important regions and to have a good control of the cells' growth from the surfaces solid.

An horizontal cut of the medium refinement grid used in the static simulations is represented in Fig. 3.3.

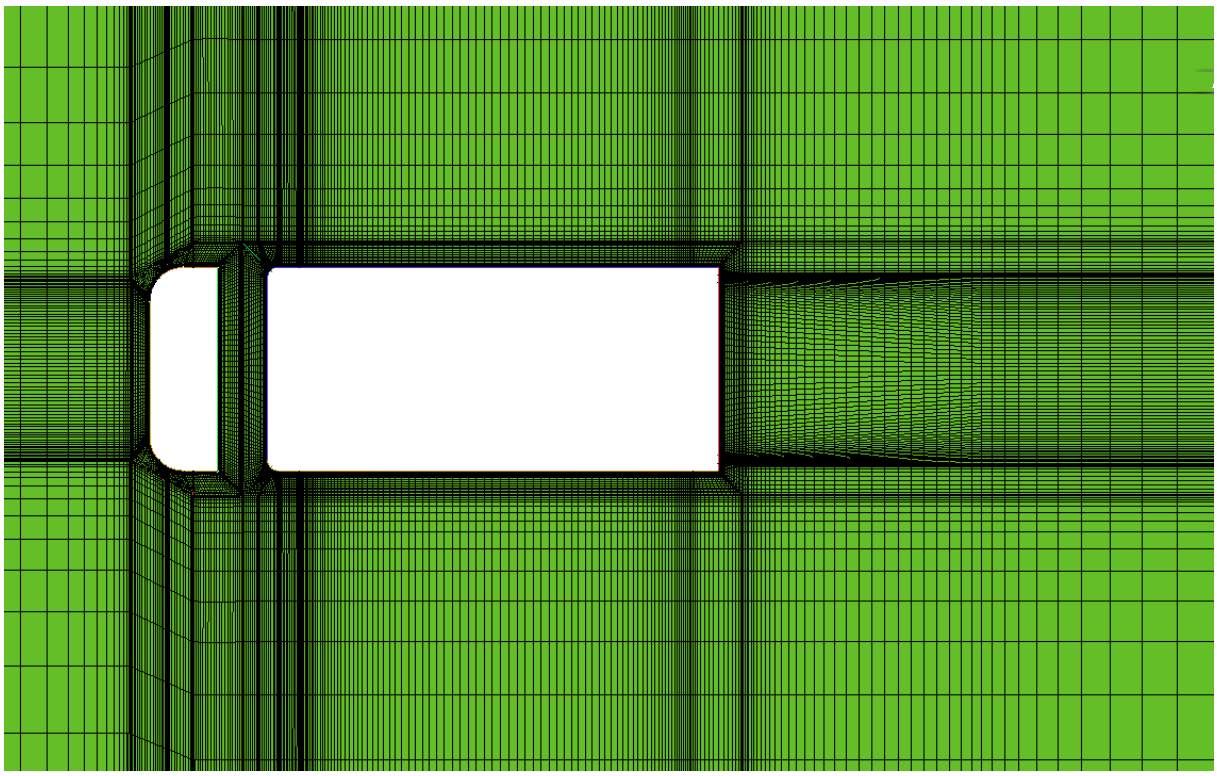

Figure 3.3: Top view of the medium refinement grid.

Around the model, in order to have a well resolved boundary layer and that way reliable results, the grids have to be properly built. To assure that, the cell sizes have to be such that the wall normal resolution is lower than one, $n^+ < 1$, so that the three regions of the turbulent boundary layer, viscous layer, buffer layer and log-law region are captured. According to Piomelli, [52], for a good LES resolution, the resolution in the streamwise direction, Δ_s^+, should be lower than $50 - 150$ and the resolution in the spanwise direction, Δ_l^+, should be lower than $15 - 40$. For a good RANS resolution, Δ_s^+ should be lower than 1000 and Δ_l^+ should be lower than 200. For PANS a good resolution is something in between the

two. This three parameters are computed as:

$$n^+ = \frac{u_\tau n}{\nu}, \tag{3.1}$$

$$\Delta_s^+ = \frac{u_\tau \Delta_s}{\nu}, \tag{3.2}$$

$$\Delta_l^+ = \frac{u_\tau \Delta_l}{\nu}, \tag{3.3}$$

where $u_\tau = \sqrt{\frac{\tau_{wall}}{\rho}}$, τ_{wall} being the wall shear stress, n the distance from the center of the first cell to the nearest wall and ν the kinematic viscosity.

In this work, all grids have a $n^+ < 1.3$, $\Delta_s^+ < 630$ and $\Delta_l^+ < 358$. Only in a portion of the front pillars of the trailer and some punctual spots on the cabin the y^+ resolution reaches higher values. Also, the spanwise and streamwise resolution is well bellow the LES requisites in regions of higher importance such as corners and regions close to the gap and wake.

The details of three computational grids are reported on table 3.1.

Case	Coarse mesh	Medium mesh	Fine mesh
Number of cells (Million)	3	5.1	7.9
n^+_{max}	3.7	3.1	2.9
n^+_{mean}	0.344	0.346	0.341
$\Delta_{s}{}^+_{max}$	630	465	374
$\Delta_{l}{}^+_{max}$	358	286	240

Table 3.1: Details of the computational grids.

The dynamic simulations were ran using a grid very close to the medium refinement mesh of the static case.

The use of this resolutions in cases of similar geometry, domain, conditions and with the same characteristic length, W, using PANS, have previously been validated in the study of bluff body flows, [20], application of AFC on a generic truck cabin, [6], and the application of AFC on a oscillating truck cabin, [3].

3.3 Numerical set-up

All simulations use a time step of $\Delta t = 5\text{x}10^{-5}$ s, which gives a CFL number, $CFL = \frac{U_\infty \Delta t}{\Delta x}$, lower than 1, in all the domain, providing a good time accuracy. Although the Reynolds numbers used to simulate a truck in real conditions is around 3 million, the current simulations are set with a Reynolds number of $Re = 2.5 \times 10^5$, based on the inlet velocity $U_\infty = 9.438$ m/s, and the width of the model, $W = 0.4$ m, which

already gives a fully turbulent flow. This reduction in Reynolds number is due to the limited availability of computational resources, since it leads to a lower cell count. In all static simulations, the averaging of the flow was started after 2 simulation seconds, which correspond to two flow passages through the channel domain, allowing the flow to be fully developed. The flow was averaged for 3 seconds, which correspond to three passages.

For all static simulations, the following boundary conditions were applied: An inlet condition at the entrance of the domain with a constant, normal to the surface velocity of $U_\infty = 9.438$ m/s; a symmetry condition for both side walls and the roof of the channel; an homogeneous Neumann boundary condition, $gradient = 0$, was set for the outlet, since given the model dimensions, the inlet conditions and the large distance between the model and the outlet, it is fair to consider that the flow as fully developed at the end of the channel; no-slip condition boundary condition was applied to all the surfaces of the truck model as well as to the floor. However, in order to save resources, higher than one y^+ values were set on the ground in order to lead the PANS model into modeling the boundary layer there, instead of trying to resolve it, and taking advantage of the hybrid wall-treatment. The initial conditions were set as the inlet velocity. Instead of trying to model the laminar-to-turbulent transition, a small level of turbulence ($k = 0.003\ m^2/s^2$, $\epsilon = 0.25\ m^2/s^3$) is introduced at the inlet, turning the flow fully turbulent.

3.3.1 Creating the Dynamic Case

For the dynamic simulations the width of the trailer was changed to $W = 0.45$ m, in order to give a bigger separation at the trailer front pillar, setting this way a model where the application of AFC can be more beneficial. The mesh used was derived from the medium refinement mesh of the static simulations. Two dynamic simulations were conducted, one with AFC application and one without. The simulation of the dynamic truck oscillation in the yaw direction between the two extreme angles was implemented by changing the inlet, roof and side walls boundary conditions to an inlet boundary condition with a specified u and v velocity varying in time. To define the oscillation formula for the boundaries, two main parameters that describe this oscillation have to be set. The first one is the oscillation frequency, which is set to have a Strouhal frequency of $S_t = \frac{fW}{U_\infty} = 0.1$, where f is the oscillation frequency in Hz, W is the trailer width and $U_\infty = 9.438$ m/s is the module of the inlet velocity. The second one is the range of the yaw angle, $-10° < \beta < 10°$. These choices are supported by experiments performed in on-road conditions [53, 54, 55], which give $0.06 < S_t < 0.9$ as important frequencies, and a lateral wind speed of around 4-5 m/s [53], which leads to the chosen yaw angle range. These parameter were also chosen to match the ones in [3], which studies the application of AFC in the A-pillars of an oscillating truck cabin, where the model has a similar geometry and the same AFC Strouhal actuation frequency. The dynamic

oscillation is then described by a sinusoidal oscillation which is given by the formulas:

$$u = 9.366 + 0.0717\cos(8.4\pi(t - t_0)), \quad v = 1.6389\sin(4.2\pi(t - t_0)), \tag{3.4}$$

where u and v are the streamwise and spanwise velocities set on the boundaries, t is the time and t_0 is the time the oscillation started in the simulation. For both dynamic simulations, 0.5 s (half of a flow through passage) were ran with the static settings, after which the dynamic conditions were implemented. The results started being averaged after one full sweeping cycle and were ran for two more cycles.

3.3.2 AFC application

In an attempt to decrease the separation on the front pillars of the trailer, AFC is applied in the dynamic configuration. The AFC applied is a zero net mass flux pulsating synthetic jet, applied through a 1.01 mm slot, in the direction normal to the surface, as represented in Fig. 3.4. The suction and blowing of the synthetic jet actuator is simulated through an inlet boundary condition with a time varying velocity normal to the surface given by the sinusoidal equation

$$U_{AFC} = 0.26U_\infty \sin(t2\pi f_a), \tag{3.5}$$

where f_a is the actuation frequency. f_a is chosen based on [3], where the application of the same type of AFC with a reduced frequency of $F^+ = \frac{f_a}{U_{inf}/W} = 3.1$ is applied in the A-pillars of an oscillating truck cabin, with a successfully omission of separation on the A-pillar and resulting in a considerable C_d reduction. The use of the same reduce frequency, with a $W = 0.45$ m leads to an actuation frequency of $f_a = 65Hz$.

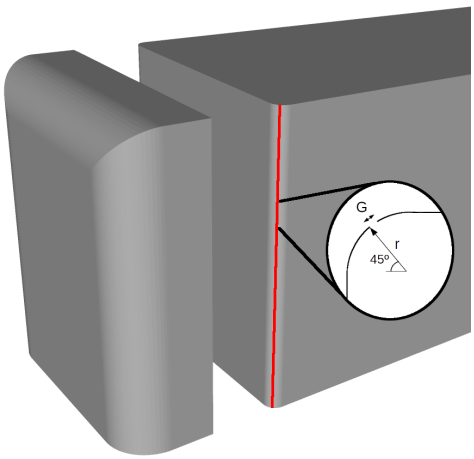

Figure 3.4: Representation of the top view of the AFC slot.

3.3.3 Solver parameters

In this work PANS and DES were used as the solving methods for the numerical simulations. The static simulations were solved using both PANS and DES while the dynamic simulations were solved using only PANS. The PANS method was applied using the commercial finite-volume based CFD software AVL-Fire, and the DES method was applied using STAR-CCM+.

For both methods, a hybrid wall-treatment was chosen and the time marching procedure was done using the implicit second order accurate three time level scheme,

$$\left(\frac{\partial \phi}{\partial t}\right)_{n+1} = \frac{3\phi_{n+1} - 4\phi_n + \phi_{n-1}}{2\Delta t}, \tag{3.6}$$

which uses the solution at the current time level, $n+1$, as well as the solutions from the previous two time levels, n and $n-1$, in a backward differentiation formula.

In PANS simulations, the continuity equation have been discretized with central differencing scheme (CDS), the turbulence equations with the second order upwind scheme MINMOD to approximate the convective fluxes, [56], and the momentum equation with the second order upwind scheme AVL SMART Bounded, [57]. Under-relaxation factor parameters were introduced in order to guarantee the stability of the equations: 0.6 for the momentum equation, 0.1 for the pressure, 0.4 for the turbulent kinetic energy equation and 0.4 for the dissipation rate. A maximum of eight iterations for each time-step was imposed.

For the DES simulations, a segregated solver with Hybrid Second-Order Upwind/Bounded-Central discretization scheme is used. The under-relaxation factor parameters are 0.8 for the momentum equation, 0.2 for the pressure and 0.8 for both kinetic and dissipation equations.

3.4 Streamlines and flow patterns

Streamlines represent the path that massless fluid elements will travel at any instant in time, and it is always tangent to the velocity vector of the flow. This way, it is used to visualize the flow patterns, which can reveal points where the streamline slope is indeterminate , i.e. all the spatial derivatives of the velocity are zero, the so called critical points. The analysis of these points help explain the features of the flow. There are three kinds of critical points that can be formed: foci, unstable nodes and saddle points, from which the first two can be stable or unstable. The streamlines can also form negative (NBL) and positive (PBL) bifurcation lines, where the first one indicate flow separation from a no-slip surface and the second reattachment. Unstable nodes indicate a stagnation point on a surface, saddle points indicate that two streams of opposite directions collide and form new streams, and unstable focus indicate the presence of a vortex. The method used in Ensight to trace streamlines is explained on [58]. All bifurcation lines and critical points are represented in Fig. 3.5.

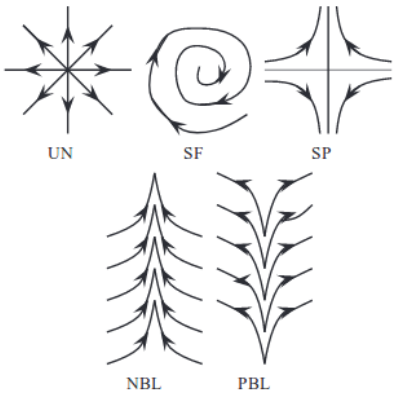

Figure 3.5: Critical points and bifurcation lines. UN is an unstable node, SF is a stable focus, SP is a saddle point, NBL is a negative bifurcation line and PBL is a positive bifurcation line, [59].

3.5 Q-invariant

In order to identify a vortex it is first necessary to define it. [60] defines it as an area where the irrotational strain is small compared to the vorticity. This described as the second invariant of the deformation tensor, II, being smaller than a negative threshold value. However, the Q-criterion is usually described as $Q = -II$:

$$Q = \frac{1}{2}\left(\left(\epsilon_{ijk}\frac{\partial v_k}{\partial x_j}\right)^2 - \left(\frac{\partial v_i}{\partial x_j} + \frac{\partial v_j}{\partial x_j}\right)^2\right), \tag{3.7}$$

where the first term, $\epsilon_{ijk}\frac{\partial v_k}{\partial x_j}$ is the vorticity and $\frac{1}{2}\left(\frac{\partial v_i}{\partial x_j} + \frac{\partial v_j}{\partial x_j}\right)$ is the symmetric strain tensor.

4

Results

As pointed out in section 3.2, it is already confirmed that it is appropriate to use the resolutions used in the present work with hybrid RANS-LES/DNS methods to accurately describe the flow around simplified vehicles. This chapter begins with the comparison between both bridging and hybrid methods, PANS and DES, results for three levels of mesh refinement. To analyze the influence of coarsening and refining the mesh on the hybrid methods' ability to accurately predict the flow characteristics, three meshes with 3, 5 and 8 million nodes are used. The same meshes were used with both methods. The comparison includes the analysis of the force coefficients of the truck and its two constituent bodies, surface pressure coefficient profiles and surface pressure visualization, velocity and velocity fluctuation profiles comparison on the model and on the wake with comparison to experimental results, and analysis and comparison of flow structures and behaviour, with comparison to experimental results.

After the comparison between both methods and the analysis on the coarsening procedure, the medium refinement mesh along with the PANS method, was chosen to perform the dynamic simulations, where the continuous yawing movement of the body, between -10° and 10°, is simulated. Afterwards, an active flow control actuation is introduced to the yawing configuration, as an attempt to stabilize the flow around the truck, improving its dynamic efficiency.

4.1 Static Results

As presented in the literature review section, PANS and DES are bridging URANS - DNS and hybrid URANS-LES turbulent models, respectively, which are increasingly being used for simulating turbulent flows with large-scale unsteadiness, like the exterior flow around simplified vehicles. In this section, the results from the application of each method in the same study settings and with the same meshes are presented, analyzed and compared.

4.1.1 Force coefficients

When it comes to engineering application, one of the flow features of most interest are the quantitative values of the forces coefficients, mainly the total drag coefficient when it comes to vehicle aerodynamics. In this section, the averaged values of drag and lift coefficients, obtained in the six simulation variations, are presented. In all cases the coefficients started being averaged after 2 seconds of simulation, corresponding to 2 flow passages through the simulation domain, until 5 seconds. In all simulations the whole truck was simulated and the force coefficient values were calculated for each body separately, and later summed.

4.1.2 Drag Coefficient, C_d

Grid	Cabin	Trailer	Truck
Coarse DES	0.7121	-0.2321	0.4800
Medium DES	0.707838	-0.2329	0.4749
Fine DES	0.6876	-0.2096	0.4780
Coarse PANS	0.7020	-0.2436	0.4585
Medium PANS	0.7039	-0.2390	0.4648
Fine PANS	0.6706	-0.2143	0.4564

Table 4.1: Mean values of C_d.

The mean values of the drag coefficient can be seen in Table 4.1. By comparing the mean value of the full truck's C_d between meshes, the coarse has a difference of less than 0.5% when compared to the fine mesh for both PANS and DES models, and the difference between the methods for each mesh is always below 5%. Showing a very close degree of accuracy in predicting C_d between the different meshes and between methods. Although the full truck total C_d is the most important result, it is also interesting to understand for which body the methods give more different results between meshes. We can see that the highest C_d difference between meshes comes from the trailer, where the difference between the coarse and the fine mesh is around 11.1% with the DES method and around 11.5% with PANS, while the cabin always shows a difference below 5% for both methods. The same is true when

comparing the C_d values between methods for the same mesh, where the trailer presents a difference always below 5% and the cabin, a difference below 2.5%. Overall, the C_d values resulting from both methods, are very close to each other, across the three meshes.

By proving both methods give similar predictions of C_d across the coarse, medium and fine mesh, this section also serves as a mesh independence study, as the difference between different meshes results for the same method are low.

4.1.3 Lift Coefficient, C_l

The drag coefficient is the most relevant value relating aerodynamics performance with fuel efficiency, however the lift coefficient is also of great importance since it is directly connected with vehicles traction, stability and overall dynamic performance.

Grid	Cabin	Trailor	Truck
Coarse DES	0.1728	-0.3206	-0.1477
Medium DES	0.1773	-0.3244	-0.1471
Fine DES	0.1766	-0.3293	-0.1527
Coarse PANS	0.1327	-0.2822	-0.1495
Medium PANS	0.1905	-0.3198	-0.1293
Fine PANS	0.1923	-0.3321	-0.1398

Table 4.2: Mean values of C_l.

Table 4.2 presents the mean values of lift coefficient. For the full truck, the mean value of C_l obtained with the coarse mesh has a difference of around 3.3% when compared to the fine mesh for DES models. For the PANS the difference is of around 6.9%. However, for PANS, when comparing the medium mesh truck's C_l with the fine mesh, we get a difference of 15.6% which is considerably higher but still acceptable. Still for PANS, the difference between coarse and fine mesh is -31% and -15% for the cabin and trailer respectively, and -0.88% and -3.7% between medium an fine mesh for the cabin and trailer respectively. All in all, we can say that the C_l values are considerably closer between meshes for the DES calculations than for PANS.

When comparing the results from the fine mesh between the two turbulent models we get a difference for the full truck of 9.2%, while -8.1% and -0.8% difference for the cabin and trailer, respectively. As for the medium mesh, around 13.8% difference for the truck and 7% and 1.5% for the cabin and trailer, respectively. For the coarse mesh, although the difference of the full truck's C_l between the two models being very low, -1.2%, the difference between each truck's body is reasonably higher for the cabin, 30%, while 13.6% for the trailer.

4.1.4 Velocity and Reynolds stress profiles

4.1.4.A Trailer

In order to better understand how differently both methods treat the boundary layer and how they react when coarsening and refining the mesh, three probe lines were created, distributed along the right side face of the trailer at $x^* = x/W = 0.05$, $x^* = 0.75$ and $x^* = 2$ in the $Z = 0$ plane, with the direction normal to the body's surface, as represented in Fig. 4.1. The value of mean velocity in the x and y direction and the mean Reynolds stresses $\overline{u'u'}$ and $\overline{v'v'}$ were recorded after 5 passages for each method and mesh, and are presented in figures 4.2 and 4.3, respectively.

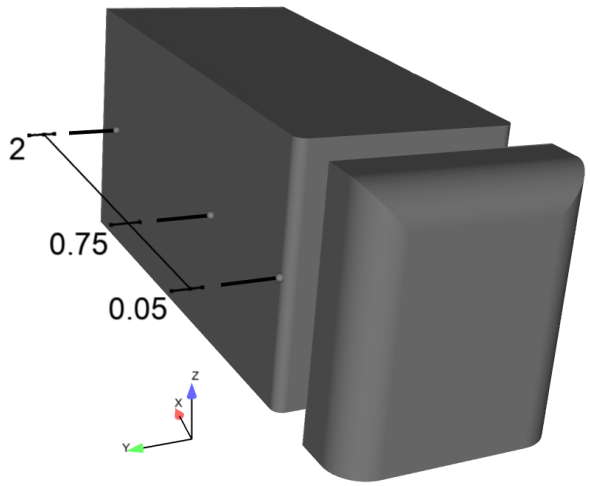

Figure 4.1: Representation of probe lines and its x location (normalized by W)

Analyzing figure 4.2, we can see a much better agreement between meshes for the DES results, with its u and v velocity profiles almost perfectly overlapping along the whole probe, for both velocity components, shows a very good convergence of the meshes. As the flow evolves from the beginning of the trailer to the end, the results between the methods present a more similar velocity profile. We can see that the span-wise velocity, v, profiles are more similar between methods than the stream-wise velocity, u, ones, and that for lower values of y the profiles between methods are more different, however eventually starting to overlap as the distance from the wall increases. For PANS, the profiles resultant from the medium and fine mesh show a very good agreement, noting a good convergence of the meshes, specially when we start moving towards the end of the trailer, for both u and v components. The v profile at $x/W = 2$ of the medium and fine mesh almost overlap, while the coarse mesh results are noticeably different. This shows that the DES model presents better agreement between meshes, when it comes to obtaining velocity profiles, and hints that DES can support coarser meshes than PANS, while

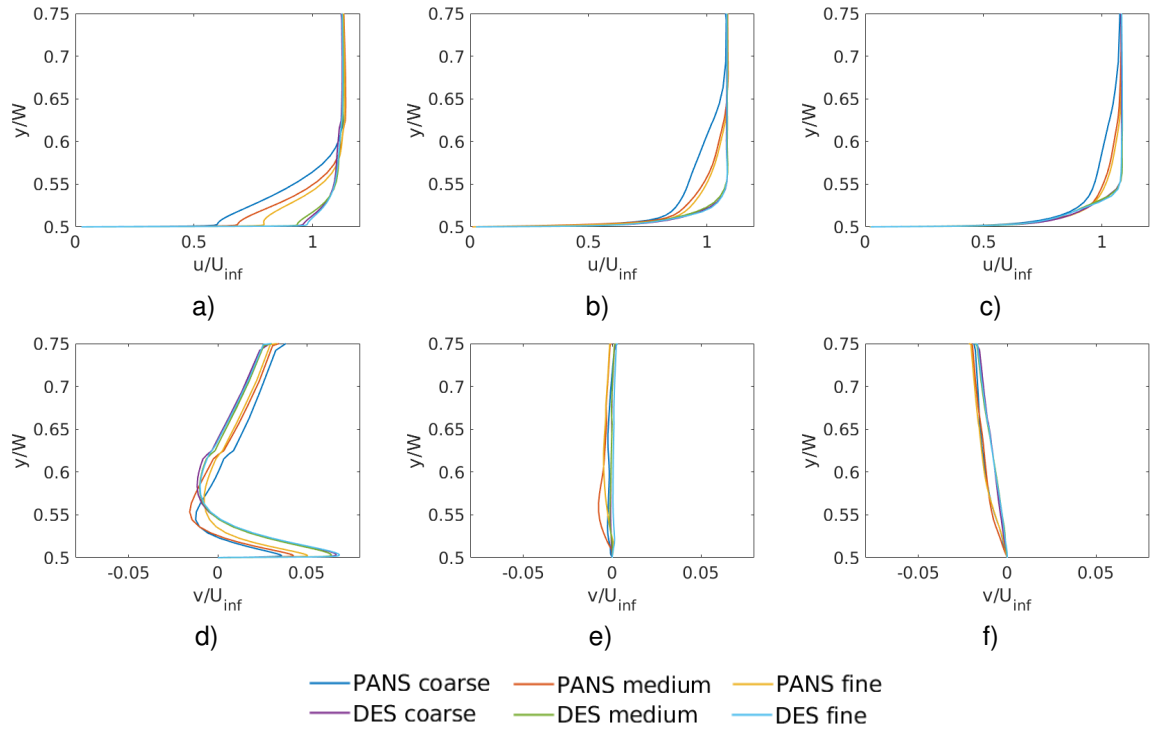

Figure 4.2: Profiles of the time-averaged velocity in the stream-wise and span direction at $x^* = 0.05$, a) and d), $x^* = 0.75$, b) and e), and $x^* = 2$, on the $z^* = 0$ plane.

maintaining similar profiles. As for which of the models present more correct results is undetermined as no experimental data of this section are available.

When it comes to the Reynolds stresses, we can also see more similarity between profiles of the DES results using the three meshes than for PANS. The similarity between profiles is higher for the $\overline{u'u'}$ than $\overline{v'v'}$. For $\overline{v'v'}$ the profiles between methods have a fairly similar shape, however it's magnitudes are significantly far apart, differing of one order of magnitude for some meshes. Although not as big, this difference of Reynolds stresses magnitude between the PANS and DES results is also visible in the $\overline{u'u'}$ profiles. This difference of magnitude is coherent with the fact that both methods have a very different way of treating the flow near the truck's surface. While the DES uses its RANS base model to treat the flow near surfaces, the PANS method treats the flow with a close to DNS approach, which means that DES models all the flow near the surface truck, while PANS resolves it, leading to PANS results having much higher values of Reynolds stresses there, than the DES ones. However, it is possible to see that the PANS with coarse mesh fluctuation results present a strange behaviour when compared to the other mesh results, as it presents significantly larger magnitudes, specially for the span-wise fluctuations.

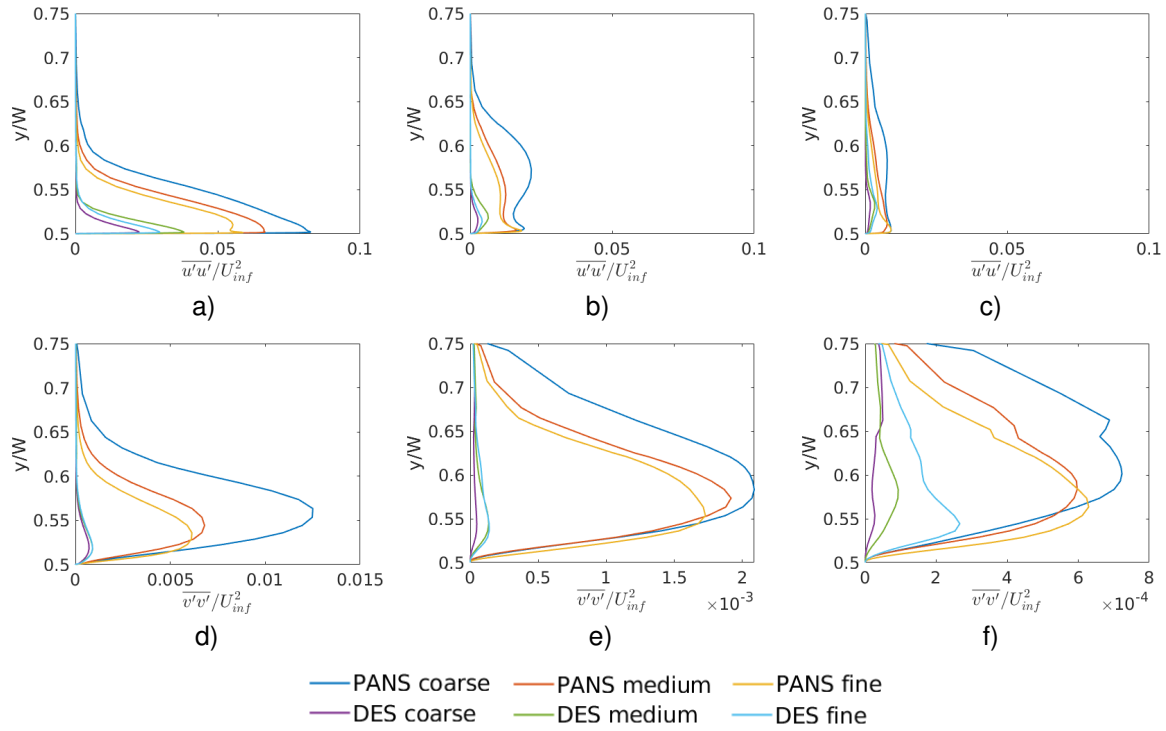

Figure 4.3: Profiles of $\frac{\overline{u'u'}}{U_{inf}^2}$ and $\frac{\overline{v'v'}}{U_{inf}^2}$ at $x^* = 0.05$, a) and d), $x^* = 0.75$, b) and e), and $x^* = 2$, on the $z^* = 0$ plane.

4.1.4.B Wake

In this section, the velocity and Reynolds stress profiles, taken on the plane $z = 0$ along the wake, are analyzed for three levels of grid refinement, and are compared with the experimental results obtained through PIV in an equivalent setting as the numerical simulations. The three probe lines with extension in the span-wise direction, are distributed along the wake, at $x/W = 2.63$, $x/W = 2.83$ and $x/W = 3.03$, in the $Z = 0$ plane. The value of mean velocity in the x and y direction and the mean Reynolds stresses $\overline{u'u'}$ and $\overline{v'v'}$ were recorded for 5 passages for each method and mesh, and are presented in figures 4.4 and 4.5, respectively.

Looking at figures 4.4, a), b), c), one can see that the U/U_{inf} profiles obtained from the numerical simulations always over-predicts the magnitude when compared to the PIV results. All results show a conical profile, symmetric or close to symmetric in relation to $y = 0$, with the streamwise velocity going from positive to negative and negative to positive along the y^* axis (from positive to negative), which is caused by the presence of a vortex with its axis along z^*, with it's core in the positive side of y^*, rotating in the clockwise direction, followed by a counterclockwise rotating one, with its core in the negative side of y^*, as it will be seen in section 4.1.7.

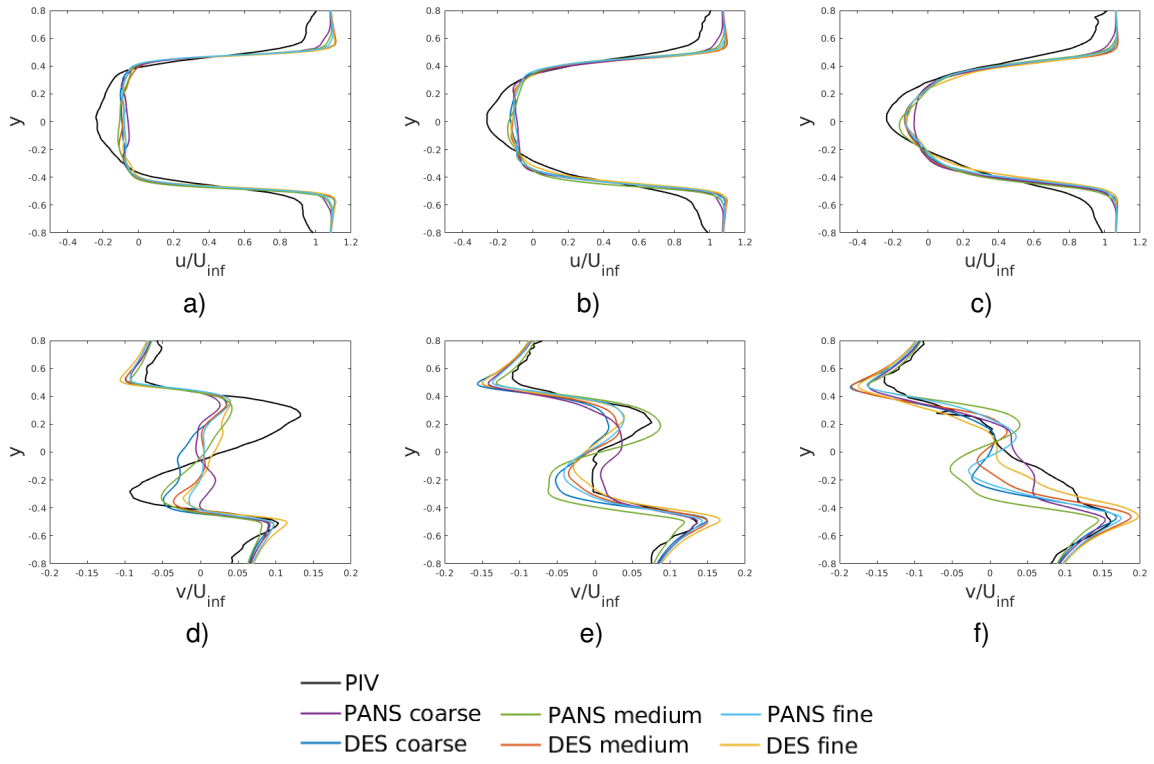

Figure 4.4: Profiles of the time-averaged velocity in the stream-wise and span direction at $x^* = 2.6252$, a) and d), $x^* = 2.8278$, b) and e), and $x^* = 3.0304$, on the $z^* = 0$ plane.

The profiles obtained with the simulations show a very good agreement between both methods across the three meshes, as they overlap along big portions of the profiles, showing again a good mesh convergence. One can again see that the coarse mesh results are further apart from the medium and fine mesh. The biggest differences between the CFD and experimental results are in the region closer to the interior of the profile, and for $x^* = 2.6252$ and $x^* = 2.8278$, (a) and b) respectively), the abrupt corner on the profile at around $y^* = \pm 0.5$. Again, the DES results present better agreement between meshes than the PANS results, and the PANS with the coarse mesh is the case which present most different profiles.

Still referring to the figures 4.4, a),b),c), along PIV (particle image velocimetry) and numerical simulation results, as we move in the streamwise direction, a) to c), the profiles adapt a sharper conical shape, and it is noticeable that the PIV profiles are always sharper and more elongated than the ones obtained in the simulations, meaning the PIV shows stronger velocities in counter streamwise direction and is varying more along y^*. This leads to believe that the simulations predict the same topology of vorticity in the $z^* = 0$ as PIV observation, although the vortices positions and intensity appear to differ between simulations and experiments. All numerical simulations are similarly distant from the PIV observation.

Now looking at Fig. 4.4, d),e),f), where the v/U_{inf} profiles in the span-wise direction, also for $x^* =$

2.6252, d), $x^* = 2.8278$, e), and $x^* = 3.0304$, f), on the $z^* = 0$ are presented. One can see that the simulation results give significantly different results, when compared to the PIV ones, specially when closer to the core region of the wake, $y^* = 0$. The profiles at $x^* = 2.6252$, Fig. 4.4.d) is where this differences are more accentuated. The profiles at $x^* = 2.8278$, e), present simulation results which are relatively closer to the PIV ones, presenting a similar shape, even overlapping in some regions close to $y = \pm 4$, however not being able to follow its magnitude in the majority of the profile. For $x^* = 3.0304$, f), the numerical simulation profiles present even more difficulty in "following" the PIV results for regions closer to $y^* = 0$.

Overall, both methods, across all meshes, don't capture the peaks of u and v velocity precisely, but all capture the trends present in the PIV observation.

The differences in the profiles between the simulations and the PIV results can be justified by differences between the simplified truck models used in the simulations, Fig. 3.1, and in the experiments, Fig. A.7, specially from the existence of two connecting rods between the cabin and trailer and of the round support located underneath the trailer, which have a major influence on the flow underneath the model that may strongly propagates to the wake. However, further investigation is required for better understanding.

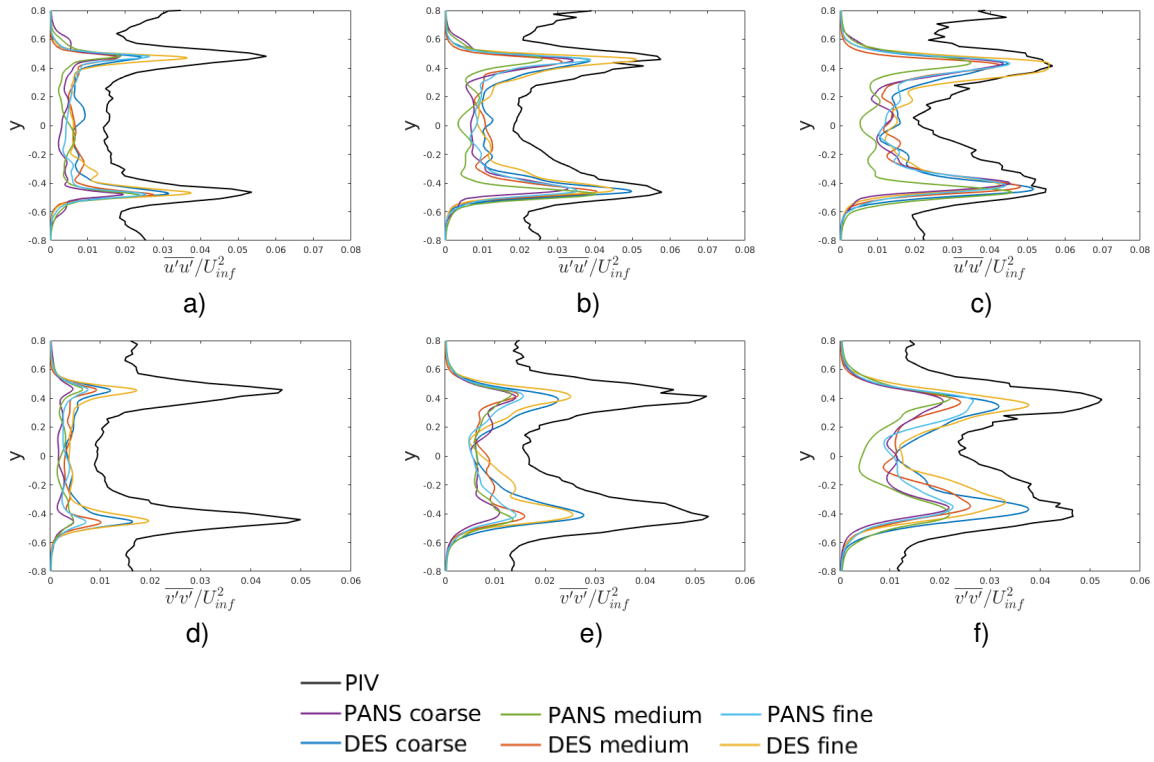

Figure 4.5: Profiles of the Averaged Reynolds stresses in the stream-wise and span direction at $x^* = 2.6252$, a) and d), $x^* = 2.8278$, b) and e), and $x^* = 3.0304$, on the $z^* = 0$ plane.

In Figure 4.5 the averaged Reynolds stresses in the streamwise, a) to c), and spanwise, d) to f), directions are presented. One can immediately notice the same pattern in all these profiles, two peaks at approximately $y^* = 0.4 - 0.5$ and a small conical depression with big oscillations in value between them, that gets sharper as we move along x^* in the wake, which is verified for all cases. Across all fluctuation profiles it is noticeable that for each mesh, the DES methods present higher Reynolds stresses values and closer to the PIV ones, meaning that the DES method is resolving more of the turbulence than PANS, inside the wake, as shown in Fig. 4.20. The PIV values are in all cases, always significantly larger than the ones obtained in the numerical simulations, and the PIV results present fluctuation values at the tips of the profiles with values significantly larger than zero, which doesn't happen with the numerical simulations.

4.1.5 Surface pressure Coefficient profiles

The pressure profiles of the bodies are directly connected with pressure drag, which is the dominant form of drag in bluff bodies. So, having a good surface pressure agreement of surface C_p between methods and meshes is of great importance. The surface pressure profiles of both cabin and trailer, measured along the planes $y = 0$ and $z = 0$ are presented in figure 4.6. Here C_p is defined by Eq. 4.1, in which p is the absolute pressure, p_∞ is the reference pressure in a cell in the upper right corner at the inlet, and the denominator is the dynamic pressure at the inlet.

$$C_p = \frac{p - p_\infty}{\frac{1}{2}\rho U_\infty^2} \tag{4.1}$$

In figure 4.6, a), the surface pressure coefficient profile at the plane $y = 0$ for the cabin is presented. One can see that the profiles resulting from the same methods almost overlap, with the exception of the PANS coarse mesh, where a noticeable discrepancy along x is visible. When looking at the region referring to the bottom part of the cabin (higher C_p lines along x in the plots) we can see that all results, but the ones from PANS with coarse mesh, overlap until $x/W \simeq -0.4$, from where PANS predicts a subtle increase of C_p while the DES results do not. When looking at the top region of the Cabin (lower value C_p lines) we can again see a different behaviour of the profile between the methods; while the DES results predicts an acceleration of the flow (C_p becomes more negative) along the spline at the top of the cabin and before reaching the top it starts smoothly decelerating (C_p becomes less negative), the PANS results show that the flow starts decelerating earlier, at about half the length of the spline, and there's a small "bump" in the pressure profile, right after the flow starts decelerating, which is a strange behaviour when looking at the cabin's geometry, since the bump happens when the corner ends and the flow reaches the top.

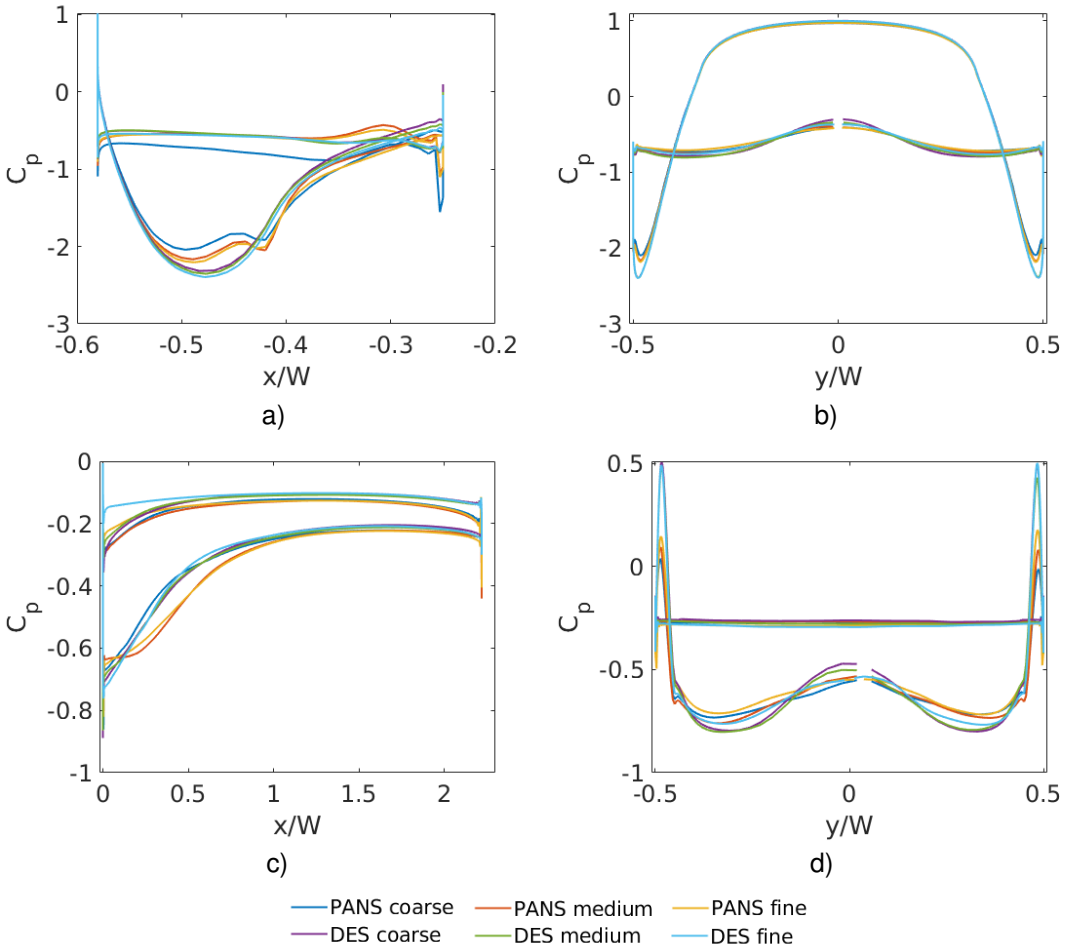

Figure 4.6: Measured surface pressure coefficient profiles with both PANS and DES methods, for the three meshes used, coarse, medium and fine. a) and c) are the pressure profiles at the plane $y = 0$ for the cabin and trailer, respectively, and b) and d) are at the plane $z = 0$ for the cabin and trailer respectively.

Once again, the PANS with coarse mesh results present a higher discrepancy from the medium and fine grid results, showing that DES handles better the coarser mesh. As for the cabin pressure profiles along the $z = 0$ plane, figure 4.1 b), they mostly overlap. Again, the DES results overlap more between meshes than the PANS ones.

In figure 4.1 c) the trailer pressure profile along the plane $y = 0$ is plotted, and we can see a good overlap between the results of different meshes using the same method, with exception for DES fine, which present higher value of C_p near $x/W = 0$, correspondent to the upper side of the trailer and the PANS coarse which show a better agreement with DES in the lower part of the trailer for lower values of x. As for the pressure profile along the plane $z = 0$, Fig. 4.1 d), there's a fairly good agreement between the results, with a more noticeable difference in the profiles for the front region of the trailer near $y/W = \pm 0.5$.

4.1.6 Surface pressure

In this section, the time averaged pressure coefficient on the cabin and trailer surfaces is presented and compared, between both methods PANS and DES, across the three same meshes. Such representation is found in Figure 4.7, where a big similarity of the results can be seen, presenting close C_p values on the surfaces, as well as a similar distribution.

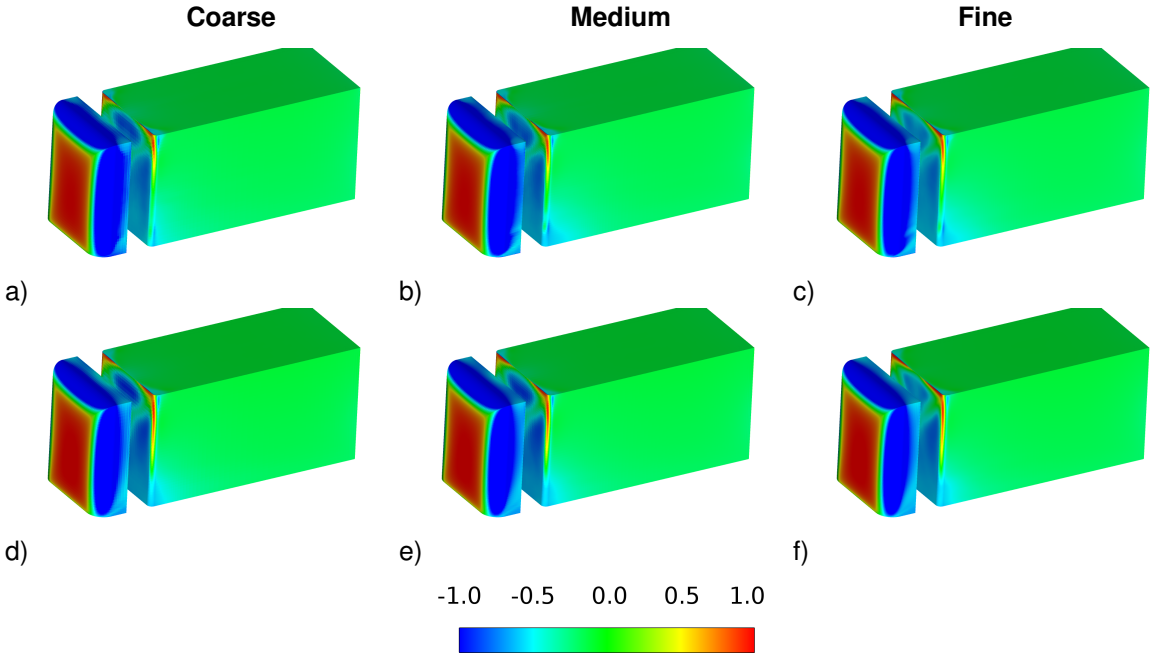

Figure 4.7: Pressure coefficient on the model's surfaces across the coarse, medium and fine mesh, using PANS, a), b), c), and DES, d), e), f).

In all results presented in Figure 4.7, the front surface of the cabin is mainly covered by C_p equal or close to one, which represents the existence of a stagnation region, caused by free-streaming air hitting it. The cabin's round edges accelerate the air flow, while keeping it attached, creating increasingly lower C_p values. More than half of the curved corner length is covered by $C_p \leq -1$ and the decrease in pressure is lower close to the cabin's horizontal edges. This large region of very low C_p over the cabin is responsible for its positive C_l values, as seen on Table 4.2. When looking at the cabin's C_p results of both models across the three meshes, we observe they are extremely similar. On the DES C_p results, Fig. 4.7.c),d),e), it is easy to identify an increase of pressure as the flow gets closer to the trailing edge of the cabin body in the side and top surfaces, due to the interaction with the fraction of flow rushing out of the recirculating flow in the gap between the cabin and trailer (see Appendix Fig. A.1.a)). Also, the flow passing underneath the cabin escapes to the sides, creating small swirling vortices and causing the flow to detach, along the lower corners of the cabin, visible on Fig. 4.21 and Appendix - Fig. A.2, which creates a curved stripe like region of low C_p on that region (along the lower corners of the cabin).

This two last characteristic behaviours are also identified in the PANS results, Fig. 4.7.a),b),c), however noticeably less pronounced, specially as the mesh coarsens. The vortices formed at the cabin's lower sharp corners travel further downstream, as seen on Fig. 4.21 and Appendix - Fig. A.2.c) f), and are responsible for the small low pressure regions at the front lower part of the trailer, where the flow is detached.

Looking at the front of the trailer, high-pressure regions are observed at the tips of the upper corner and at the upper part of the side corners, with the flow stagnating in regions of $C_p = 1$. These high-pressure regions occur due to the fraction of air that separates at the trailing edge of the cabin's sides and top, mainly coming from cabin top corners, and hits the trailer. In the DES results, this high pressure region extends noticeably longer along the trailer front side pillars, than in the PANS results. For DES results, this region is very similar between meshes. The same goes for PANS, although the length of the stagnation region on the front pillars is slightly shorter on the coarse mesh results than for medium and fine meshes, which have about the same length. Following these stagnation regions, part of the flow goes upwards and, due to the sharp top corner of the trailer, a small recirculation bubble is created on the top front corners of the roof of the trailer, which are visible as the lower pressure areas in Fig. 4.7. The recirculation bubble is visible in Fig. A.3.a) (Appendix). It is good to note that after the stagnation region at the side corners of the trailer, the low-pressure peaks are created due to acceleration of the flow by the round corners, as can be seen on Fig. A.3.b) (Appendix). The reason this low pressure peak only happens closer to the top corner is because the flow that separates at the trailing edge of the cabin's sides starts hitting the trailer further down the stream, as we can see by the high pressure region on the side corner of the trailer being slightly further downstream as the distance from the top increases.

The C_p distribution on the front surface of the trailer is very similar between meshes and models. It's distribution is dominated by the three main vortices present in the gap between the cabin and the trailer, two rotating in the z direction with opposite rotation, vortices TC and TD, and one rotating in the y direction, vortex B, and by the downwards rushing of flow below the vortex rotating in the y direction (all vortices are described and labeled in the upcoming section 4.1.7). There are three pockets of low pressure, darker blue, visible on the surface, where the top one corrsponds to the vortex B and the two symmetric ones right below, correspond to vortices TC and TD. As the flow rushes downwards on the area below the y vortex, this area also represents relatively low pressure. We can also see that between the vortices, the flow travels downwards with higher C_p, which is better seen on Fig. A.1.b) (Appendix). As we follow the trailer further downstream, all results show a decrease of C_p from the top to the bottom of it, indicating the existence of downforce.

All in all, the models give very close results of C_p behaviour on the truck's walls, with little change when coarsening the mesh, specially for the DES results since it models the flow close to the wall. The main difference between models and meshes lays on the C_p magnitudes, as we can see on the trailer's

front surface, and the trailing edges of the cabin. The fact that the DES surface C_p results are more consistent along the mesh coarsening and are similar to PANS results with medium and finer mesh, without having to resolve the whole boundary layer, making the DES wall approach more attractive.

4.1.7 Flow visualization

In this section a description of the flow is presented, together with the comparison between the visualizations of the flow features of the PANS and DES methods using a coarse, medium and fine mesh. This includes the comparison between the visualization of time-averaged velocity and streamlines obtained, and comparison of the critical points present and its locations. All results presented were considered after five passages averaging of the flow.

To complement the analysis of the flow visualizations, the figure 4.8 is introduced, representing the vortices' core and other critical points location on the planes $y = 0$ and $z = 0$, for all CFD and experimental results, together with the code names used to identify them along this report. To note that the experimental results only capture the wake on the plane $z = 0$. All coordinates marked with an asterisk are normalized by the width of the model, W.

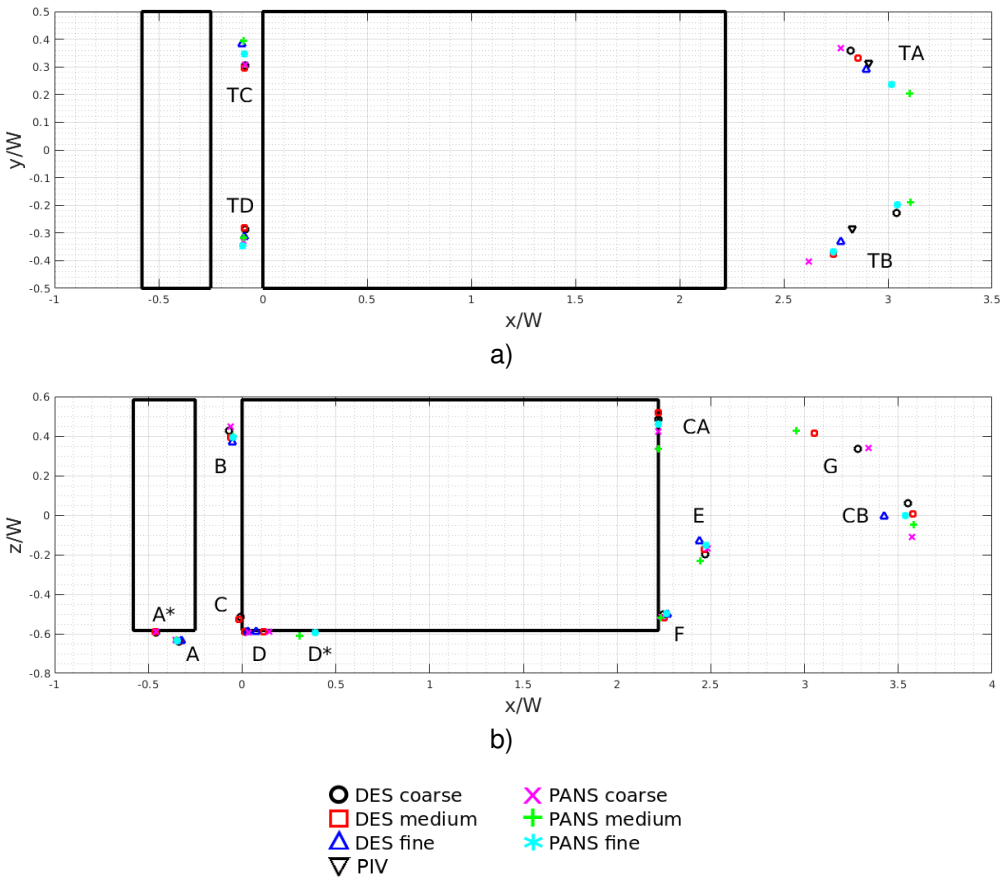

Figure 4.8: Critical points on the plane: a) $z = 0$, b) $y = 0$

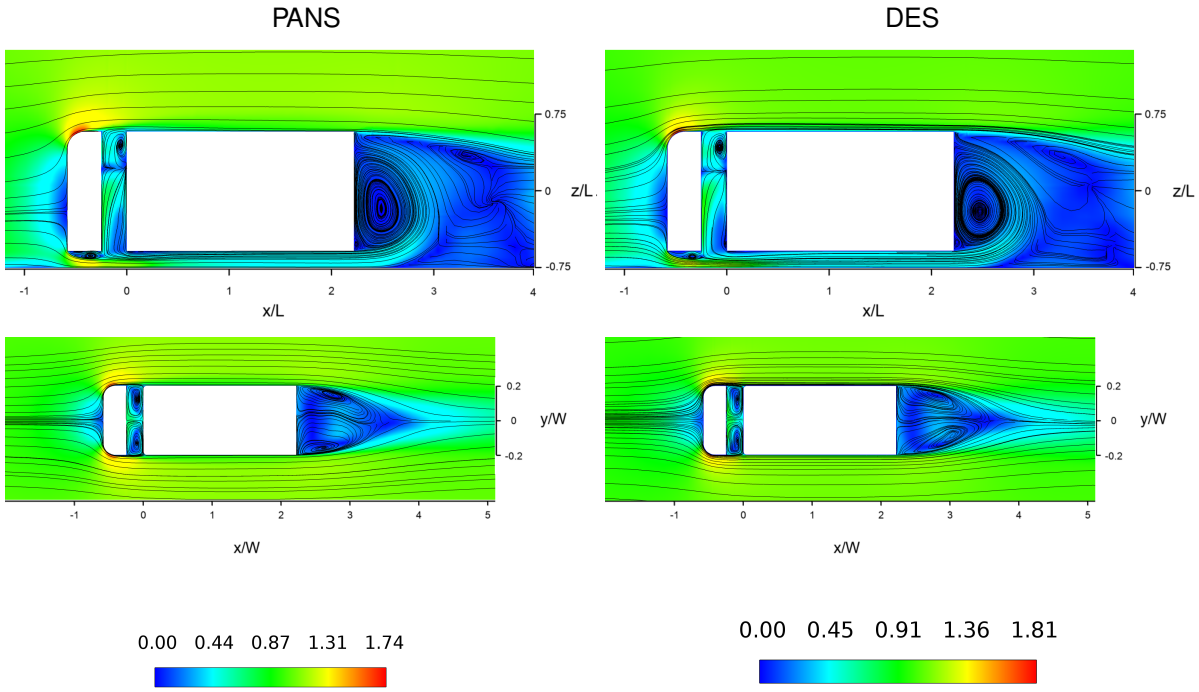

Figure 4.9: Contours of normalized time-averaged velocity and streamlines results using the coarse mesh with PANS and DES. First row: plane $y = 0$; Second row: plane $z = 0$.

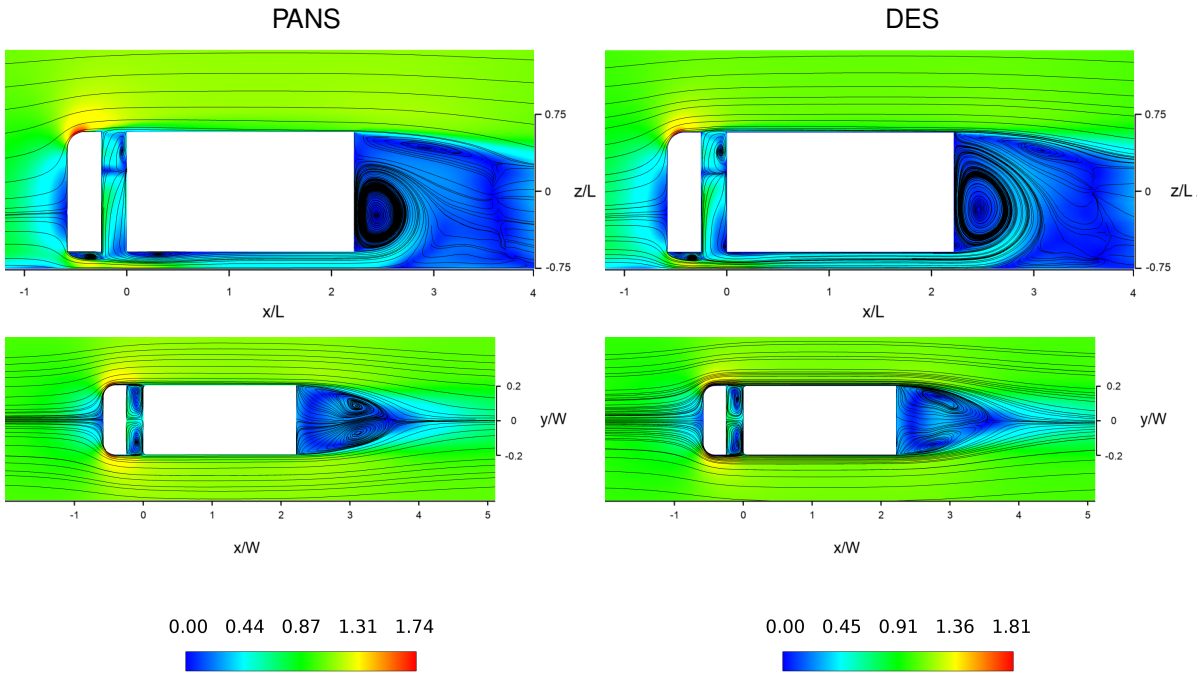

Figure 4.10: Contours of normalized time-averaged velocity and streamlines results using the medium mesh with PANS and DES. First row: plane $y = 0$; Second row: plane $z = 0$.

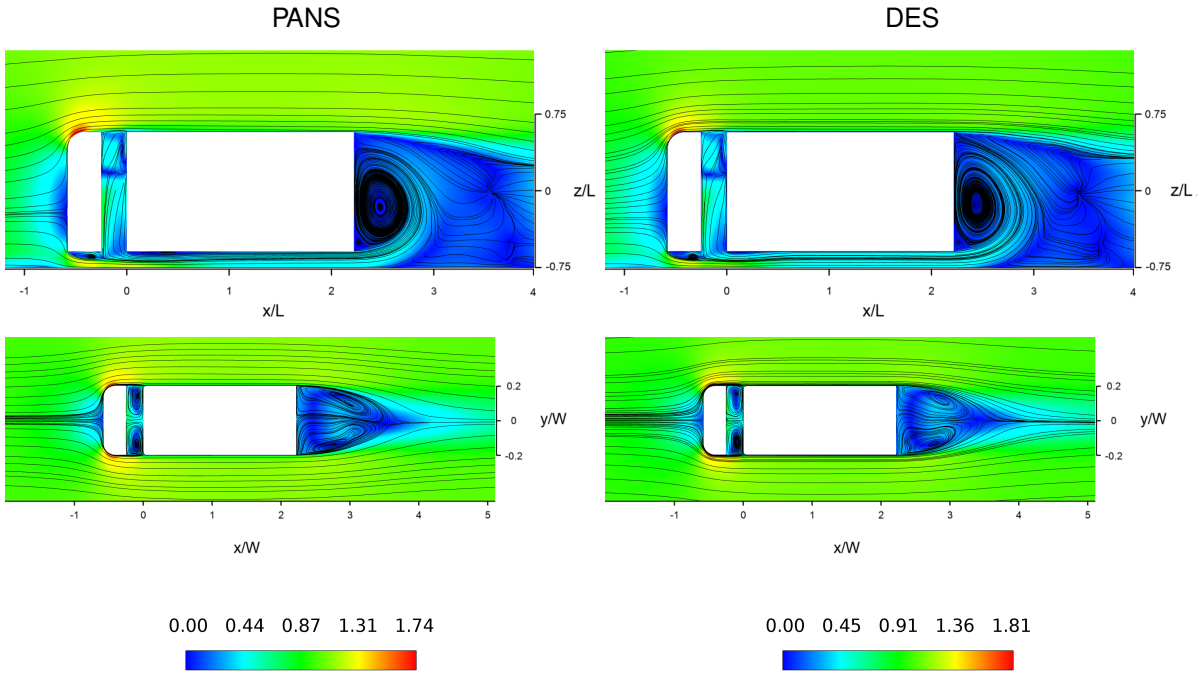

Figure 4.11: Contours of normalized time-averaged velocity and streamlines results using the fine mesh with PANS and DES. First row: plane $y = 0$; Second row: plane $z = 0$.

The following paragraphs will consist on the analysis and comparison of the flow structures and behaviour represented in figures 4.9 to 4.11, complemented by the vortex core location represented in figure 4.8. First, the analysis of the results on plane $y = 0$ will be carried out: The incoming unperturbed flow stagnates below the center of the cabin's front surface, due to the different radius of the top and lower corners and the vicinity to the ground. Part of the flow is directed upwards and is accelerated by the cabin curvature, always remaining fully attached, lowering the pressure in this region, which is responsible for the lift behaviour in the cabin, presented in section 4.1.2. Other part of the flow goes downwards and separates from the cabin when trying to follow the cabin's lower sharp angle, creating a recirculation bubble, A. This re-circulation bubble is very similar between methods using the same mesh, presenting a similar size, shape and core location as it can be seen in figure 4.8.b). Both methods, when using the coarse mesh, present an extra recirculation bubble in this location, much smaller in size when compared to vortex A, which is pointed out in figure 4.8.b) as vortex A*. This small vortex is only present with the use of the coarse and medium mesh with DES and coarse mesh with PANS, as it can be seen in figures 4.9 to 4.11, presenting the same core location. Comparing the vortex A between methods and meshes, we can see that for all of the combinations, method - mesh, the location of the core of vortex A on the plane $y = 0$ is almost coincident and the joint size of the vortices A and A* is very close to each other.

As the flow contours the cabin, part of it travels into the gap between the cabin and the trailer. Here

the flow is fairly similar between PANS and DES, along the three meshes, all presenting a bifurcation of the flow across the gap, at around $0.2375 > z^* > 0.028$, which is caused by the flow in that region being dominated by the mass flow coming from the sides of the cabin, with a clockwise rotating vortex above it, vortex B, and a downwards flow stream below, also dominated by the mass flow from the sides. The location of vortex B seems to be well predicted and coherent across PANS and DES using the same mesh, since its core location on the plane $y = 0$ is reasonably close, as presented in figure 4.8.b). It's shape is also reasonably close between methods and meshes, just with slight differences. The vortex B from the results using DES and PANS coarse and medium mesh, is rounder and more concentrated than in the refined mesh results. This can be one of the contributions for the fact that the C_d of the trailer in this cases are more negative.

Looking at the front lower region of the trailer there are some differences on the flow behaviour. The coarse and medium DES results present a small recirculation bubble on the extreme lower part of the front surface of the trailer, identified as C on Fig. 4.8.b), which is not present on the other results. All PANS results present a significantly bigger recirculation bubble underneath the trailer, identified as D on Fig. 4.8.b), when compared to the DES results.

Moving on to the wake of the trailer, the major contributors of the truck's drag are found, the trailer wake vortices. Continuing looking at the results presented in figures 4.9 to 4.11, we can see that the flow topology is similar for all methods and meshes. There are two main vortices on the wake of the trailer rotating in opposite directions, vortex E and G. The flow traveling on top of the trailer stays always attached and it contours and encapsulates the re-circulation zone on the wake of the trailer in a slightly downward direction, without piercing it. The flow coming from underneath the trailer is mostly fed into the main lower vortex, vortex E, and there is a reversed ground boundary layer flow for $2.8 < x^* < 3.7$. Trapped by the main lower vortex and the feeding flow from the under-body, there is a very small secondary lower vortex, F, which is created when the flow travelling downward along the trailer's base separates, after encountering an adverse pressure gradient once it gets past vortex E. We can also see that a saddle point and a rear stagnation point are formed where the upper vortex, G, and the main lower vortex, E, meet, in the rear of the trailer, represented in Fig. 4.8.b) as CA. Only the results from the fine mesh don't present the vortex G, having instead a boomerang shape flow. A possible reason for this is the longer averaging time usually necessary for finer meshes. Also, common to all results is the presence of a node source point, identified as CB, on figure 4.8.b) - which means that the wake closure mechanism in this region is mainly caused by the flow coming from the sides of the trailer. It also means that the flow downstream of this area and some of the reversed ground boundary layer flow are also originated by the flow from the sides of the trailer. Near the main upper vortex, G, there is a free saddle point, that divides the flow in four parts: flow passing between the two main vortices, flow on the main upper vortex, G, flow passing above the main upper vortex and flow coming from the source point.

Looking at figure 4.8.b), we can see the E and F vortices' core location, in the $y = 0$ plane, is very similar between PANS and DES across the different meshes. However, we can see a difference in the vortex E height as we can notice that the rear stagnation point, CA in figure 4.8, that enclosures this vortex is always higher for DES simulations than for the same mesh in PANS results. This can be one of the reasons for the trailer C_d values in DES results being higher than the results from PANS, when using the same mesh. From Fig. 4.8.b), one can easily see that this stagnation point is particularly lower for the PANS with medium mesh, making its vortex E the smallest between the results. Also, the DES with fine mesh results do not present the stagnation point CA, meaning that the vortex E takes over the entire trailer base, which can also be one of the reasons for its trailer C_d being the highest between the results.

The vortex G location is fairly close between methods using the same mesh but noticeably far away between different meshes. More noticeably is the absence of the vortex G on the fine mesh results, which instead present a boomerang shape flow. Most likely, this is the main reason why the fine meshes present a higher C_d, since it is the main difference between results on the wake topology. In figure 4.8.b), when comparing the node source point position between results, we can see they lay around the same region but relatively far from overlaying each other.

Next, the analysis of the results on the plane $z = 0$, referring to figures 4.9 to 4.11, will be carried out. Looking at the results, one can see that both methods give a fairly similar flow description on the plane $z = 0$. In all results the incoming unperturbed flow stagnates in the center-line ($y = 0$) of the plane $z = 0$, which is coherent with the fact that the model is symmetric in relation to the plane $y = 0$. The flow accelerates while contouring the A-pillars of the cabin, always remaining fully attached, and separates at the trailing edge of the tractor body, forming two symmetric counter-rotating vortices trapped inside the gap between the tractor and the trailer, denominated TC and TD, which dominate this region. The flow visualization on the plane $y = 0$ together with the one at $z = 0$, describe an half toroidal vortex in the gap. All the results show a fairly symmetric flow in the gap, with the PANS with medium mesh and the DES with fine mesh results being the less symmetric in core locations, as it can be seen in 4.8.a). As the flow reaches the trailer side walls, it remains attached to them along the entire length. As PIV experiments carried out were focused on the plane $z = 0$ at the wake, a close-up comparison of this is presented on Fig. 4.12, where the time-averaged streamwise component of velocity is presented, together with the streamlines. The wake of the trailer is dominated by two large vortices, TA and TB, which are bounded by the mass flow from the side surfaces of the trailer, and unite into a saddle point. Due to the symmetric geometry of the model and a zero yaw angle setting, it would be expected to have a fully symmetric flow around the truck. However, the results don't show this. In the wake of the trailer all the results present a certain degree of asymmetry. However, the PIV results are fairly close to symmetric wake, with its vortices' cores occupying the locations $(x^*, y^*) = (2.907, 0.313)$ and $(x^*, y^*) = (2.828, -0.283)$. The results from PANS with medium mesh present the most symmetric

vortices' cores, located at $(x^*, y^*) = (3.103, 0.205)$ and $(x^*, y^*) = (3.108, -0.188)$, however they are positioned considerably further downstream than the PIV results, just like the PANS with the fine mesh. The DES with fine mesh results comes in second when it comes to being close to symmetric, and is followed by the DES with medium mesh. The wake vortices are located at $(x^*, y^*) = (2.858, 0.333)$ and $(x^*, y^*) = (2.737, -0.376)$ for the DES with medium mesh, and $(x^*, y^*) = (2.895, 0.291)$ and $(x^*, y^*) = (2.773, -0.333)$ for the DES with fine mesh, making the DES with fine mesh case the one which has vortex core location closer to the PIV, followed by the DES with medium mesh results. The remaining results present a higher degree of asymmetry, as better seen in figure 4.8.a). To achieve a symmetric solution in respect to the plane $z = 0$, a higher averaging time is required for all simulations.

It is also interesting to analyze the wake flow visualizations in Fig. 4.12 with the U velocity profiles presented on Fig. 4.4, as a better understanding of those profiles and a better comparison between the experimental and the CFD results can be made. For example, if we look at the wake images we see on the PIV results show a bigger, darker blue region along the center of the wake, when compared to all CFD simulation results, which is coherent with the u velocity profile results presenting more negative values closer to the center than the numerical simulations results. Also, the PIV results present a bigger difference of blue tones along y, while the simulations have a very soft blue with little variations, which is also coherent with PIV u profiles presenting a more conical shape than the CFD ones, which have more of a square shape.

Overall, all cases, experimental and CFD, capture the same main structures, although with different sizes and positions, as the vortices cores differ noticeably between methods, meshes and experiments. Although the DES results present vortices TA and TB core positions closer to the PIV results than PANS, it is important to keep in mind that the experiments model is slightly different from the model used in the numerical simulations, as it has two connecting rods between the cabin and trailer and a round support located underneath the trailer, which impacts on the flow underneath the model and affects the wake dynamics. A picture of the experimental model is show in the appendix, Fig. A.7.

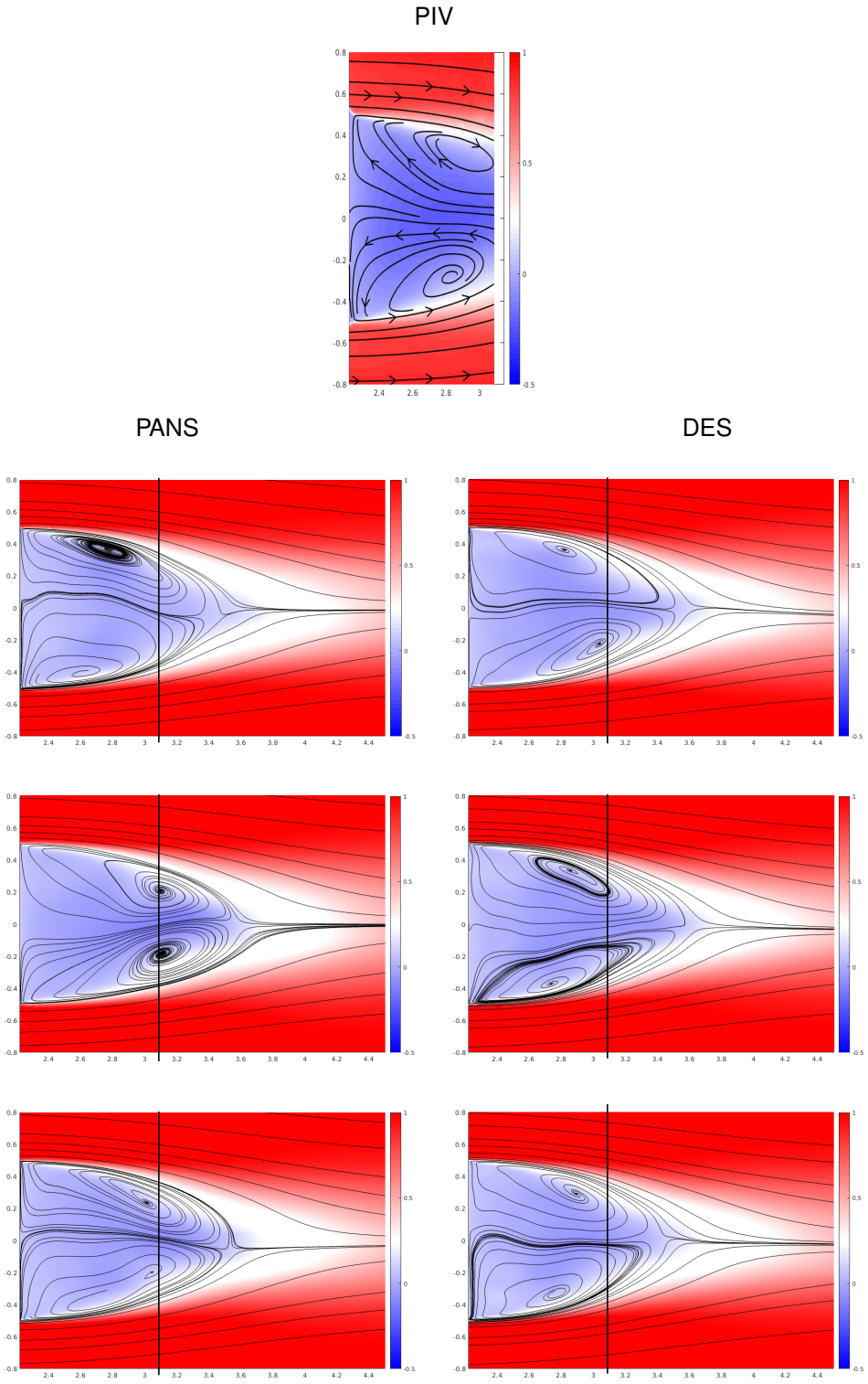

Figure 4.12: Contours of normalized time-averaged velocity and streamlines of the PIV results and of the results with coarse (first row), medium (second row) and fine (third row) meshes using PANS and DES, on the $z = 0$ plane. The black line in the simulation results show the limit of the PIV frame.

4.1.7.A Averaged Vorticity and Reynolds stresses

In this section, the time averaged normalized vorticity, $\frac{w_i}{U_{inf}/W}$, as well as the normalized fluctuating Reynolds stress components, $\frac{\overline{u'u'}}{U_{inf}^2}$, $\frac{\overline{v'v'}}{U_{inf}^2}$ and $\frac{\overline{w'w'}}{U_{inf}^2}$, are presented in the planes $y = 0$ and $z = 0$, for both methods, PANS and DES, along the three same meshes, coarse, medium and fine. These are also compared with the PIV results of the $z = 0$ plane, taken at a portion of the wake.

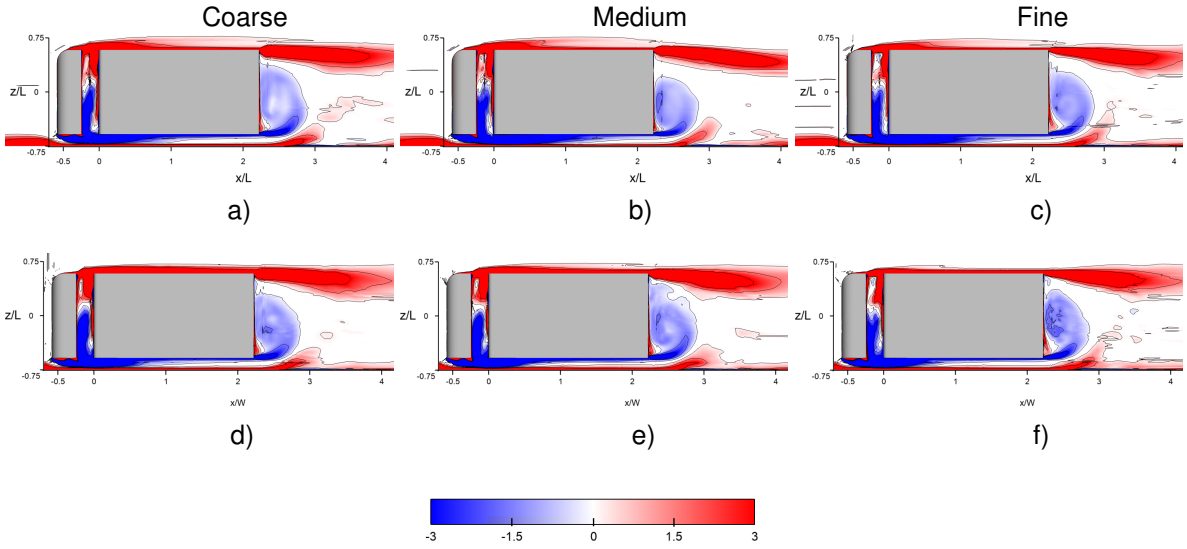

Figure 4.13: Contours of normalized time-averaged y-vorticity on the $y = 0$ plane using the coarse, medium and fine mesh with PANS, a), b), c), and DES, d), e), f).

Looking at the 2D representations of the y-vorticity and z-vorticity on the $y = 0$ and $z = 0$ planes, on figures 4.13 and 4.14, respectively, they all present the same topology. When looking to the side view, plane $y = 0$, as the flow first reaches the cabin, it gains positive vorticity in the y direction above the front stagnation point and negative below. As it reaches the gap, the flow rotating in the negative direction dominates most of the gap space, as only part of the top area of the gap is filled with flow rotating in the positive direction. This is due to the lower pressure area on top of the cabin, created by the flow accelerated by the rounded top corner, sucking in the flow from underneath the cabin, which already has a negative rotation by itself. In the wake of the trailer, we can identify the upper and lower shear layer vortices, E and G, with positive and negative rotation, respectively, and the secondary vortex, F, with positive rotation, generated on the rear surface of the trailer by the flow of the main lower vortex, E. Below the main lower vortex it's possible to identify the positive y-vorticity generated by the stationary ground and right after, right at the ground, a section of negative rotation, caused by the reversed ground boundary layer flow described in section 4.1.7. For a closer view, see Fig. A.4 to A.6. From the top view, $z = 0$, we can see an almost symmetric vorticity, with the right side of the truck being overwhelmed by negative z-vorticity values and the left part by positive. All the four major vortices are visible in the $z = 0$

plane, TA, TB, TC, TD, in all CFD and PIV results.

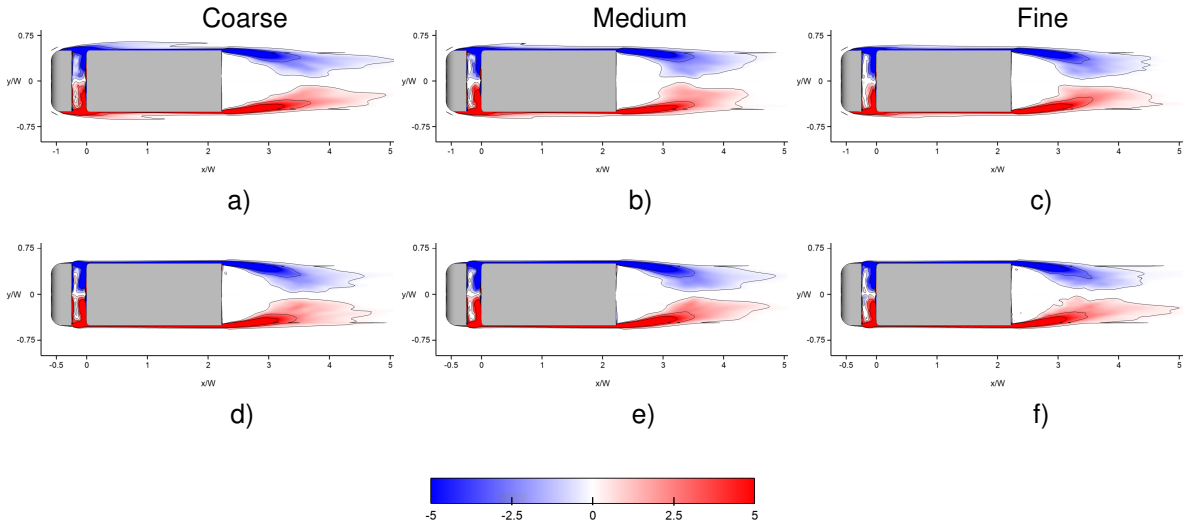

Figure 4.14: Contours of normalized time-averaged z-vorticity on the $z = 0$ plane, using the coarse, medium and fine mesh with PANS, a), b), c), and DES, d), e), f).

The results are very similar when it comes to the vorticity along the gap and underneath the truck. However, by looking at Fig. 4.13, one can notice it is on the flow above the truck that the vorticity behaviour differs the most between methods, along the three meshes. In PANS results most of the vorticity is induced by the cabin's round angle, however in DES it is mostly created by the flow coming out of the gap. Also, in PANS results the vorticity lowers along the trailer top, while in DES it almost remains unchanged, representing an almost constant layer thickness. We can see a similar behaviour when looking to the top view results of z-vorticity, Fig. 4.14, where in PANS results there's a big growth in vorticity value after the end of the cabin side round corners, while in DES results this increase only happens instantly after the flow leaves the cabin's surface and reaches the gap. Also, the vorticity substantially decreases along the trailer sides for the PANS results, while for DES, it barely changes along the trailer sides.

As PIV experiments were conducted for the $z = 0$ plane on the wake, a closer representation of the experiment and CFD results in that region is presented on Fig. 4.15. As pointed out before, both models across all meshes, predict the two main regions of high vorticity in a very similar way. The experimental results also capture the two main regions of vorticity, however with significantly weaker intensity than the CFD results. Both experimental and CFD results identify the presence of two small regions of counter rotating vorticity immediatly at the trailer base, with the PANS presenting this region more similar to the PIV results and more symmetric than DES. It is also visible that the CFD results present peaks of vorticity in the center of the wake region, while the PIV results present no vorticity there.

When comparing the streamline top view representations in section 4.1.7 with the top view results of

z-vorticity, the first thing that strikes out is how symmetric the z-vorticity results are, when comparing to the asymmetric behaviour presented by the averaged flow streamlines.

It is important to understand that the figures 4.13 and 4.14 represent levels that were selected in order to better see the lower shear layer vortex structure. The results for every case do have higher values of vorticity than the ones presented in the figures.

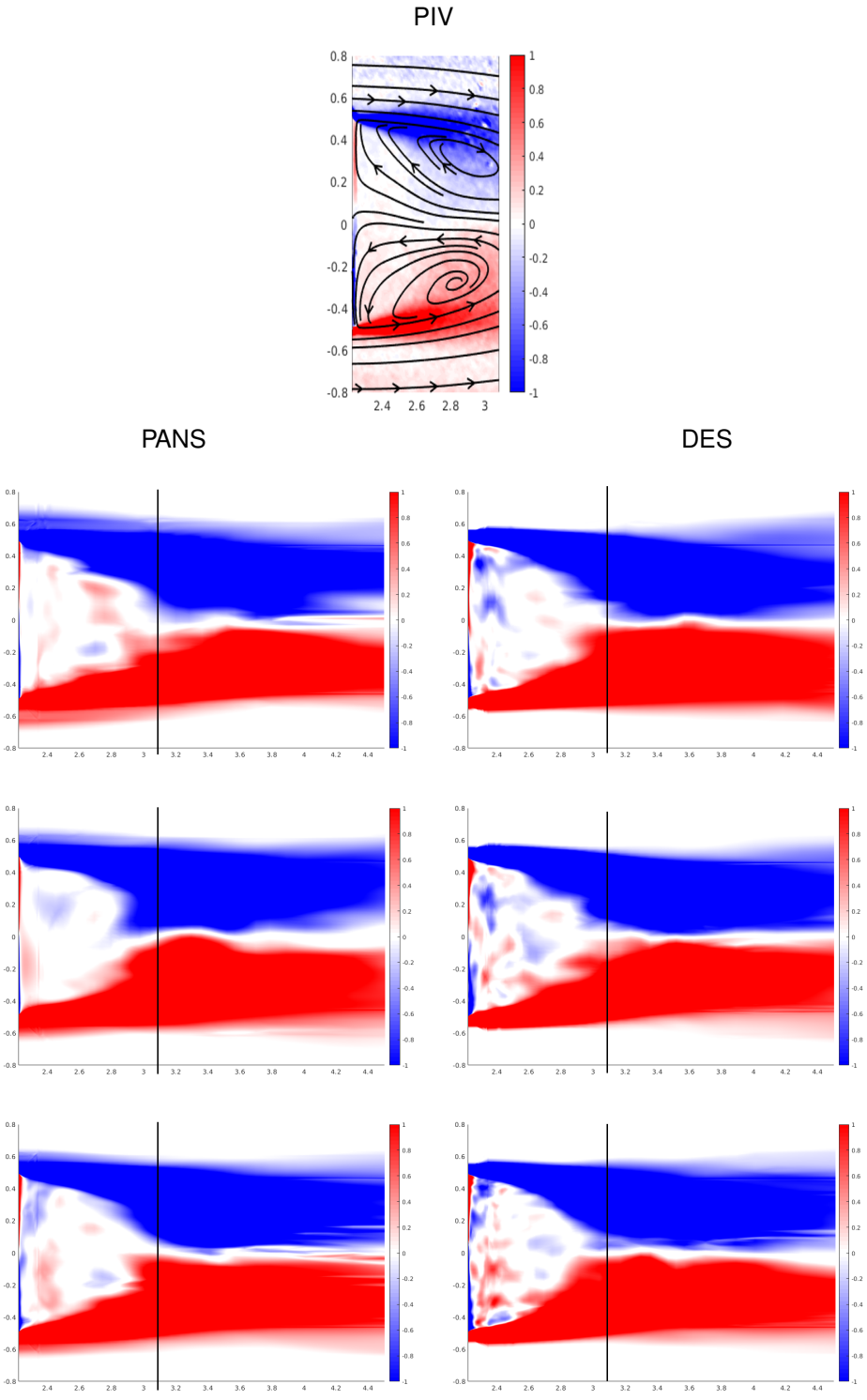

Figure 4.15: Contours of normalized time-averaged z-vorticity on the $z = 0$ plane, of the PIV results and of the results with coarse (first row), medium (second row) and fine (third row) meshes. The vertical black lines on the CFD results represent the extreme right position of the PIV window.

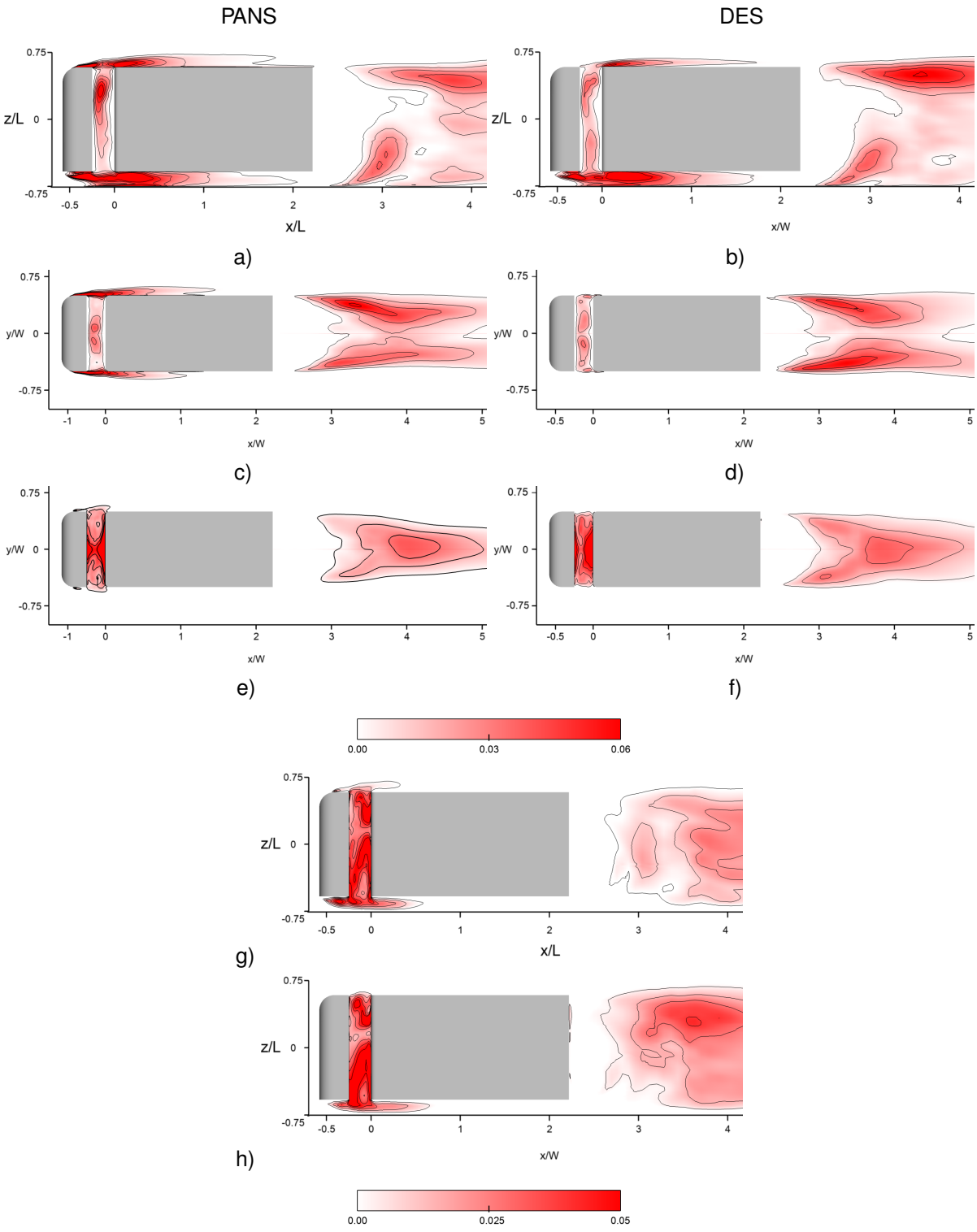

Figure 4.16: Contours and isolines of normalized time-averaged Reynolds stresses using the coarse mesh with PANS and DES. a), b) and c), d): $\frac{\overline{u'u'}}{U_{inf}^2}$ on the $y = 0$ and $z = 0$ planes respectively, e) and f) is $\frac{\overline{v'v'}}{U_{inf}^2}$ on the $z = 0$ plane, and g) and h) is $\frac{\overline{w'w'}}{U_{inf}^2}$ on the $y = 0$, of PANS and DES respectively..

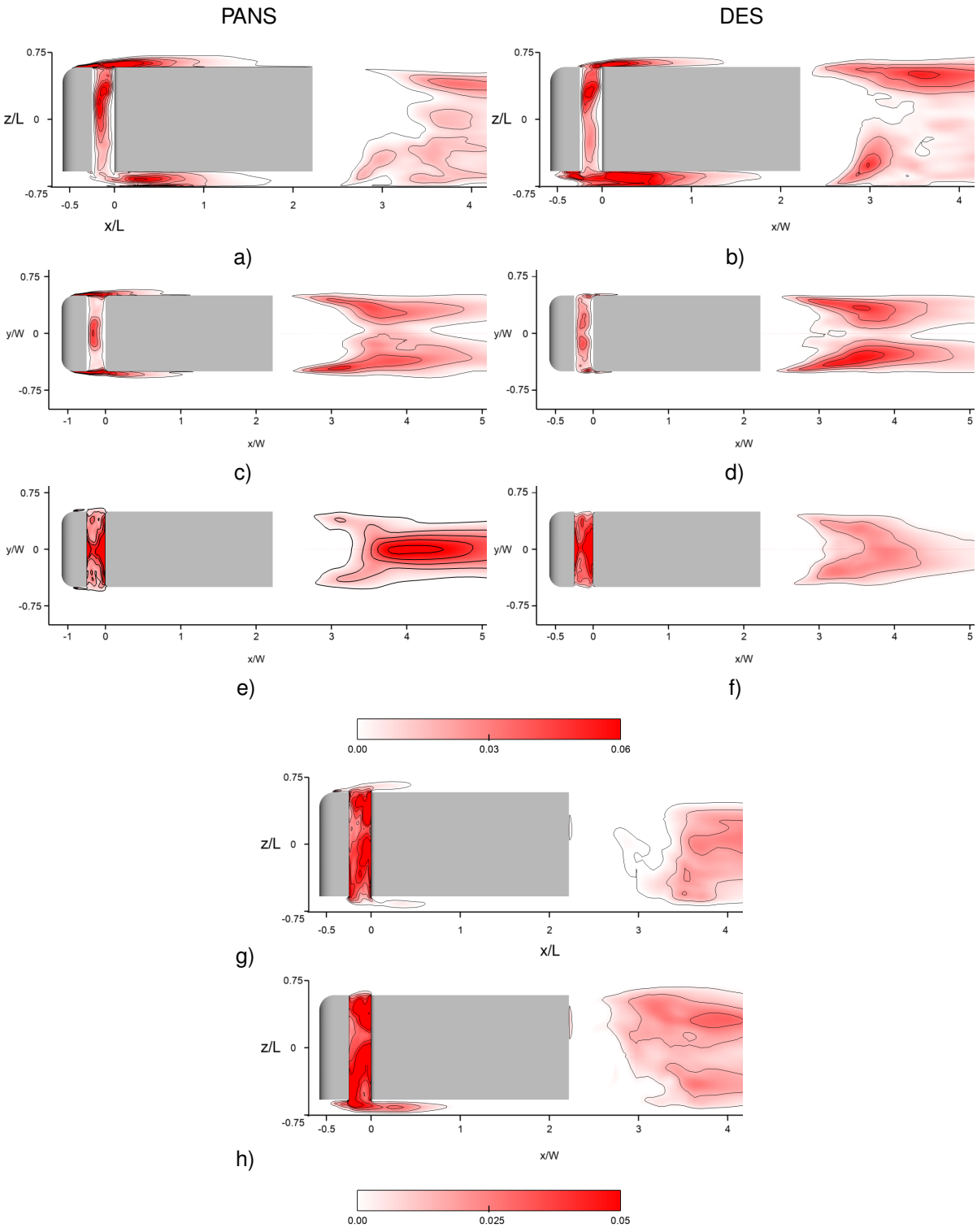

Figure 4.17: Contours and isolines of normalized time-averaged Reynolds stresses using the medium mesh with PANS and DES. a), b) and c), d): $\frac{\overline{u'u'}}{U_{inf}^2}$ on the $y = 0$ and $z = 0$ planes respectively, e) and f) is $\frac{\overline{v'v'}}{U_{inf}^2}$ on the $z = 0$ plane, and g) and h) is $\frac{\overline{w'w'}}{U_{inf}^2}$ on the $y = 0$, of PANS and DES respectively..

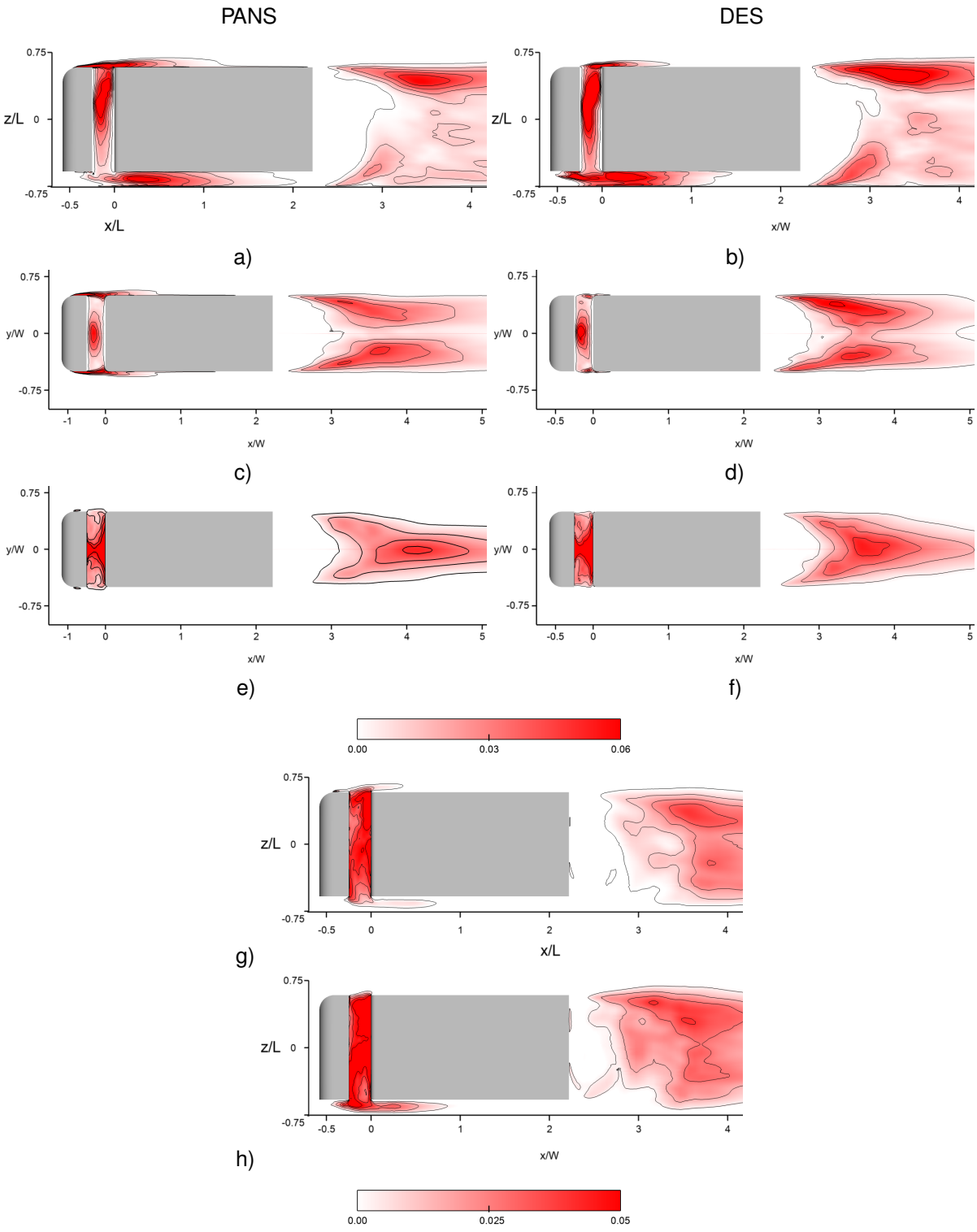

Figure 4.18: Contours and isolines of normalized time-averaged Reynolds stresses using the fine mesh with PANS and DES. a), b) and c), d): $\frac{\overline{u'u'}}{U_{inf}^2}$ on the $y = 0$ and $z = 0$ planes respectively, e) and f) is $\frac{\overline{v'v'}}{U_{inf}^2}$ on the $z = 0$ plane, and g) and h) is $\frac{\overline{w'w'}}{U_{inf}^2}$ on the $y = 0$, of PANS and DES respectively.

In figures 4.16 to 4.18, the 2D representations of Reynolds stresses, $\frac{\overline{u'u'}}{U_{inf}^2}$, $\frac{\overline{v'v'}}{U_{inf}^2}$, $\frac{\overline{w'w'}}{U_{inf}^2}$, on the $y = 0$ and $z = 0$ planes, are presented. In these figures, one can see that in all cases, $\frac{\overline{u'u'}}{U_{inf}^2}$ is the strongest fluctuation, however its highest values are located in different regions, depending on the mesh and method. When referring to the plane $y = 0$, the PANS with medium and fine meshes results present the highest values of fluctuation on the region above the cabin, above and below the first quarter of the trailer and on the gap between the cabin and trailer, with the finer mesh presenting the higher values more spread than the medium - since when the mesh is finer, more stresses are resolved, leading to higher values of fluctuation. Although the coarse mesh presents the regions of highest values of Reynolds stresses referred for the medium and fine mesh, it differs majorly by also presenting a large region of very strong fluctuations under the cabin. Just like the PANS with coarse mesh results, all DES results have the highest values of $\frac{\overline{u'u'}}{U_{inf}^2}$ in this large region below the cabin, as well as above and under the trailer. However, unlike the PANS results, none of the DES results present the strong fluctuations region above the cabin. Also, only the medium and fine mesh present strong fluctuation on the gap region (even stronger than the PANS results) and for the fine mesh, the region of the upper shear layer on wake of the trailer is also a region of highest values of fluctuation. Along all cases it is possible to identify strong fluctuations on the region of the upper shear layer and on the shear layer caused by the stationary ground, both visible on the wake of the trailer, and its values start decreasing from around $x^* = 3$, downstream. Still looking at the results on the $y = 0$ plane, when looking at the wake, for the same mesh, the DES results always present higher values of $\frac{\overline{u'u'}}{U_{inf}^2}$ and also more disperse.

When looking at the results contoured on the $z = 0$ plane, figures 4.16.c),d) to 4.18.c),d), one can see that all PANS results present the highest values of $\frac{\overline{u'u'}}{U_{inf}^2}$ on the side shear layers of the cabin, which extends until the front of the trailer, along with the regions described for the $y = 0$ plane. However, the DES results present no fluctuations in this regions, and have no regions of $\frac{\overline{u'u'}}{U_{inf}^2}$ as high as on the $y = 0$ plane. For the DES results, the $z = 0$ plane has the strongest $\frac{\overline{u'u'}}{U_{inf}^2}$ concentrations at the trailer's side shear layers, which are also present on the PANS results, however slightly weaker. Along all cases it is also possible to identify strong fluctuations on the gap region, where the fine meshes present a peak of $\frac{\overline{u'u'}}{U_{inf}^2}$ with both models. It is also interesting to notice that when looking at the truck region, PANS and DES results, present an almost symmetric $\frac{\overline{u'u'}}{U_{inf}^2}$ distribution.

In figure 4.19, the wake $\frac{\overline{u'u'}}{U_{inf}^2}$ results on the plane $z = 0$ are presented for both models across the three meshes and for the PIV results. From this, one can see that the experimental results present considerably higher $\frac{\overline{u'u'}}{U_{inf}^2}$ fluctuation levels, and in larger regions, as it starts being visible right after the trailer's end, while CFD results show no fluctuation close to the trailer base. Figures 4.16.e), f) to 4.18.e), f) show the strongest values of $\frac{\overline{v'v'}}{U_{inf}^2}$ on the gap between the cabin and trailer, specially in its center region. All cases also present regions of high $\frac{\overline{v'v'}}{U_{inf}^2}$ values at the wake of the trailer, at around $x^* = 3$ onward, with the PANS with the medium and fine mesh and DES with fine mesh presenting peaks downstream

of the time-averaged recirculation region (presented in figures 4.9 to 4.11). The $\frac{\overline{v'v'}}{U_{inf}^2}$ results are fairly similar between methods for the same mesh, with the exception of the medium mesh, where the PANS results present a wider and stronger region of fluctuations at the wake.

Finally, figures 4.16.g), h) to 4.18.g), h), show the contour with isolines of $\frac{\overline{w'w'}}{U_{inf}^2}$, on the $y = 0$ plane. It is possible to see that all cases show a similar distribution of $\frac{\overline{w'w'}}{U_{inf}^2}$, where the gap between the cabin and trailer is the region with highest values of oscillations and with a region of weaker oscillations down the wake. One evident difference between the results is the strong region of oscillations present at the region below the cabin for all DES results and PANS with coarse mesh, which is not present in the PANS with medium and fine mesh. It is interesting to notice on the DES results that as the mesh is refined, the bigger is the region of the strongest oscillations, which again makes sense, since as the mesh is refined, more stresses are resolved, leading to higher values of fluctuation. One can also see that the DES results present a stronger and wider region of fluctuations on the wake than the PANS results, with the PANS with medium mesh only presenting a region with oscillation further on the wake when compared to the other results. Also, there are peaks of oscillation on the region of the free saddle point, CC, resulting on the interaction between the flow coming from the main upper vortex and the source point.

An interesting tendency of all components of Reynolds stresses is that DES presents higher and larger regions of fluctuations on the wake than the PANS results, and that PANS presents higher and larger regions of fluctuations close to the truck surfaces than the DES results, if the regions underneath the truck are not considered.

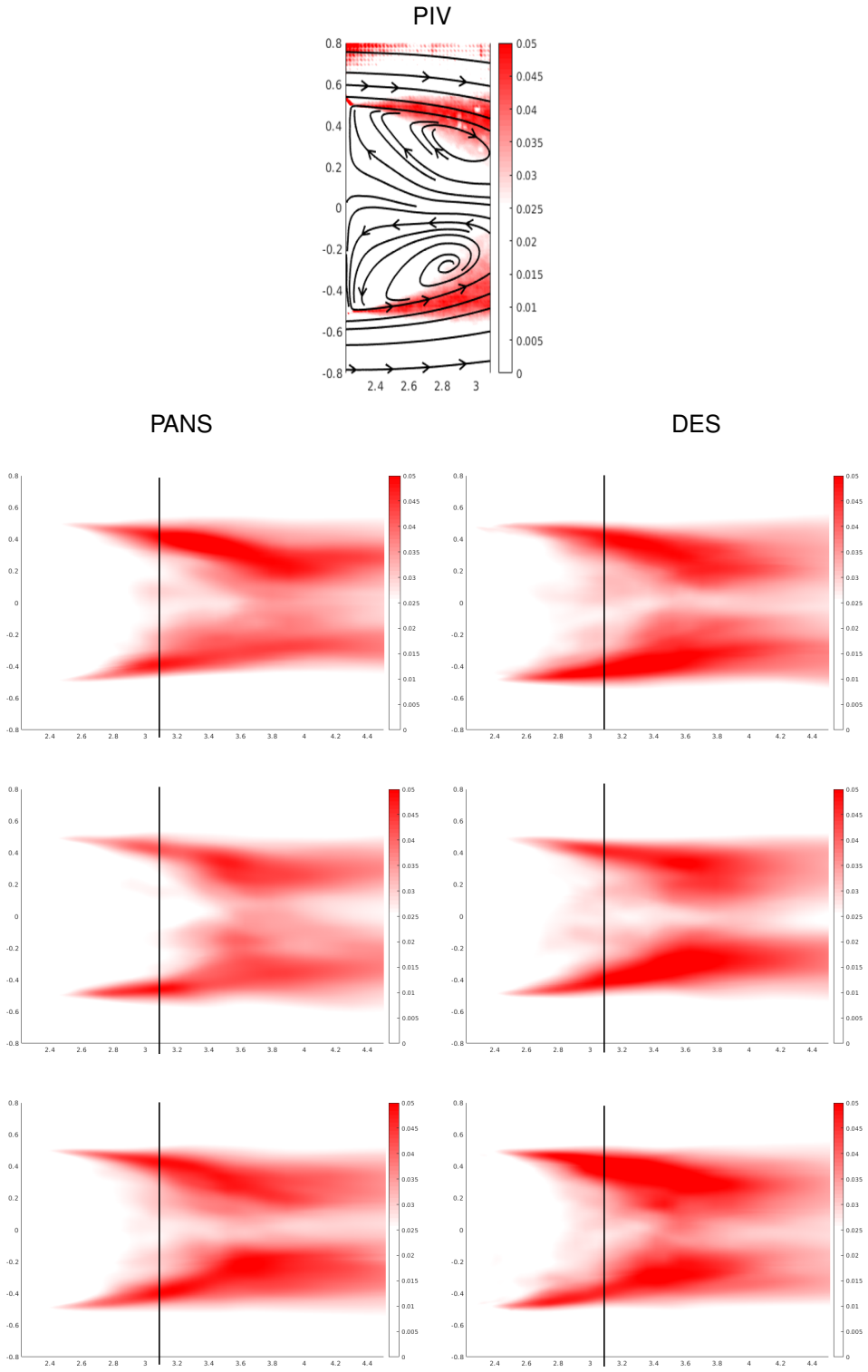

Figure 4.19: Contours of $\frac{\overline{u'u'}}{U_{inf}^2}$ on the $z = 0$ plane, of the PIV results and of the results with coarse (first row), medium (second row) and fine (third row) meshes. The vertical black lines on the CFD results represent the extreme right position of the PIV window.

4.1.8 Blending factors and flow structures

As seen in section 2.1, the PANS and DES simulations adapt to the computational grid used, the immediate flow field features, and in the IDDES case, also to the the wall distance, leading to different levels of resolved turbulence scales, complemented with turbulence models. The PANS model uses a set of equations which includes the dynamic factor f_k sensitive to each cell size and to the level of turbulence, in terms of kinetic energy, at each time step, enabling it to blend between DNS and the RANS base model. Whereas the DES model is set up so that boundary layers and irrotational flow regions are solved using a base RANS model, while regions where the grid is fine enough, is far away from walls, and the flow is massively separated it behaves as an LES subgrid scale model.

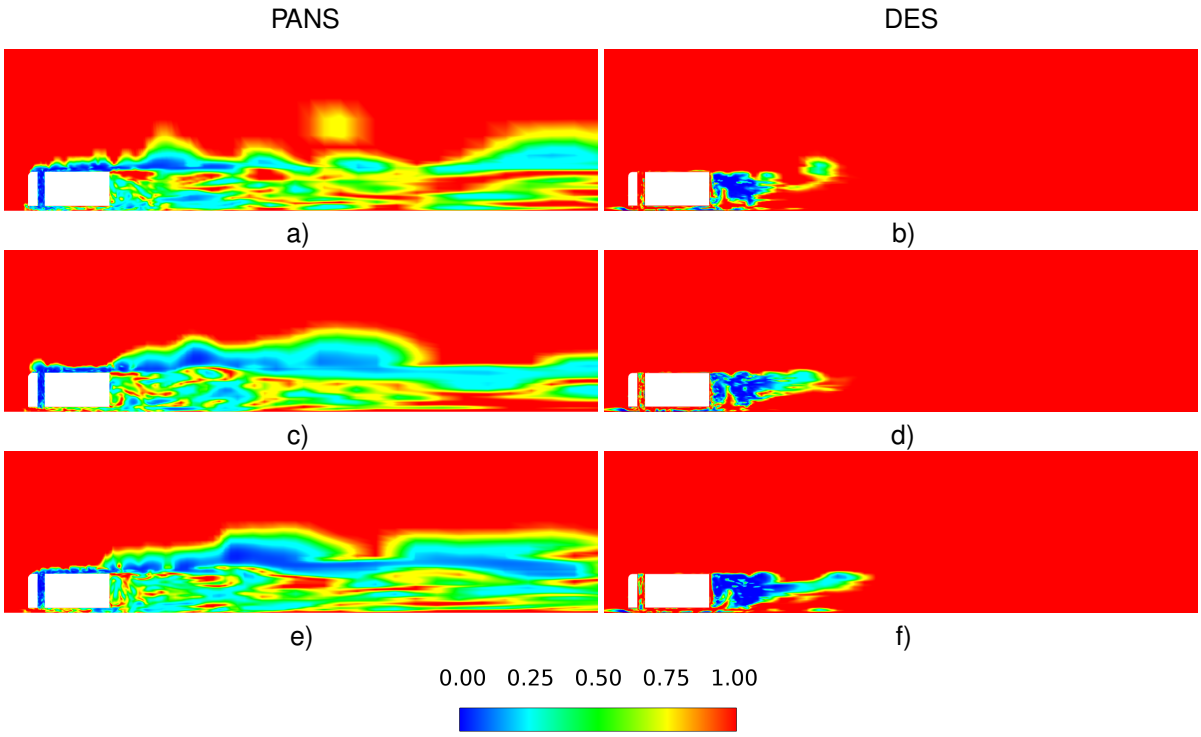

Figure 4.20: Contours of the f_k ratio, for PANS, and DES Upwind Blending Factor, for DES, on the $z = 0$ plane, using the coarse mesh, a) and b), medium mesh, c) and d), and fine mesh, e) and f).

The goal in this section is to analyze how the models are behaving in each case, this is, where PANS behaves as DNS, RANS or in-between and where DES is behaving as LES, RANS or in-between. For PANS, this analysis is directly done by observation of the input variable f_k. For IDDES it is not as straightforward, since the filtering is done through several variables, as previously seen on section 2.1.2. So, the analysis is indirectly done by the observation of the variable DES upwind blending factor, which indicates how the the Hybrid Second-Order Upwind/Central Difference Scheme is working, this is how much of upwind differencing scheme is being used in comparison with central differencing scheme. It

is correlated with how the model is handling the flow since the upwind differencing scheme is mainly used for RANS, while central differencing is used for LES. This way the DES Upwind Blending Factor indicates unity for areas such as attached shear layers and irrotational free-stream flow, and zero for areas where LES is required such as massively separated regions.

Figure 4.20 show the influence of the grid coarsening and refinement on the blending factor, f_k, for PANS, and on the DES Upwind Blending factor, for DES. Comparing this two blending factors between methods, one can see how differently the two methods approach the concept of bridging/ hybrid model, as explained previously. The PANS results present zero or close to zero f_k values in regions of high refinement and high turbulent kinetic energy, which is on the gap between the cabin and the trailer, on and near shear layers (including the top free shear layer), and along the trailer's wake, where the mesh is refined enough and there is large regions of recirculation. One can see that from PANS with coarse mesh to PANS with medium mesh, the regions of lower f_k increase. The same behaviour, although less evident, is present from the PANS with medium mesh to fine mesh results, where the region of low f_k value is larger around the rear of the trailer, along the wake and close to the outlet. This is in accordance with the model formulation as by refining the mesh, the Δ value is smaller, leading to lower f_k values, by Eq. 2.18. However, the coarse mesh results present a close to zero f_k region underneath the cabin that is not present with the more refined meshes, which is inconsistent. Across all meshes, the PANS results present large regions where f_k takes values close to zero and the solution approaches the DNS like behaviour above (outside) the big recirculation zone on the wake, while inside the recirculation zone of the wake, although the f_k values are low, there are very few and small regions where $f_k = 0$, much less than it would be expected. Also, one would expect a much bigger difference of f_k values on the wake with the refinement of the mesh.

On the DES simulations, we can see the DES upwind blending factor obtained, Fig. 4.20.b), d), f), are in accordance with the theory, as the wake region presents close to zero or zero values of DES upwind blending factor, while near the truck surfaces presents equal to 1 values. As the turbulence decreases away from the wake, the DES shows a blending factor of 1, treating the flow there entirely as RANS. As the mesh is refined, from coarse to fine, the increase of close to zero, and low value DES upwind blending factor regions is obvious, on the gap between the cabin and trailer and specially on the wake, which is in accordance with the DES model formulation. It would have been expected that the gap would have larger regions with the blending factor close to zero, as it is a region of high separation. The reason this doesn't happen might be due to that region being between two wall surfaces, which triggers the DES model into not using the LES module.

Overall, the DES results show a RANS treatment in all regions near the truck's surfaces, modeling therefore the entire region. PANS treats the flow near the truck's surface with a close to DNS behaviour. This is also coherent with the results analyzed in section 4.1.4.A, referring to the velocity and Reynolds

stresses profiles along the trailer. When it comes to the wake region, on one side the DES results show to resolve more of this region closer to the trailer's base, as it presents much larger areas of zero value of the blending factor than the PANS results. On the other side PANS results present low blending values on a longer extension of the wake, down until the outlet, i.e. in the streamwise direction, while the regions of $f_k = 0$ are surprisingly scarce, even close to the trailer base. This is also in accordance with the results in section 4.1.4.B. The DES with coarse mesh already presents a decent region of zero value of the blending factor on the wake region, while the PANS results present unexpectedly higher values of f_k. The gap between the cabin and the trailer is an interesting region, as PANS has a close to DNS behaviour in all of it, while DES majorly behaves as RANS, even though there's high separation and turbulence there, leading to believe that it is a weak spot for the DES model.

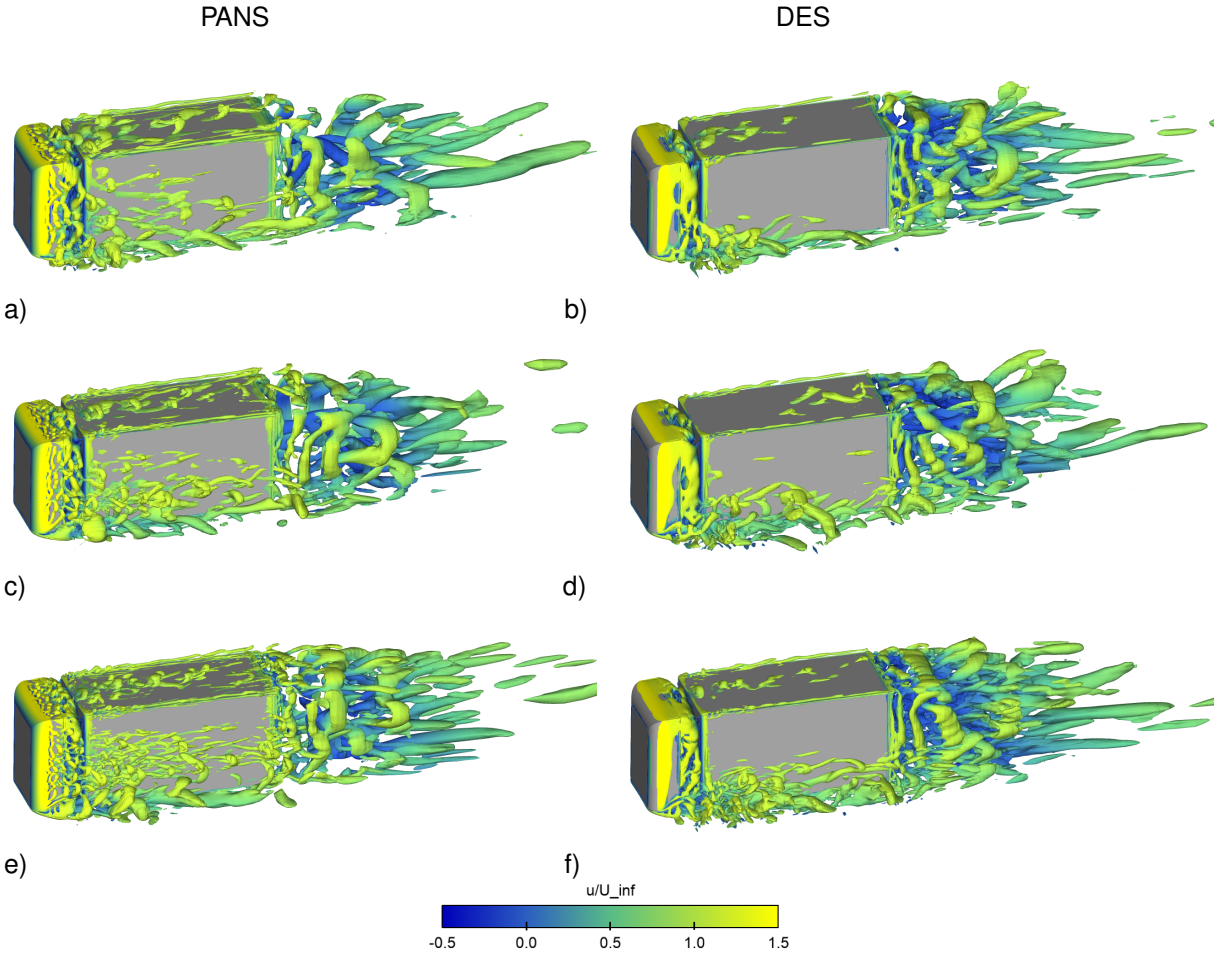

Figure 4.21: Representation of the iso-surfaces of the second invariant of the velocity gradient, $Q = 1500s^{-2}$, coloured by the normalized stream wise velocity component

In Fig. 4.21, in order to compare the instantaneous flow structures around the truck model between the two methods and to analyze the effect of mesh refining, the iso-surfaces of the second invariant of the velocity gradient, $Q = 1500s^{-2}$, are visualized. The iso-surfaces are coloured by the normalized

stream wise velocity component. This method is particularly good to study the geometry of flow patterns near no-slip boundaries and in areas of flow separation and reattachment. Analyzing all results on Fig. 4.21, it is possible to state that all PANS results present laminar like structures from the start of the top, and side, corners of the cabin, until the end of the corner, which is not detected in DES results. As the round corner ends, the PANS results show unsteady flow separation characterized by small-scale flow structures, which extend along the top and sides of the cabin and eventually are sucked into the gap between the cabin and the trailer. In PANS, along all horizontal surfaces of the cabin small hairpin structures are born and the gap is filled with tangled structures. As the mesh is refined, the PANS results show more and smaller of this smaller hairpin structures. However, the DES results show laminar like structures all around the cabin, which extend into large structures that fill in the gap, with exception of the flow around the lower corner of the cabin. It is clear that in this region, the coarse mesh with PANS captures more of the vortical structures than the finest mesh with DES. Looking to both PANS and DES results, one chain of flow structures that stick out is the intertwined vortices structures that are generated in the lower corners of the cabin and extend in the free-stream direction along the trailer lower corner, from small to larger eddies. Referring to this chain of structures between methods, for the same mesh, one can see that for the coarse mesh, the PANS and DES results show a similar amount of structures, and for the medium and fine mesh, the DES results show similar but noticeably smaller structures than PANS results, denoting the capturing of more unsteady scales of motion. Both methods identity the vortices created by the top sharp corners of the trailers along its whole length, although the PANS results show a better resolution of the structures when comparing the same mesh between methods. Another structures that stand out on the PANS results are the multiple hairpin structures created along the top and side surfaces, which get better resolution as the mesh is refined, capturing more vortical structures. On the other hand, the DES results can barely identify any structures on this surfaces. Finally, the most obvious concentration of vorticity, the wake, is analyzed. The wake is the region where a bigger amount of structures can be found and it is also where the largest structures are found. Across the three meshes we see that PANS, when compared with DES using the same mesh, is able to resolve smaller eddies around the truck model and inside the gap, but on the wake the DES results present a better resolution of structures, which is in accordance with the blending factor analysis done previously.

Overall, for both methods, as the mesh is refined, the bigger is the spectrum of structure size identified and more are the structures present. All results show a fairly similar description of the flow. We can see a clear correlation between the blending factor values presented on Fig. 4.20 and the Q-criterion iso-surfaces presented on Fig. 4.21. Ideally, the finer the mesh, the lower the values of the blending factors, f_k and DES upwind blending factor, the more scales are resolved and therefore smaller structures are identifiable in the results of the Q-criterion. This was verified in results presented in this section.

Also, to notice that in Fig. 4.20 the PANS results present f_k values close to zero all around the truck model and on the gap between the cabin and the trailer, while the DES present values of the blending factor close to one, and on the wake, we can see for the same mesh, the DES always have significantly lower values of the blending factor. This aligns well with the Q-criterion results presented on Fig. 4.21, as for the same mesh, PANS presents smaller eddies around the truck model and inside the gap, but it is DES results that is able to capture smaller structures on the wake of the truck model. It is important to notice that the Q-criterion alone does not prove which model can better resolve the flow.

4.2 Dynamic Results

The results presented in the previous section, have provided important information about the features of the flow, and how the PANS and DES models behave solving the flow around the truck model, when different levels of refined grids are used.

In this section, the PANS model is used to study the effect of the application of active flow control (AFC) on a dynamic oscillating configuration of a truck model, which is a flow configuration which is more close to reality. For this, two simulations are conducted, having exactly the same settings, the only difference being the implementation of AFC on the front pillars of the trailer. The AFC application produces pulsating jet flows with a normalized frequency of $F^+ = 3.1$, as an attempt to stabilize the flow around the truck, improving its dynamic efficiency, as explained in section 1.1. Both simulations have the same inlet conditions, with an inlet velocity of 9.438 m/s oscillating in its direction between $-10^\circ < \beta < 10^\circ$, with a width based Strouhal frequency of $St = 0.1$. The truck model studied is the same as the one from the $\beta = 0$ studies, only with the difference of having 45 cm width, so there is an accentuated flow separation on the trailer's front pillar. This raises the simulations Reynolds number to $\mathrm{Re} = 2.8x10^5$. For both dynamic simulations, 0.5 s (half a passage) were ran with the static settings, after which the dynamic conditions were implemented. The results started being averaged after one full sweeping cycle and were ran for two more cycles. All results presented were taken after the averaging of two full sweeps.

4.2.1 Drag Coefficient

The application of active flow control to the trailer's front pillar under the described oscillating conditions aims to smooth and stabilize the flow around the trailer and to minimize the hysteresis effect, ultimately leading to an overall drag reduction on the truck model.

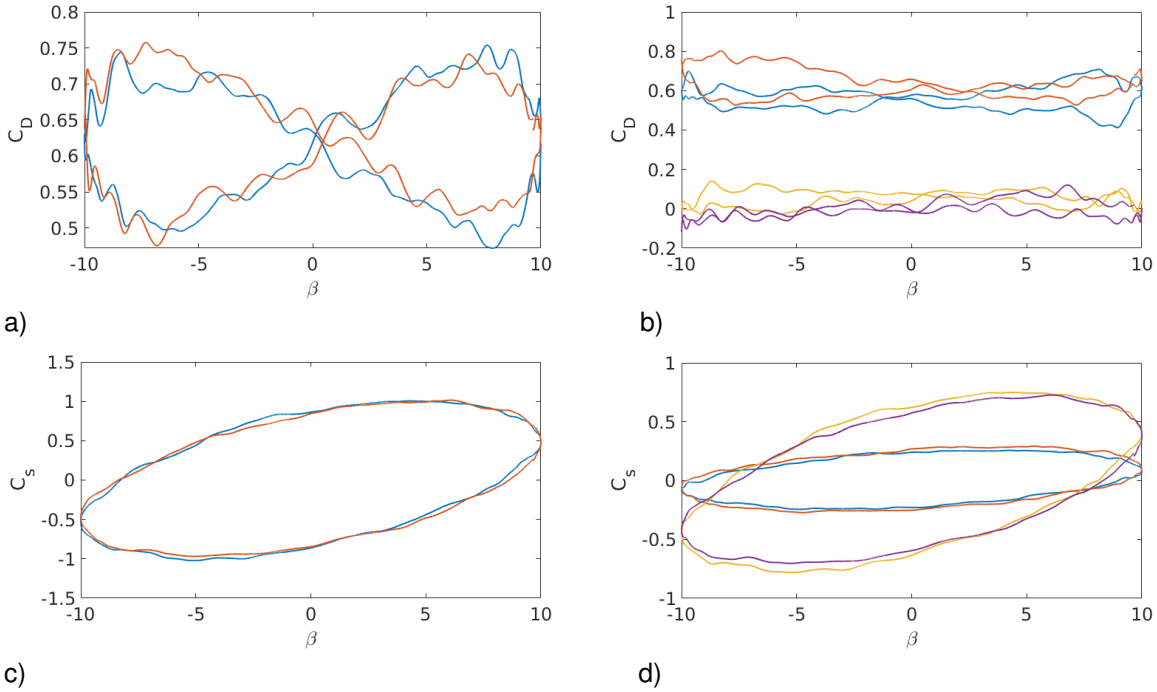

Figure 4.22: C_d of the complete truck, a), and cabin and trailer components, b), and C_s of the complete truck, c), and cabin and trailer components, d).
a) and c): Orange - AFC on, Blue - AFC off
b) and d): Blue - Cabin with AFC off, Orange - Cabin with AFC on, Yellow - Trailer with AFC off, Purple - Trailer with AFC on

However, by looking at Fig. 4.22, a), one can see that the application of AFC on the trailer's front pillars actually is not an effective solution. The Fig. 4.22, a) shows the full truck model drag signals of the dynamic actuated (orange line) and unactuated (blue line) cases during a full sweep, and it is possible to see that the application of AFC leads to an increase of the truck's drag coefficient along almost all the yaw angles and no improvement of the hysteresis effect is seen. Due to the application of AFC, the drag has a maximum increase of 13% and 10% when $\beta = 8.1°$ and $\beta = -7.4°$, respectively, and a maximum decrease of 8.7% and 5.8% when $\beta = 8.7°$ and $\beta = -6.9°$, respectively. Over a full oscillation, the average C_d of the truck with and without actuation is 0.6257 and 0.6151, so the application of AFC on the trailer's front pillar contributes to an average increase of 2%, which renders its use as ineffective in drag reduction, at least at this actuation frequency. By looking at Fig. 4.22.c), one can see that the application of AFC barely had any effect on the side force coefficient, C_s, failing to decrease the hysteresis effect. One can also notice a large inertial effect of the flow, as the C_s values of the truck are far from zero at $\beta = 0°$.

To better understand why the AFC application is ineffective, it is important to look at both bodies of the truck model, the cabin and the trailer. Fig. 4.22.b) shows the different drag signals of the cabin and trailer on the dynamic actuated and unactuated cases, where it is possible to verify that the cabin

is the major contributor for the full truck drag coefficient, showing values one order of magnitude higher for some yaw angles, when compared to trailer's C_d. The application of AFC caused an increase of the cabin's drag coefficient for almost the full oscillation range, presenting a maximum increase of 48% and 35% at $\beta = 9°$ and $\beta = -7°$, respectively, and an average increase of 12.3% over a full oscillation. Even though a major reduction of the trailer's C_d is evident, averaging a 127.5% C_d reduction, it is still 15.3% lower than the cabin C_d increase, resulting in the overall increase of the full truck C_d. Figure 4.22.d), shows the side force coefficient on the cabin and trailer during a whole sweep, for the actuated and unactuted cases. One can see that the cabin is the major contributor for the truck's C_s and hysteresis effect, and that there is no significant difference on the cabin and trailer with the current AFC application.

In this case, the overall C_d of the truck didn't decrease due to the fact that the trailer's C_d decrease wasn't high enough to counteract the cabin's increase of C_d. This leads to believe that there is the possibility of reducing the truck's overall C_d by applying the AFC on the trailer's front pillars, in a way that it has less effect on the cabin's C_d. This could be done by applying a different actuation frequency or more likely by applying the actuation jets in a different direction, instead of normal to the surface.

4.2.2 Flow Behaviour

In this section, an analysis of the flow behaviour during the yaw oscillation is presented for both the actuated and unactuated cases. In Fig. 4.23 the instantaneous streamwise flow velocity is presented for four different yaw angles, $4.7°$, $-8.8°$, $-4.7°$, $8.8°$. There, one can see that the fluctuations produced by the dynamics of the case significantly affects the aerodynamic performance. Also, there's a flow inertial effect that is clearly seen in Figures 4.23 and 4.24, as the presented wakes don't always align with the model's inlet velocity. Figure 4.24 presents iso-surfaces of the second invariant of the velocity gradient, $Q = 1500s^{-2}$, coloured by the normalized stream wise velocity component. For the unactuated case, at $\beta = \pm 8.8$ it is possible to see in Fig. 4.23.b),d), that even though the flow is coming at a $\beta \neq 0$, the unactuated case present an attached flow along almost the whole trailer, which is due to the model rotation, since a static study at that yaw angle would cause separation at the cabin and trailer leeward sides. However, by applying the AFC on the trailer's front pillar, Fig. 4.23.f),h), one can see that the flow is now separated along the entire trailer's windward side, directly interacting with the wake. This shows that the AFC is destabilizing the flow, which is the opposite effect of what it is supposed to have. It is also possible to notice that the use of AFC makes the recirculation region on the gap between the cabin and trailer larger, which is likely the reason for the for the increase of the cabin C_d and decrease of the trailer C_d. This is also visible on Fig. 4.24, where the application of AFC seems to delay the braking of some of the structures and shows more structures on the cabin and trailer windward side. In Fig. 4.24.a),e),c),g), it is possible to identify the rolling up of a long stream-wise vortex that extends from front of the trailer to its wake, and contributes to a drag increase.

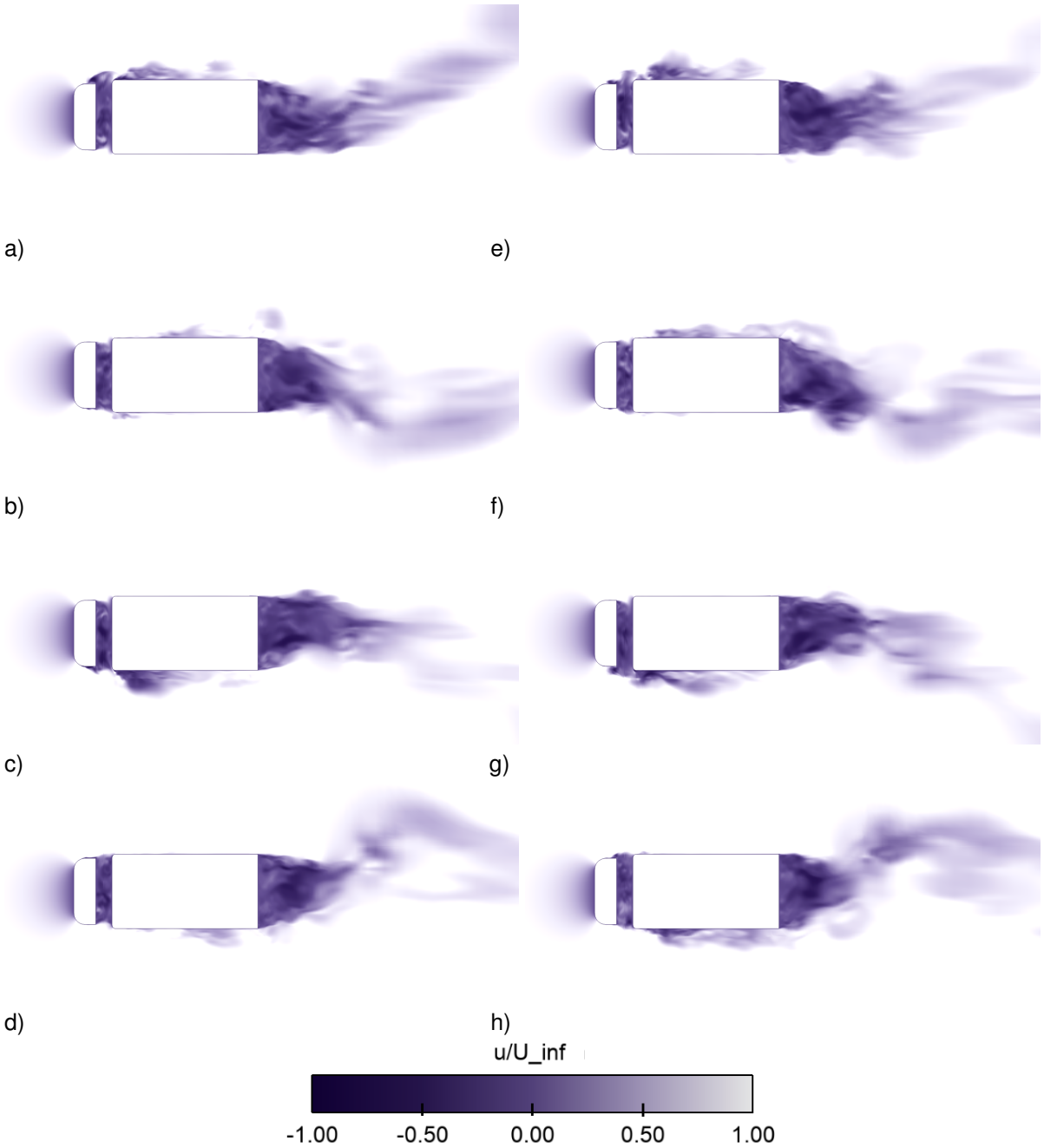

Figure 4.23: Instantaneous stream-wise flow velocity. a) to d) represent the unactuated case and e) to h) the actuated one. $\beta = 4.7^{\circ}$ counter-clock wise rotation: a) and e); $\beta = -8.8^{\circ}$ counter-clock wise rotation: b) and f); $\beta = -4.7^{\circ}$ clock wise rotation: c) and g); $\beta = 8.8^{\circ}$ clock wise rotation: d) and h)

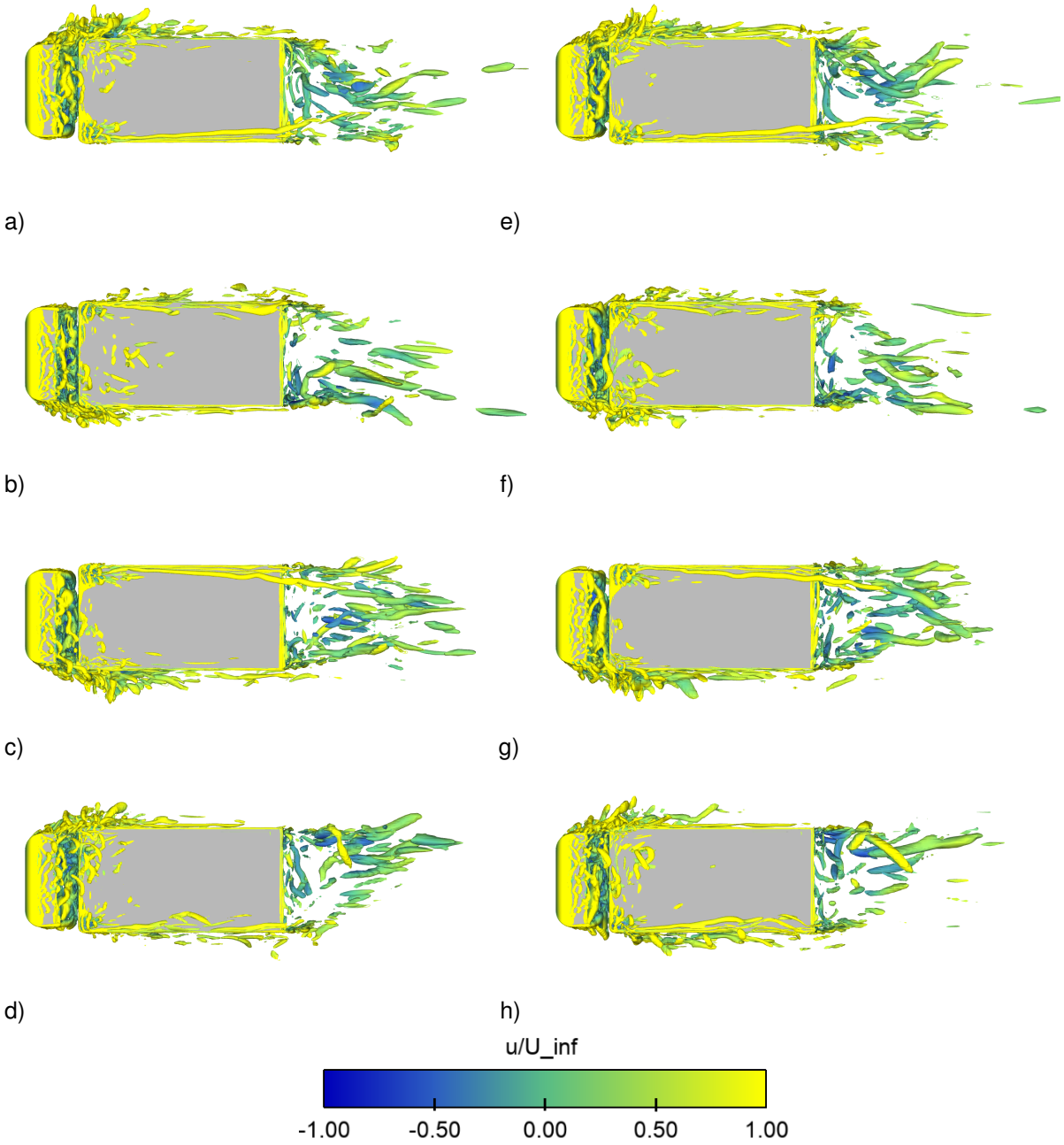

Figure 4.24: Iso-surfaces of the second invariant of the velocity gradient, $Q = 1500s^{-2}$ colored by the instantaneous stream-wise flow Qocity. a) to d) represent the unactuated case and e) to h) the actuated one. $\beta = 4.7^{\circ}$ counter-clock wise rotation: a) and f); $\beta = -8.8^{\circ}$ counter-clock wise rotation: b) and g); $\beta = -4.7^{\circ}$ clock wise rotation: c) and h); $\beta = 8.8^{\circ}$ clock wise rotation: d) and i)

4.2.3 PANS performance

During the simulation of both cases, an interesting behaviour of the PANS blending function, f_k, was noticed. Figure 4.25 shows the input f_k ratio of both cases, and one can see that the model is treating most of the flow with a close to DNS behaviour, meaning that the model is ineffective with the dynamic settings used in this simulations, more precisely, the application of unsteady inflow conditions of this magnitude, as it imposes some turbulent content that is enough to trigger the PANS model into activating the DNS mode, even though the mesh is not fine enough. This is not a problem near the truck model and in the wake as the mesh there has the proper refinement, but it could be a problem outside this region where the mesh is coarser. This should be taken into consideration when reading this section. It is important to notice that the small structures that are present in the shear layer, formed on the the trailer front pillars, are still being captured, which is of great importance due to their dynamically importance for the side wake formation. An improvement of the PANS model is under investigation at the moment, where the variable f_k is being reformulated into taking into account only turbulent fluctuations, and discarding temporal ones. This work provides a new insight that contributes to the new formulation.

A solution to this problem is imposing the model rotation by mesh deformation on a circular portion of the mesh, around the model, as successfully applied in [3]. It would be interesting to see if the IDDES model used on the static cases would perform better with the simulation settings here presented, as the IDDES is equipped with a WMLES branch which is activated for unsteady inflow conditions.

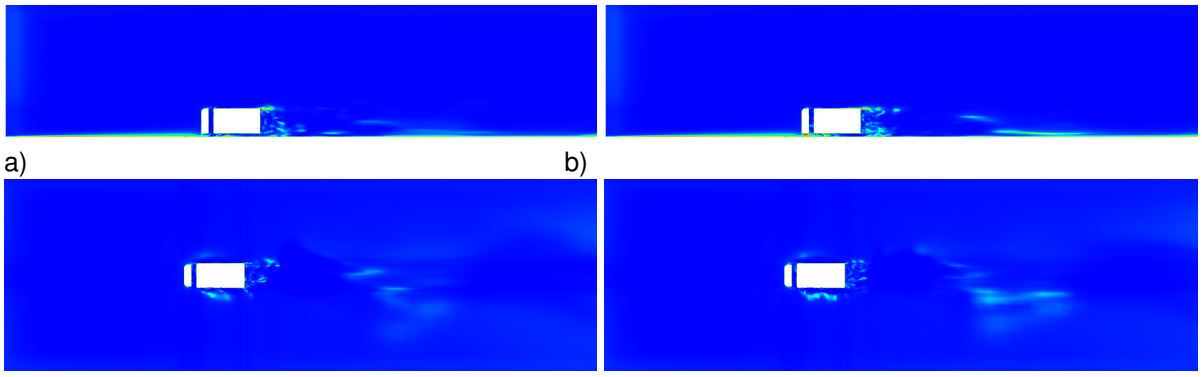

Figure 4.25: Contours of the f_k ratio of the dynamic simulation results at $\beta = 8.8°$ (clockwise rotation), on the plane $y = 0$ and $z = 0$ planes, for the unactuated case, a), c), and the actuated case, b) and d).

5

Conclusion

5.1 Conclusions

Unsteady numerical simulations were carried out to understand the physics of the flow around a simplified tractor-trailer model at $Re = 2.5 \times 10^5$, as well as to conduct a detailed comparison of the PANS and DES performance in predicting the unsteady turbulent flow, and its behaviour to different levels of grid refinement. The simulations were performed using PANS and DES across three structured hexahedral grids of increasing resolution. The comparison of PANS and DES in predicting the flow, using three different refinement level grids, was carried out trough the analysis of the aerodynamic forces, velocity and Reynolds stress profiles (including comparison with unpublished experimental results), surface pressure coefficient profiles and visualization, identification and localization of the flow features through the analysis of averaged streamlines, visualization of vorticity and Reynolds stresses, and analysis of instantaneous flow structures around the model.

The results show that PANS and DES predict very similar values of C_d, across all the three meshes and between methods. The same is verified for C_l for the DES results, and for the PANS results when using medium and fine mesh, while with coarse mesh the PANS results present significantly different C_l

values from the other results, specially for the cabin.

When it comes to the velocity and Reynolds profiles, on the trailer the DES results are always very similar between meshes, but significantly different from the PANS results, while the PANS present similar profiles between the medium and fine mesh, but bigger discrepancy for the coarse mesh. Once again, showing poorer performance of the coarser mesh when used with PANS. In the trailer Reynolds stresses profiles analysis, it is possible to see that the DES models the flow near the surface, while PANS tries to partially resolve it, which is the reason the DES results across the three meshes are so similar. In the wake, u/U_{inf} profiles obtained from the numerical simulations always over-predicts the magnitude when compared to the PIV results, while for the Reynolds stresses profiles, the opposite happens, it under-predicts. Both methods, across all meshes, don't capture the peaks of the profiles precisely, but almost all capture the trends present in PIV results. In the wake it is the DES results that present higher Reynolds stresses profiles and come closer to the PIV results. The DES surface pressure coefficient profiles results present very consistent results through the meshes, while the PANS with coarse mesh results present considerable discrepancies from the medium and fine mesh results. Also, the DES results present a more realistic pressure profile around the cabin.

The results show that both PANS and DES simulations capture the same main flow features and produce similar trends, which are in accordance with works such as [1,61, 65], among others. It was found the presence of asymmetry in the wake flow at zero yaw angle, which is consistent with previous numerical and experimental results. This presence of asymmetry is independent of the method and mesh.

After analyzing the turbulence models' blending factors and the instantaneous flow structures, it was shown that PANS is resolving less of the flow in the wake than it would be expected and that the DES has the same problem, but directed to the gap between the cab and the trailer.

Overall, the DES results are more correlated, as the profiles taken along the trailer and along the wake mostly overlap, from the coarsest mesh to the finest, which is not the case for PANS as the coarse profiles are noticeably different from the ones obtained using finer meshes and even the finer meshes don't overlap as good as the DES ones.

The second part of the thesis was focused on providing a first look into how viable the application of AFC in the trailer front pillars is, in order to mitigate the flow separation and consequently enhancing its aerodynamic performance on the gap region, during close to real conditions. The dynamic simulation results showed the creation of an hysteresis effect on the C_d and C_s signals, created by the inertia of flow during the oscillations. When it comes to the effect of the actuation on the dynamic case, it was possible to see that the flow is not stabilized by the AFC, as the hysteresis of the C_d and C_s signals were not decreased. Most important, it was observed an overall increase of C_d due to the AFC application, as the decrease in the trailer's C_d was not enough to counteract the increase of the cabin's C_d, suggesting

the need to change the AFC configuration and/or parameters in order to obtain better results.

As PANS failed to effectively use its bridging capabilities to treat the dynamic flow under the applied settings, it was concluded that the use of PANS is ineffective to study dynamic cases, when the oscillation is imposed by the boundary layers, since it introduces some turbulent content that is enough to trigger the PANS model into activating the DNS mode. However, a new formulation of the PANS model that solve this problem is being developed.

5.2 Future Work

Both two parts of the thesis present aspects that should be improved. In the comparison between DES and PANS methods there is a lack of experimental results necessary to distinguish which of the methods represent the unsteady turbulent flow more accurately.

On the dynamic cases, it was concluded that the way the oscillation was introduced to the case is not supported by PANS. So, a mesh deformation on a circular portion of the mesh around the model should be applied, as successfully applied in [3]. It would also be interesting to simulate with DES the dynamic cases, using the same boundary conditions used in this work, as well as using the new PANS formulation when available.

Since the AFC application was rendered ineffective for the one configuration used, different configurations should be considered, such as setting the actuation slot in a different position of the pillar or to apply an actuation at a different angle with the surface.

Bibliography

[1] H. Choi, J. Lee, H. Park, ”Aerodynamics of Heavy Vehicles”, *Annual Review of Fluid Mechanics*, vol. 46, pp. 441-468, 2014.

[2] B. Chiekh, M. Ferchichi, M. Michard, M. Guellouz, M. S. Béra, ”Synthetic Jet Actuation Strategies for Momentumless Trailing Edge Wake,” *Journal of Wind Engineering and Industrial Aerodynamics*, vol. 113, pp. 59-70, 2013.

[3] G. Minelli, S. Krajnović, B. Basara. ”A Flow Control Study of a Simplified, Oscillating Truck Cabin using PANS,” *Journal of Fluids Engineering*, vol. 140, no. 12, 2018.

[4] E. A. Mohammad, V. Chernoray, M. Jahanmiri, and L. Davidson, "Experimental and Computational Studies of Active Flow Control on a Model Truck-Trailer," *EPJ Web of conferences*, vol. 25, no. 16, 2012.

[5] R.M Wood, "A Discussion of a Heavy Truck Advanced Aerodynamic Trailer System," *International Forum for Road Transport Technology (IFRTT) 9th International Symposium on Heavy Vehicle Weights and Dimiensions*, 2006.

[6] G. Minelli, E. Hartono, V. Chernoraya, L.Hjelm, B.Basara, S.Krajnović, "Validation of PANS and Active Flow Control for a Generic Truck Cabin," *Journal of Wind Engineering and Industrial Aerodynamics*, vol. 171, pp. 148-160, 2017.

[7] C. HÅKANSSON, M. J. LENNGREN, "CFD Analysis of Aerodynamic Trailer Devices for Drag Reduction of Heavy Duty Trucks," Chalmers tekniska högskola, 2010.

[8] Kevin P. Garry and Kevin R. Cooper. "Comparison of Quasi-static and Dynamic Wind Tunnel Measurements on Simplified Tractor-trailer Models," *Journal of Wind Engineering and Industrial Aerodynamics*, Vol. 22 (2-3), pp. 185-194, 1986.

[9] G. Minelli, B. Basara, S. Krajnovic, "A LES Study on the Effect of Periodic Gusts on a Truck Model," *International Conference on Jets, Wakes and Separated Flows*, 2017.

[10] G. Minelli, S. Krajnović, B. Basara, B.R. Noack, "Numerical Investigation of Active Flow Control Around a Generic Truck A-pillar, Flow," *Turbulence and Combustion*, vol. 97, pp. 1235–1254, 2016.

[11] J. Östh, S. Krajnović, "A Study of the Aerodynamics of a Generic Container Freight Wagon Using Large-Eddy Simulation," *Journal of Fluids and Structures*, vol. 44, pp. 31–51, 2014.

[12] S. Krajnović, L. Davidson. Exploring the Flow Around a Simplified Bus with Large Eddy Simulation and Topological Tools. In: McCallen, R., Browand, F., Ross, J. (Eds.), The Aerodynamics of Heavy Vehicles: Trucks, Buses, and Trains. Springer Berlin Heidelberg, Berlin, Heidelberg, pp. 49–64, 2004

[13] Spalart P.R., Jou W.H., Strelets M., and Allmaras S.R., Comments on the Feasibility of LES for Wings, and on a Hybrid RANS/LES Approach, 1st AFOSR Int. Conf. on DNS/LES, Aug. 4-8, 1997, Ruston, LA. In: Advances in DNS/LES, C. Liu and Z. Liu Eds., Greyden Press, Columbus, OH, USA (1997).

[14] H. Hemida, S. Krajnović, "LES Study of the Influence of the Nose Shape and Yaw Angles on Flow Structures Around Trains," *Journal of Wind Engineering and Industrial Aerodynamics*, vol. 98, no. 1, pp. 34-46, 2010.

[15] J. Zhang, J. Li, H. Tian, G. Gao, J. Sheridan, ”Impact of Ground and Wheel Boundary Conditions on Numerical Simulation of the High-speed Train Aerodynamic Performance,” *Journal of Fluids and Structures*, vol. 61, pp. 249-261, 2016.

[16] E. Guilmineau, G. Deng, J. Wackers, ”Numerical Simulation with a DES Approach for Automotive Flows,” *Journal of Fluids and Structures*, vol. 27, no. 5–6, pp. 807-816, 2011.

[17] S. Girimaji, R. Srinivasan, E. Jeong, ”PANS Turbulence Model for Seamless Transition Between RANS and LES: Fixed-point Analysis and Preliminary Results,” *ASME. Fluids Engineering Division Summer Meeting, vol. 2: Symposia, Parts A, B, and C, July 6-10, 2003, Hawaii, USA*, pp. 1901–1909, 2003

[18] S. Krajnović, R. Lárusson, and B. Basara. ”Superiority of PANS compared to LES in predicting a rudimentary landing gear flow with affordable meshes,” *Int. J. Heat Fluid Fl.*, vol. 37, pp. 109-122, 2012.

[19] M. Mirzaei, S. Krajnović, B. Basara. ”Partially-Averaged Navier-Stokes simulations of flows around two different Ahmed bodies,” *Computers Fluids*, vol. 117, pp. 273-286, 2015.

[20] G. Minelli, S. Krajnović, B. Basara. ”Partially-averaged Navier-Stokes Simulations of Two Bluff Body Flows”, *Applied Mathematics and Computation*, vol. 272, no. 3, pp. 292-706, 2016.

[21] H. Tennekes, J. L. Lumley, ”A First Course in Turbulence,” *The MIT Press, Cambridge, Massachusetts*, 1972.

[22] O. Osborne, “An experimental investigation of the circumstances which determine whether the motion of water shall be direct or sinuous, and of the law of resistance in parallel channels,” *Philosophical Transactions of the Royal Society*, vol. 174, pp. 935–982, 1883.

[23] S. Kurien and M. A. Taylor, ”Direct Numerical Simulations of Turbulence: Data Generation and Statistical Analysis,” *Los Alamos Science*, vol. 29, pp. 143-151, 2005.

[24] U. Piomelli, ”Wall-Layer Models for Large Eddy Simulations,” *Annual Review of fluid Mechanics*, vol. 34, pp. 349-374, 2002.

[25] T. Ishiara, T. Gotoh, and Y. Kaneda, ”Study of high-Reynolsd number isotropic turbulence by Direct Numerical Simulation,” *Annual Review of Fluid Mechanics*, vol. 41, no. 1, pp. 165-180, 2009.

[26] T. Ishiara, Y. Kaneda, M. Yokokawa, K. Itakura, and A. Uno, ”Small-Scale statistics in high-resolution Direct Numerical Simulation of turbulence: Reynolds number dependence of one-point velocity gradient statistics,” *Journal of Fluid Mechanics*, vol. 592, pp. 335-366, 2007.

[27] P. Schlatter, R. ÖRLÜ, ”Assessment of direct numerical simulation data of turbulent boundary layers,” *Journal of Fluid Mechanics*, vol. 659, pp. 116-126, 2010.

[28] W. Xiaohua, J. R. Baltzer and R. J. Adrian, ”Direct numerical simulation of a 30R long turbulent pipe flow at R^{+} = 685: large- and very large-scale motions,” *Journal of Fluid Mechanics*, vol. 698, pp. 235-281, 2012.

[29] H. Choi and P. Moin, ”Grid-point requirements for large eddy simulation: Chapman’s estimates revisited,” *Physics of Fluids*, vol. 24, no. 1, pp. 13-18, 2012.

[30] S. S. Girimaji, ”Partially-Averaged Navier-Stokes Model for Turbulence: A Reynolds-Averaged Navier-Stokes to Direct Numerical Simulation Bridging Method,” *Journal of Applied Physiscs*, vol. 73, pp. 413-421, 2006.

[31] S. S. Girimaji, E.Jeong, and R. Srinivasan, ”Partially Averaged Navier-Stokes Method for Turbulence: Fixed Point Analysis and Comparison With Unsteady Partially Averaged Navier-Stokes,” *Journal of Applied Physics*, col. 73, pp. 422-428, 2006.

[32] B. Basara, S. Krajnović, and S.S. Girimaji. ”PANS methodology applied to elliptic relaxation-based eddy viscosity transport model,” *Proceedings of Turbulence and interactions*, vol. 110, pp. 63-69, 2009.

[33] B. Basara, S. Krajnović, and S.S. Girimaji, Z. Pavlovic. ”Partially Averaged Navier-Stokes Method for Turbulence Simulations: Near-Wall Eddy viscosity Transport Model Implementation,” *AIAA Journal*, vol 49, no. 12, pp. 2627-2636, 2011.

[34] K. Hanjalić, M. Popovac, and Hadžiabdić, ”A Robust near wall elliptic-relaxation eddy-viscosity turbulence model for CFD,” *Int. J. Heat Fluid Fl.* vol. 25, pp. 1047-1051, 2004.

[35] D.C. Wilcox, “Turbulence Modeling for CFD,” 3rd edition, DCW Industries, Inc., 2006

[36] S. Kapadia, S. Roy, M. Vallero, K. Wurtzler, J. Forsythe, ”Detached-Eddy Simulation over a Reference Ahmed Car Model,” *Friedrich R., Geurts B.J., Métais O. (eds) Direct and Large-Eddy Simulation V. ERCOFTAC Series, vol 9. Springer, Dordrecht*

[37] F.R. Menter, M. Kuntz, R. Langtry, ”Ten years of experience with the SST turbulence model,” *4th International Symposium on Turbulence Heat and Mass Transfer*, pp. 625–632, 2003.

[38] M.S. Gritskevich, A.V. Garbaruk, J. Schütze, F.R. Menter, ”Development of DDES and IDDES Formulations for the k- Shear Stress Transport Model,” *Flow, Turbulence and Combustion*, vol 88, no. 3, pp 431–449, 2012.

[39] P. R. Spalart, S. Deck, M. L. Shur, K. D. Squires, M. Kh. Strelets, and A. Travin, "A New Version of Detached-eddy Simulation, Resistant to Ambiguous Grid Densities," *Theoretical and Computational Fluid Dynamics. Springer Berlin / Heidelberg.*, vol 20, no. 3, 2006.

[40] M. L. Shur, P. R. Spalart, M. K. Strelets, and A. K. Travin. "A Hybrid RANS-LES Approach With Delayed-DES and Wall-Modelled LES Capabilities," *International Journal of Heat and Fluid Flow*, vol. 29, no.6, pp. 1638-1649, 2008.

[41] F. R. Menter. "Two-equation eddy-viscosity turbulence models for engineering applications," *AIAA Journal*, vol. 32, no. 8, pp. 1598-1605, 1994.

[42] Spalart, P.R. and Rumsey, C.L. 2007. "Effective Inflow Conditions for Turbulence Models in Aerodynamic Calculations", AIAA Journal, 45(10), pp. 2544-2553.

[43] S.K. Arolla, P.A. Durbin, "Modeling rotation and curvature effects within scalar eddy viscosity model framework," *International Journal of Heat and Fluid Flow*, vol. 39, pp. 78-89, 2013.

[44] F. Menter, "Zonal Two Equation k-w Turbulence Models For Aerodynamic Flows," *23rd Fluid Dynamics, Plasmadynamics, and Lasers Conference, Fluid Dynamics and Co-located Conferences*, 1993.

[45] F. R. Menter. "Two-equation eddy-viscosity turbulence models for engineering applications," *AIAA Journal*, vol. 32, no. 8, pp. 1598-1605, 1994.

[46] P. A. Durbin, "On the k-e stagnation point anomaly," *International Journal of Heat and Fluid Flow*, vol. 17, no.1, pp. 89-90, 1996.

[47] P. SPALART and S. ALLMARAS, "A one-equation turbulence model for aerodynamic flows," *La Rech. Aerospatiale*, vol. 1, no.1, pp. 5–21, 1994.

[48] R.H. Croll, W.T. Gutierrez, B. Hassan, J.E. Suazo, A.J. Riggins, "Experimental Investigation of the Ground Transportation Systems (GTS) Project for Heavy Vehicle Drag Reduction," SAE Technical Paper 960907, 1996.

[49] J.T.Heineck, S.M. Walker, D. Satran, "The Measurement of Wake and Gap Flows of the Generic Conventional Truck Model (GCM) using Three-Component PIV," In: McCallen R., Browand F., Ross J. (eds) The Aerodynamics of Heavy Vehicles: Trucks, Buses, and Trains. Lecture Notes in Applied and Computational Mechanics, vol 19. Springer, Berlin, Heidelberg

[50] P. Castellucci, and K. Salari, "Computational Simulation of Tractor-Trailer Gap Flow with Drag-Reducing Aerodynamic Devices," SAE Technical Paper 2005-01-3625, 2005.

[51] M. Hammache, F. Browand, ”On the aerodynamics of tractor-trailers,” In: McCallen et al. 2004a, pp. 185–205, 2004.

[52] U. Piomelli, J.R. Chasnov, ”Large-eddy Simulations:Theory and Applications,” Kluwer Academic Publisher, 1996.

[53] S. Watkins and J. W. Saunders. ”Turbulence Experienced by Road Vehicles under Normal Driving Conditions,” *SAE Technical Paper Series*, 1995.

[54] S. Wordley and J. Saunders, “On-road Turbulence,” *SAE Int. J. Passeng. Cars - Mech. Syst*, 2009.

[55] S. Wordley and J. Saunders, “On-road Turbulence: Vol. 2,” *SAE Interna- tional Journal of Passenger Cars - Mechanical Systems*, vol. 2, pp. 111–137, 2009.

[56] A. Harten, ”High Resolution Schemes for Hyperbolic Conservation Laws,” *Journal of Computational Physics*, vol. 135, pp. 260–278, 1997.

[57] P. H. Gaskell, A. K. C. Lau, ”Curvature-compensated convective transport: SMART, A new boundedness- preserving transport algorithm,” *International Journal for Numerical Methods in Fluids*, 1988.

[58] D. Sujudi, R. Haimes, ”Identification of Swirling Flow in 3-D Vector Fields,” AIAA-95-1715, 1995.

[59] J. Östh, S. Krajnović, ”The flow around a simplified tractor-trailer model studied by large eddy simulation,” *Journal of Wind Engineering and Industrial Aerodynamics*, vol. 102, pp. 36-47, 2012.

[60] J.C.R. Hunt, A.A. Wray and P. Moin, ”Eddies, Streams, and Convergence Zones in Turbulent Flows,” Center for Turbulence Rereomh Proceedings of the Summer Program, 1988.

[61] H. J. Schmidt, R. WoszidloC, N. NayeriC, O. Paschereit, ”The effect of flow control on the wake dynamics of a rectangular bluff body in ground proximity,” Experiments in Fluids, 59: 107, 2018.

[62] B. Herry, ”Aerodynamic study of a 3D backward facing double step applied to safer launch and recovery of helicopters on ships,” *Mechanics of the fluids. Université de Valenciennes et du Hainaut-Cambresis*, 2010.

[63] A, Cogotti, ”Car-Wake imaging Using a Seven-Hole Probe,” SAE International Congress and exposition, Detroit, Michigan, 1986

[64] G. Minelli, ”A LES Study of a Modified Ahmed Body Geometry”, Chalmers tekniska högskola, 2012.

[65] D. McArthur, D. Burton, M. Thompson, J. Sheridan, ”On the near wake of a simplified heavy vehicle,” *Journal of Fluids and Structures*, vol. 66, pp. 293-314, 2016.

[66] G. Minelli, E.A. Hartono, V. Chernoray, L.Hjelm, and S. Krajnović, ”Aerodynamics flow control for a generic truck cabin using synthetic jets”, Journal of Wind Engineering an Industrial Aerodynnamics, vol. 168, pp. 81-90, 2017.

A

Appendix

A.1 Appendix 1

Complementing images of section 4.1.6

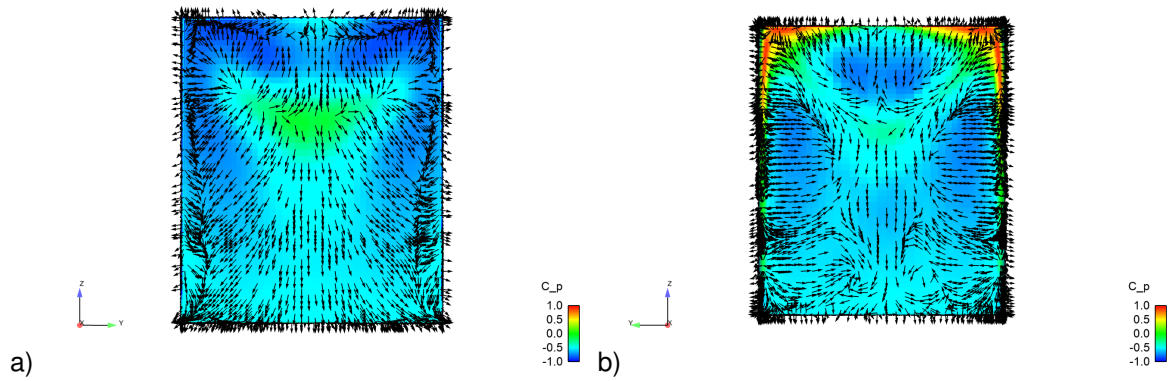

Figure A.1: Back view of the cabin, a), and front view of the trailer, b), colored by C_p and with the flow vectors projected to the surface.

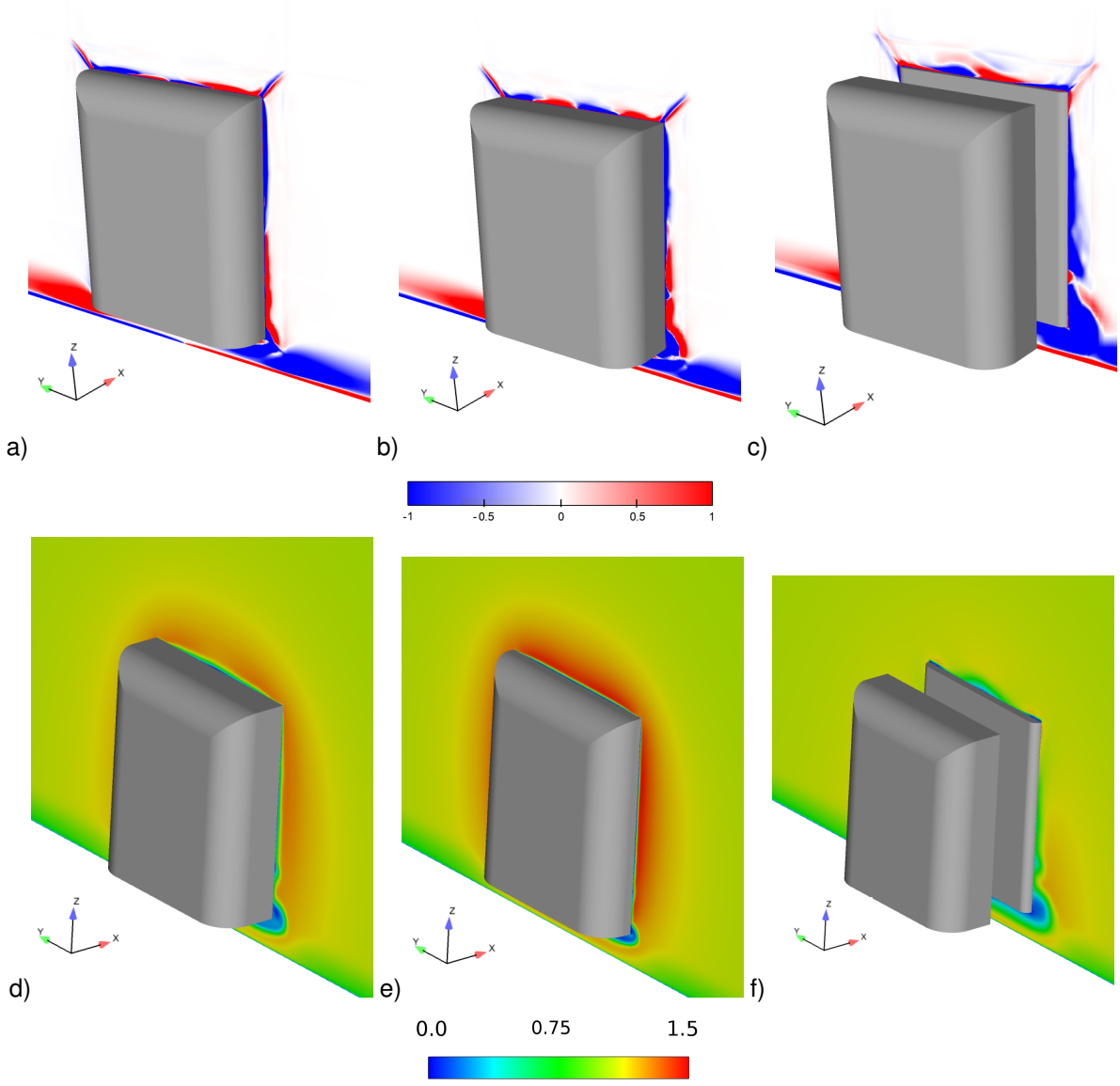

Figure A.2: Representation of the normalized flow average x-vorticity on the plane $x/W = -0.25$, a), $x/W = -0.375$, b), and $x/W = 0.05$, c), and representation of the normalized flow average velocity on the plane $x/W = -0.25$, d), and $x/W = -0.375$, e), and $x/W = 0.05$.

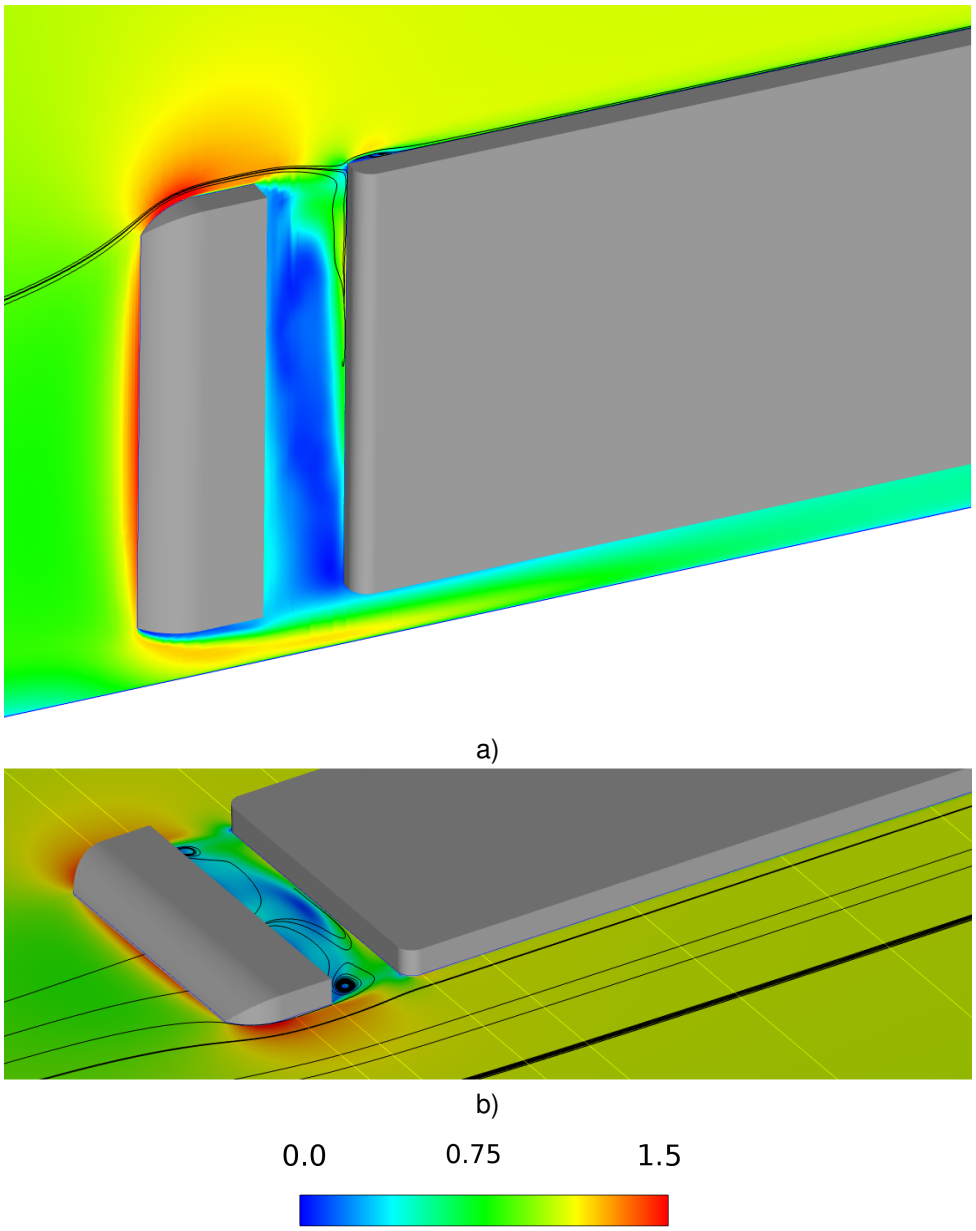

Figure A.3: Representation of the normalized flow average velocity on the plane $y = 0.49$ and $z = 0.5$, b).

A.2 Appendix 2

Closer view of the vorticity images, from section 4.1.7.A.

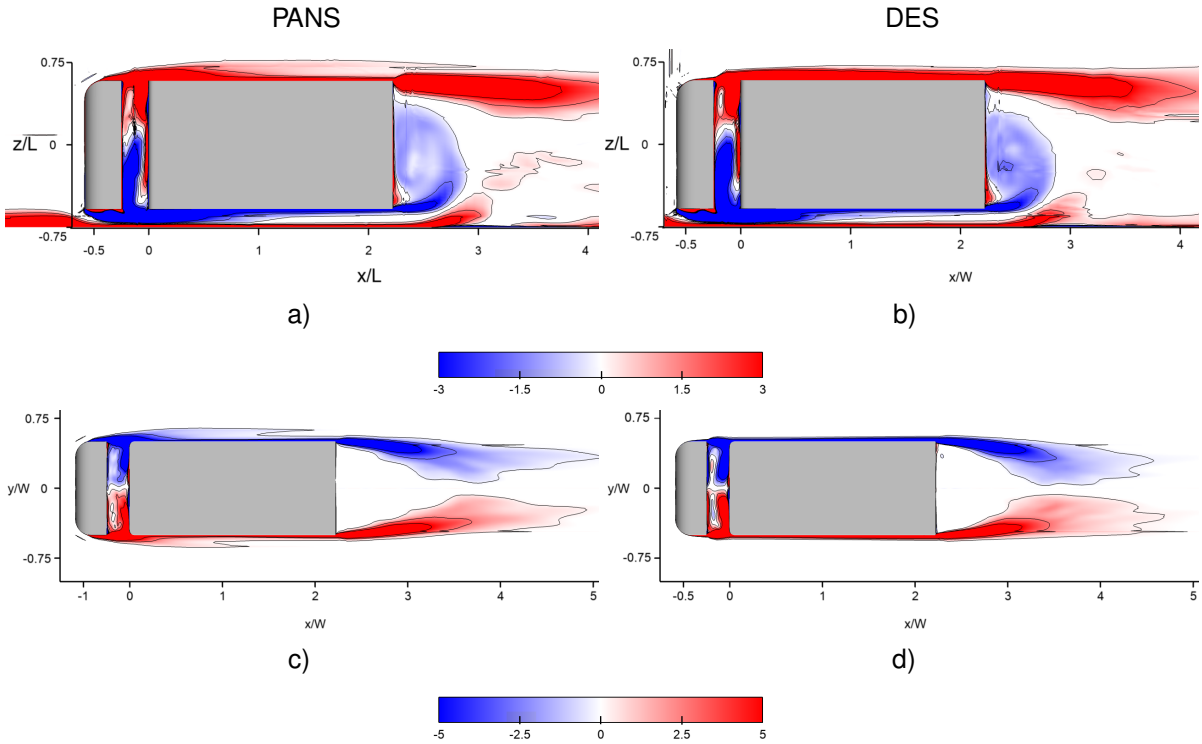

Figure A.4: Contours of normalized time-averaged vorticity using the coarse mesh with PANS and DES: a) and b) y-vorticity, c) and d) z-vorticity

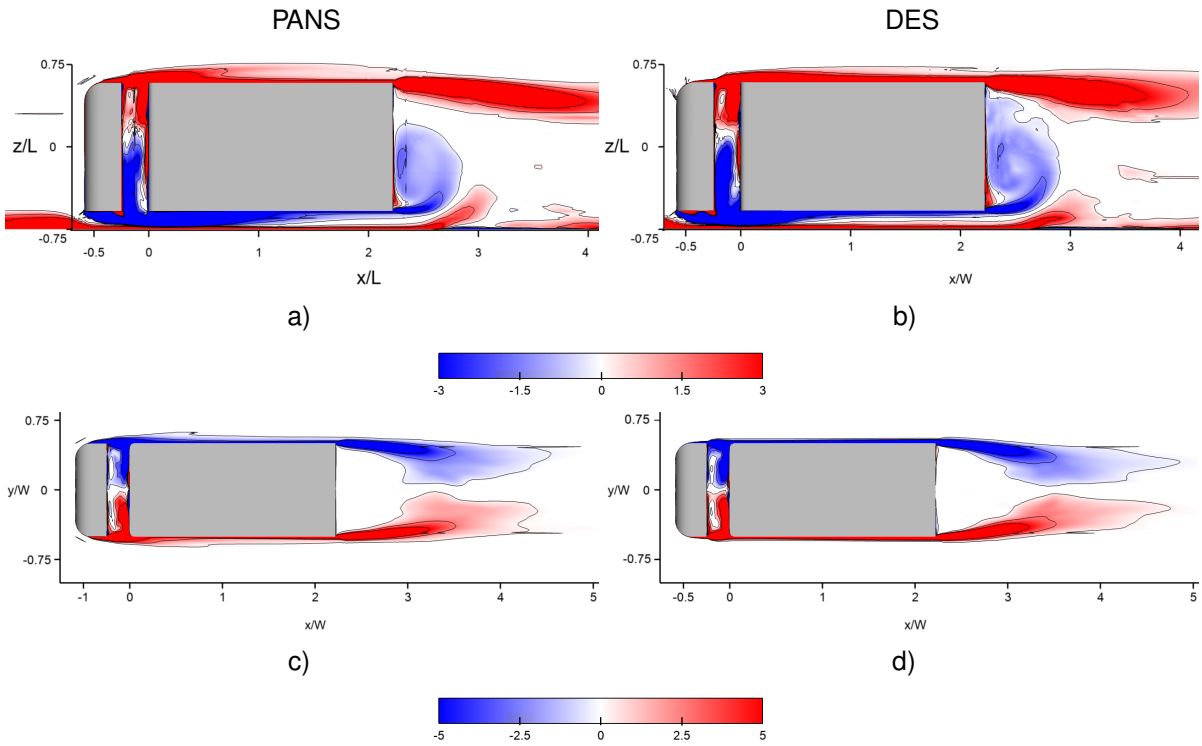

Figure A.5: Contours of normalized time-averaged vorticity using the medium mesh with PANS and DES: a) and b) y-vorticity, c) and d) z-vorticity

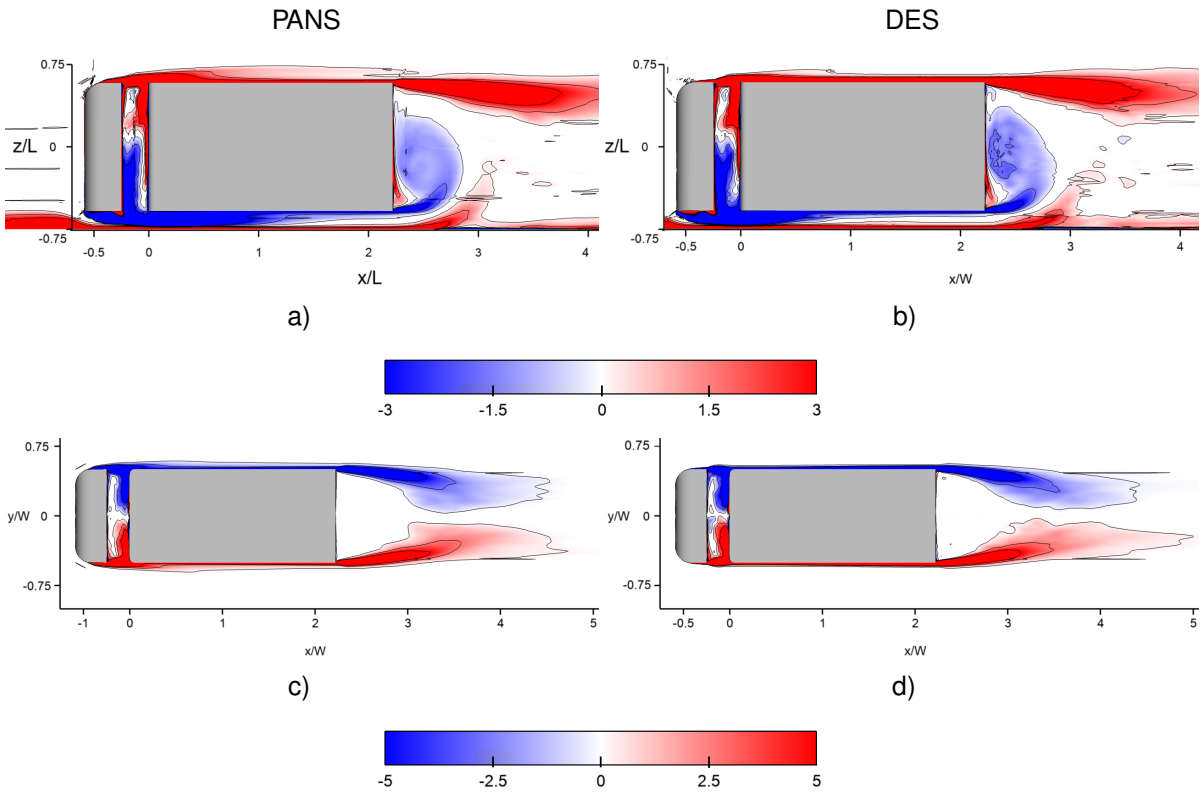

Figure A.6: Contours of normalized time-averaged vorticity using the fine mesh with PANS and DES: a) and b) y-vorticity, c) and d) z-vorticity

A.3 Appendix 3

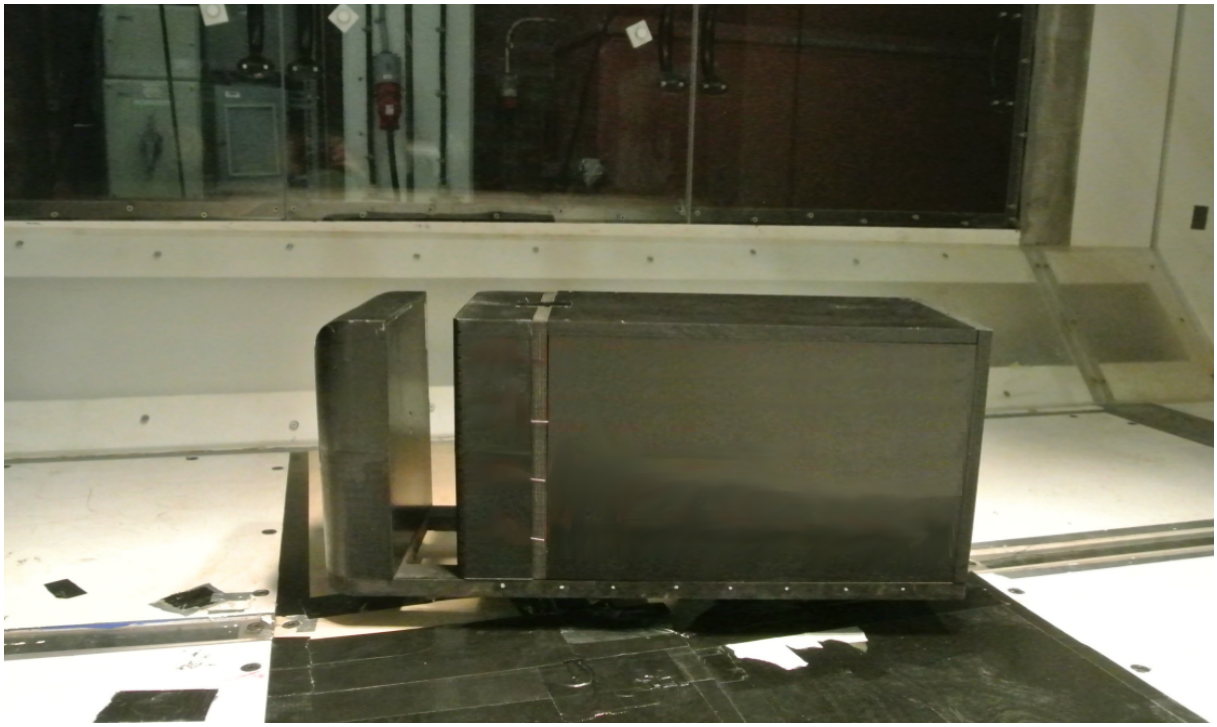

Figure A.7: Picture of the model used in the PIV experiments.